Doctoral Thesis

Growth and Characterization of Graphene on Texture-Controlled Platinum Films

Jae-Kyung Choi

Department of Material Science Engineering

Graduate School of UNIST

2015

Growth and Characterization of Graphene on Texture-Controlled Platinum Films

Jae-Kyung Choi

Department of Material Science Engineering

Graduate School of UNIST

Growth and Characterization of Graphene on Texture-Controlled Platinum Films

A thesis/dissertation
submitted to the Graduate School of UNIST
in partial fulfillment of the
requirements for the degree of
Doctor of Philosophy

Jae-Kyung Choi

7. 10. 2015 of submission

Approved by

Advisor
Soon-Yong Kwon

Growth and Characterization of Graphene on Texture-Controlled Platinum Films

Jae-Kyung Choi

This certifies that the dissertation of Jae-Kyung Choi is approved.

07.10.2015

signature

Advisor: Soon-Yong Kwon

signature

Zonghoon Lee

signature

Hyung-Joon Shin

signature

Sung Youb Kim

signature

Sung Dae Kim

Abstract

In this study, the primary purpose of this research is to grow high quality graphene on platinum (Pt) films, especially wrinkle-free graphene as a 2-dimensional membrane for transparent conductor and hydrophobic water-distillation applications by using texture-controlled Pt films that have incorporated oxygen atoms. In order to achieve the final goals, this research primary had been focused on analysis of abnormal Pt grains through annealing process and study of graphene growth kinetics through chemical vapor deposition process. Then, a new transfer method was applied to graphene transfer by reacting graphene/Pt interface, without incurring damages and unintentional doping.

The wrinkle-free graphene was synthesized by using texture-controlled Pt films (200, 220) with giant grains (GGPt) via chemical vapor deposition (CVD). The Pt films on SiO_2/Si substrates could be controlled by sputtering with Ar/O_2 gas mixtures and abnormal grain growth was affected by the incorporated oxygen during post-annealing process. In order to analysis of graphene growth kinetics on GGPt, each films were heated at the CVD process temperature of ~975 ℃ and maintained for 10 min under CH_4/H_2 gas mixture (5 and 50 sccm, respectively) without cleaning treatments. Enhanced surface perfectness and limited number of grain boundary (GB) of Pt induced homogeneous C-precipitation, thus the high-crystallized monolayer graphene sheets was formed. The transferred graphene shows wrinkle-free characteristics regardless of the orientation types of Pt, probably due to much lesser difference in thermal expansion coefficient (TEC, ~11 μm $m^{-1}K^{-1}$ at 1000 ℃) to graphene. The wrinkles or ripples-free graphene films showed a high crystallinity and high carrier mobility at room-temperature up to ~8,500 $cm^2V^{-1}s^{-1}$.

To transfer graphene, a thermal-assisted transfer method was applied by a NaOH (1 M) aqueous solution at 90 ℃. The thermal-assisted transfer method was only activated by the hydroxide (OH^-) in NaOH solution to separate the graphene/Pt interface. The thermal-assisted transfer process allowed the complete transfer of large-scale graphene films onto arbitrary target substrates without incurring damages and unintentional doping. Compare to bare GGPt, graphene-free GGPt showed no contamination and degradation after the graphene transfer. The fact was demonstrated by XPS data, which showed almost same binding energy of Pt-$4f_{5/2}$, Pt-$4f_{7/2}$ (74±0.2 eV). On the basis of these results, a recycle ability of Pt was demonstrated. Also, the result of graphene on the recycled Pt showed almost same quality as the obtained graphene from 1st Pt. Furthermore, the transfer method could be applicable to the large-scale patterned graphene on Pt films with SiO_2 regions. By comparing an electrochemical transfer method, the thermal-assisted transfer method have proved to be successfully transferred onto SiO_2/Si substrate for the patterned Pt films. The reason is that the reaction between Si and Na^+ took place in the boiled NaOH solution to react the SiO_2 surface.

Through a pre-annealing step in CVD process, the porous graphene membrane could be obtained from the porous Pt texture. The density and size of pore depended on the pre-annealing time in hydrogen gas.

Especially, a dense pores of Pt films was obtained with controllable density (~2×10^5 cm^{-2}) and ~2.5 μm of radius by pre-annealing for 5 min. Since an oxygen was inserted during Pt film sputtered as an adhesion layer between Pt and SiO_2/Si substrate, Pt sintering has occurred by oxygen diffusion during pre-annealing step in H_2 atmosphere. The porous graphene membrane were successfully transferred onto SiO_2/Si substrate by thermal-assisted transfer method. Surprisingly, graphene was grown direct in the pores of Pt films. It was demonstrated through that Pt particles directly formed growth of the graphene.

In summary, this study shows the wrinkle-free characteristic of graphene layer by using Pt thin films with preferred orientations and giant grains. In addition, large-scale and patterned graphene films can be successfully transferred onto arbitrary substrates via thermal-assisted transfer method and the Pt substrates can be repeatedly used for the proliferation of graphene applications. Furthermore, this transfer technique shows a high tolerance to variations in types and morphologies of underlying substrates, which is essential for the various applications proposed for graphene.

Keywords : Graphene, Chemical vapor deposition (CVD), Platinum (Pt), Giant grain, Wrinkle-free graphene, Thermal-assisted transfer, Porous membrane.

Contents

List of figures

List of tables

Chapter 1. Overviews

1.1 Graphene

1.1.1 Characterizations of graphene

Conventionally, graphene is a mono-layer from graphite.[1] Graphene is 2-dimensional materials of sp^2-bonded carbon atoms composite in a honeycomb lattice.[1-2] The length between carbon atoms is about 1.42 Å. In particular, the graphene has 3 sigma-bonds (σ-bonds) in a planar array and 1 π-bond out of plane. Due to the 3 neighbor strong bonds composite 120° angles in-plane, the graphene shows superior mechanical properties with an Young's modulus of 1 TPa and an intrinsic tensile strength of 130 GPa.[3] These intrinsic mechanical properties can be utilized such a pressure sensor. Besides, a thermal transport ability is covered by the graphene and reported thermal conductivity of theoretically 5300 $W \cdot m^{-1} \cdot K^{-1}$.[4] The thermal properties in graphene have attracted interest for thermal sensor, thermal management devices, and heat dissipation layer or heat sink materials. The graphene also shows high carrier/current density (theoretical limit ~2.5 X 10^5 $cm^2/V \cdot s$) [5] which originate the linear dispersion at the Fermi level with zero electron effective mass from π-orbital (figure 1-1).[6] It makes an ideal electric devices such as transparent conducting layer and flexible integrated materials.

1.1.2 Trends of graphene

2010 Nobel physics prize was already shown a deep novelty of the unique properties. In many research fields, the graphene already has been pioneered an academic phenomenon and practical devices for industry. The manufacture of graphene appears to be evolved toward commercialization, which originated from micro-sized graphene flakes using mechanical exfoliation in 2004.[7] And the production of graphene heads directly for large-scale, high-quality, and simple processing.[8]

In spite of the many interesting properties of graphene and advanced techniques in graphene fabrication, there still remains the limitation. In cases of poor graphene such as including impurities after graphene transfer process or putting on amorphous supporting substrate or defects, these defects are known as inducing the degradation characteristics of graphene. For examples, graphene with polymeric residues can decrease the thermal conductivity to 500~600 $W \cdot m^{-1} \cdot K^{-1}$ or the carrier mobility to 50 %.[5,9] This even applies to graphene which is not a single-layer. Because graphene properties depend on the number of layers. Shihua Zhao et al. reported the single-layer graphene (SLG), bi-layer graphene (BLG), and multi-layer graphene (MLG) exhibit apparent differences in electrostatic force and capacitance

behaviors (figure 1-2).[10] Also, the optical properties of graphene are strongly dependent on their stacking orders or layers. Yingying Wang et al. calculated that a twisted BLG is frequency dependent with additional light absorption behaviors due to band folding effect while SLG or Bernal stacked BLG is frequency independent in the visible wavelength (figure 1-3).[11] Shou-En Zhu et al. showed that the optical transmittance decline by the increasing graphene stacks as an experiment (figure 1-4).[12] Therefore, recent trend of graphene manufacturing is trying to acquire the single-layer and defects-free graphene for commercialization.

1.2 Synthesis of graphene

Current production methods for graphene are undergoing development. The methods can be divided roughly into 4 types with mechanical exfoliation[7], chemical exfoliation[13,14], epitaxy method[15], and chemical vapor deposition (CVD) method[16] (figure 1-5).

1.2.1 Mechanical exfoliation

First one is the mechanical exfoliation. This involves cleaving graphite by placing it on scotch tape and repeatedly peeled off the graphite. This graphene can keep its unique properties and I can obtain high quality graphene.[7] However, the fabricated size is so small for practical application and it is hard to make formatting special position.[13]

1.2.2 Chemical exfoliation

To overcome this drawback, chemical exfoliation method has been introduced.[14] The chemical exfoliation method is called graphite oxide reduction or reduce graphene oxide (RGO) method. Rapid heating of graphite oxide and exfoliation yields highly dispersed carbon powder with a few percent of graphene flakes. This method can produce the mass production with low cost. Compare to previous method, I cannot obtain high quality graphene owing to incomplete removal of functional groups.

1.2.3 Epitaxy

For production of high-quality graphene, an epitaxial graphene formation method was introduced.[15] The epitaxial graphene formation is that reduction of silicon carbide (SIC) at the high temperature around 1000 ˚C. This process is relatively straightforward, as the silicon desorbs around 1000 ℃ in ultra-high vacuum. The epitaxial method can produce the mass production. However, the price of SIC substrate is quite expensive and the way of processing is complex compared to other method. Likewise,

mass production of graphene is difficult.

1.2.4 Chemical vapor deposition

Final method is CVD process which is used to hydro-carbon source with hydrogen gas (H_2) included inert gas like Nitrogen (N_2) or Argon (Ar) gas.[16] At high temperature, using the ability of carbon solubility and hydrocarbon decomposition can grow the graphene with catalysts. This method can obtain large-scale and high-quality graphene. The remaining challenging is to obtain fine control over film thickness and prevent secondary crystal formation. In the respect of thermodynamics, this method is needed high pressure and temperature. Among this method, using the CVD has been demonstrated as an attractive approach because of the ability to grow high-quality graphene films over large areas and wide accessibility of industrial equipment. When a fabrication of graphene uses the CVD method, I need hydrocarbon source, high temperature and catalyst material which have the carbon solubility. One of the important things is to choose the catalyst material. A transition metal which has the carbon solubility is the face centered cubic (FCC) structure like Ni, Cu and Pt. The carbon solubility of Ni is 0.11 % at 1000 ˚C. The carbon solubility of Pt is 0.9% at 1000℃. The carbon solubility of Cu is 0.004% at 1000℃. If I use the Ni or Cu which has high carbon solubility, I can obtain the graphene which has monolayer and multilayer. It means that the Ni or Cu is very sensitive to CVD circumstances, but the transition metal can be controlled externally for desired graphene.

1.2.5 Rapid thermal annealing

Recently, a rapid thermal annealing (RTA) method is reported (figure 1-6).[17] Actually, the RTA method was one of the specialized semiconducting materials. The difference between typical CVD and RTA can be describe that the graphene formation mechanisms. While the CVD method is using the decomposed hydrocarbon source to high-quality graphene, the RTA method is using a self-decomposition of carbon in catalytic material for rapid production (figure 1-7).

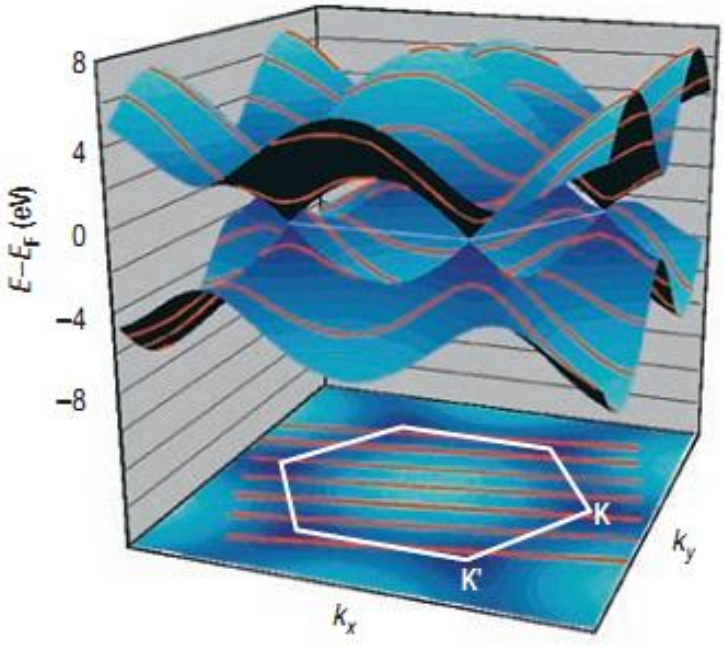

Figure 1-1. A band structure (top) and Brillouin zone (bottom) of graphene.[6]
The high carrier velocity is originated from massless particles.

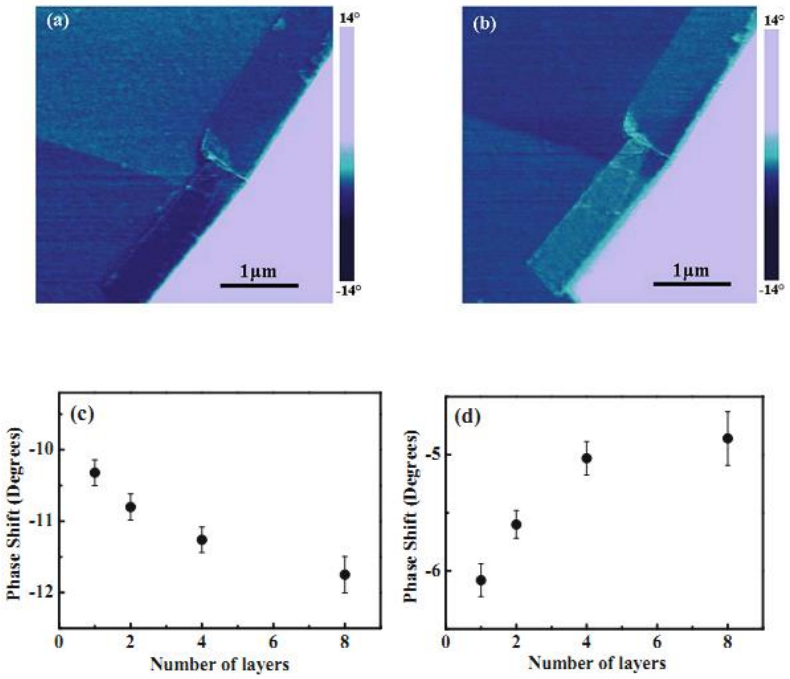

Figure 1-2. The phase shift of graphene versus the number of graphene layers.[10]

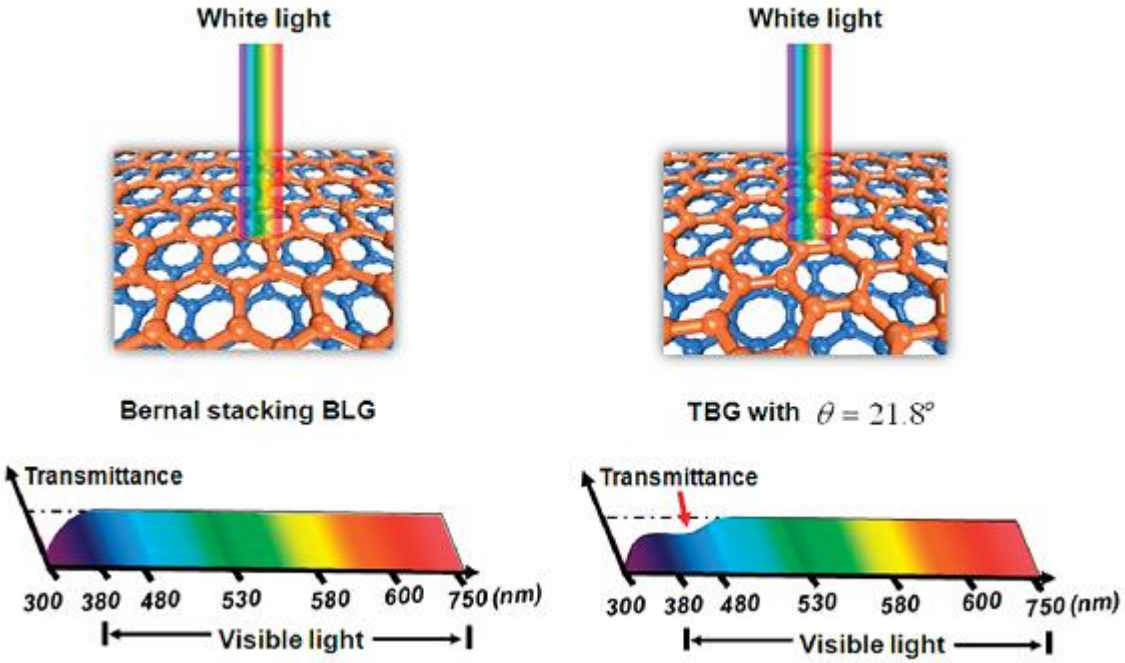

Figure 1-3. Light absorption by SLG or Bernal stacked BLG and TBG.[11]

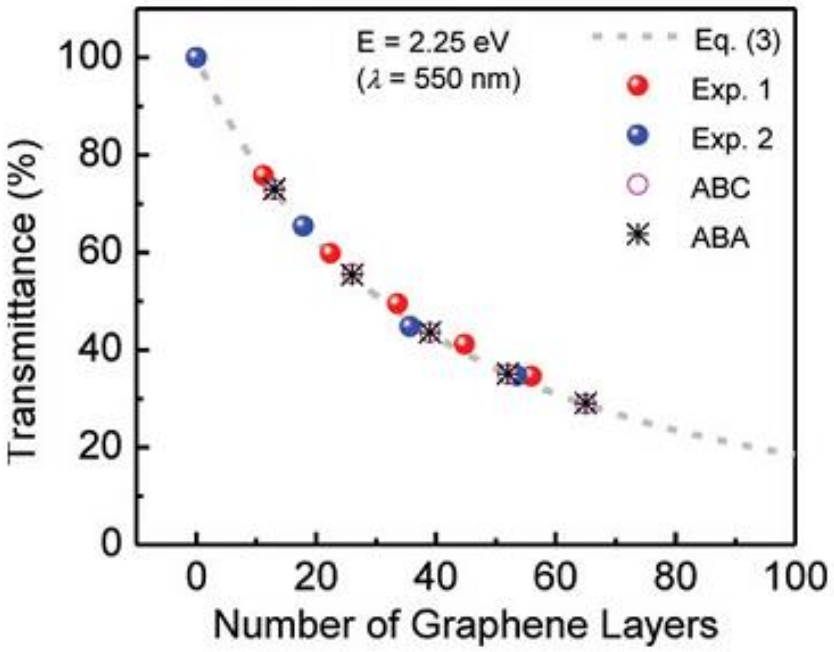

Figure 1-4. Number of graphene layer dependent optical transmittance.[12]

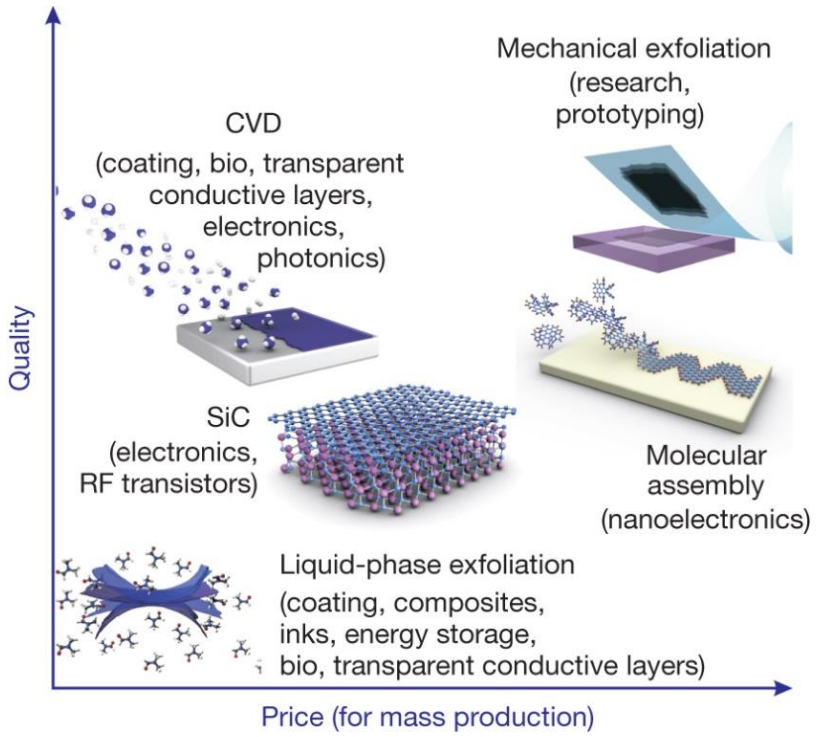

Figure 1-5. Representative methods of graphene production.[18]

Method	sample size (mm)	Carrier mobility ($cm^2V^{-1}s^{-1}$)	Applications
Mechanical exfoliation	> 1,000	$\geq 10^6$	Research
Chemical exfoliation	≤ 0.1	100	Coating, Conductor, Composites
CVD	1,000	10,000	Coating, Conductor, Composites Bioapplications, Membrane
Epitaxy	50	10,000	Hf transistor, electronics

Table 1-1. Representative properties of graphene obtained by various methods.[18]

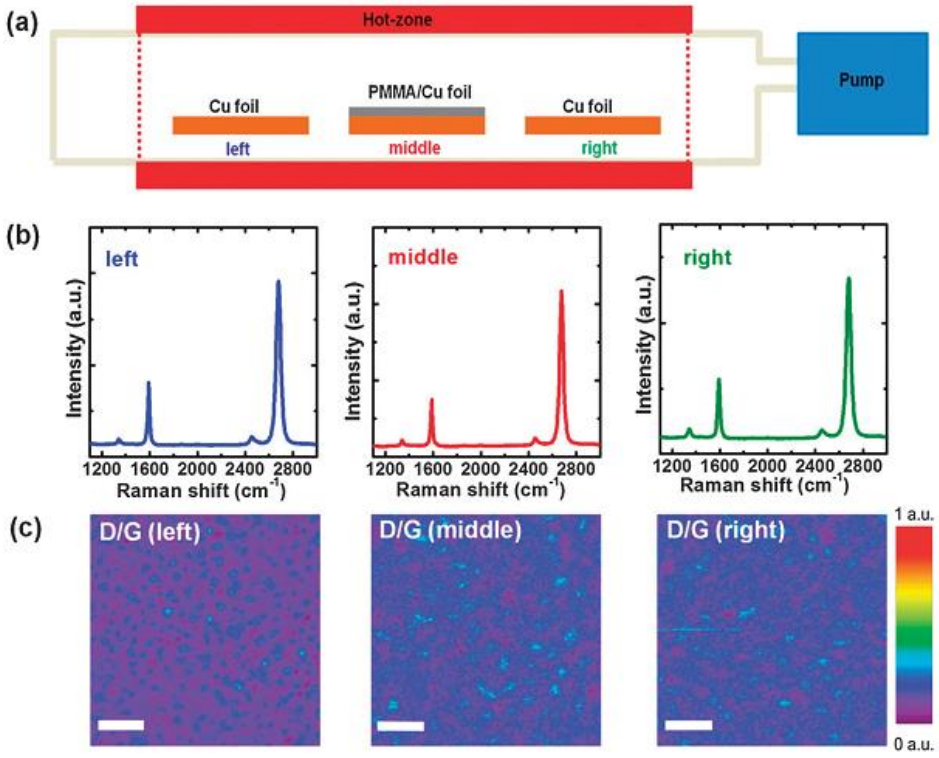

Figure 1-6. Characterization of graphene obtained by RTA method.[17]

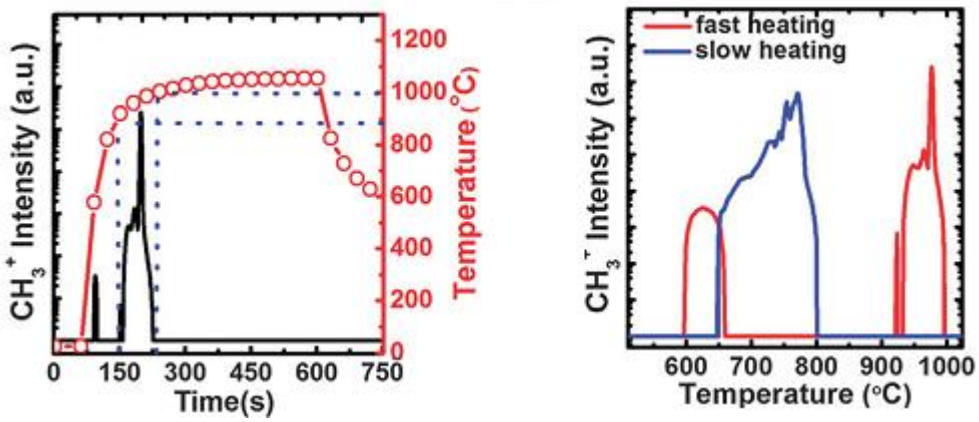

Figure 1-7. Self-decomposition of carbon in catalytic material for rapid production.[17]

Chapter 2. Growth of Graphene on Giant Grain Platinum Films

2.1 Introduction

The graphene can be synthesized by following methods; Cleavage of graphite with the Mechanical exfoliation, reduction of graphene oxide with Hummers method, and graphene growth on transition metal with the Chemical Vapor Deposition (CVD). Among these, the CVD route has a potential to mass-produce the graphene with superior quality. But CVD route is bound to limit as polycrystalline graphene and wrinkle due to usage of the transition metal, which is very sensitive to high temperature. In particular, the transition metal leads to thermal stress with graphene, and the growth behavior of graphene is dependent to their crystallinity.

2.1.1 Wrinkles of graphene

The wrinkle of is an unavoidable problem in CVD-graphene. The wrinkle is species of one-dimensional (1-D) line defects like edges, grain boundaries, ridges, and ripples (figure 2-1).[19,20] The 1-D wrinkle is caused by various routes in process of graphene production. During high temperature CVD process, a thermal expansion coefficient difference between graphene and carbon catalytic substrate leads to thermal stress at the cooling process. The wrinkle have resulted from the thermal stressed graphene layer on carbon catalytic substrate. Therefore, the main driving force of yielding wrinkle is the difference of thermal expansion coefficient (TEC) between graphene and substrate (figure 2-2).[21] And the high temperature ambience for graphene growth makes wrinkle inevitable. In addition, a surface morphology of carbon catalytic substrate also leads to the wrinkle. According to Yanhong Zhang et al.[19], the part of these line defects formation is affected by align system of the carbon catalytic surface steps. Also, density of wrinkle is dependent on graphene layer resulting from the carbon catalytic crystallinity. They show the high-density wrinkle At monolayer graphene on Pt(111) with low TEC, which can be modulated by controlling the CVD growth conditions (figure 2-3).[19] In spite of the Pt(111) with low TEC, they could not overcome the wrinkle. It means that the wrinkle depends not only on the TEC but also on the crystallinities of carbon catalytic substrate. Seung Jin Chae et al. showed that the wrinkle appears on near grain boundary in poly-Ni foils (figure 2-4).[22] They reported that cause is the graphene layer tends to absorb the strain/stress energy by mechanical deformation at the defect lines like the grain boundary in poly-Ni where the defect lines minimize the local strain/stress by formation of wrinkle. The cause of wrinkle formation are not the end, and the wrinkle can also form in the graphene transfer process or as graphene conditions.[23] V. E. Calado et al. found that the wrinkle can form on a hydrophilic target substrate during the wet transfer method (figure 2-5). In this regard, they suggested that the wrinkle formation should be controlled by using a hydrophobic target substrate

during the wet transfer. Above three major causes of winkle-formation via CVD-graphene, which are not relevant with ideal exfoliated graphene, affect the quality of graphene as defects. And these defect lower electronic properties, mechanical properties and chemical stability. So, the engineering of wrinkle is an important challenge for graphene industry. Therefore, I suggest using the texture-controlled Pt films with low TEC and low grain boundaries. As like this, I studied the graphene wrinkle related with the platinum textures. And I found the removal of driving force for the wrinkle position. Finally, I could control the wrinkle and reduce them by using texture-controlling of Pt films. .

2.1.2 Graphene on platinum for low thermal expansion coefficient

Generally, the formation of graphene resulting from carbon soluble conventional metal such as Cu[24], Ni[25] is quite sensitive to temperature in CVD growth. The reason for dependence on growth temperature is because of that carbon is first dissolved in the metal at high temperatures, followed by precipitation on its surface upon cooling. The difference in TEC between the graphene and metal occurs in this process, and thus the defects of graphene is generated by the thermal mismatch. Recently high quality graphene synthesis has been attempted in several ways to minimize defects in graphene. Among them, overcoming TEC between graphene and its metal catalyst is one major candidate to enhance graphene quality. Pt[26], much like those of Ni[25], Ru[27], Pd[28], and Cu[24], allows for the synthesis of graphene due to its outstanding properties for hydrocarbon catalyst (carbon solubility ~0.9 % at 1000 ℃)[29]. It exhibits excellent properties in thermal stability and chemical resistance. Especially, the small thermal expansion coefficient difference of Pt (~11 um m^{-1} K^{-1} for Pt, ~21 um m^{-1} K^{-1} for Cu, ~17 um m^{-1} K^{-1} for Ni at 1000 ℃) to graphene (~6.7 um m^{-1} K^{-1})[30] allows high quality synthesis of graphene with defect free film. Numerous research papers have reported grown high-quality graphene layers onto Pt foils by CVD method[31]. In addition, the precise growth mechanism of graphene on Pt is still uncertain, and transfer of graphene from Pt is difficult since Pt has strong chemical resistance and it is hard to separate graphene from Pt film. In this chapter, I report the orientation-sensitive growth of graphene on preferred orientated films of giant grain Pt (200), (220) via CVD method.

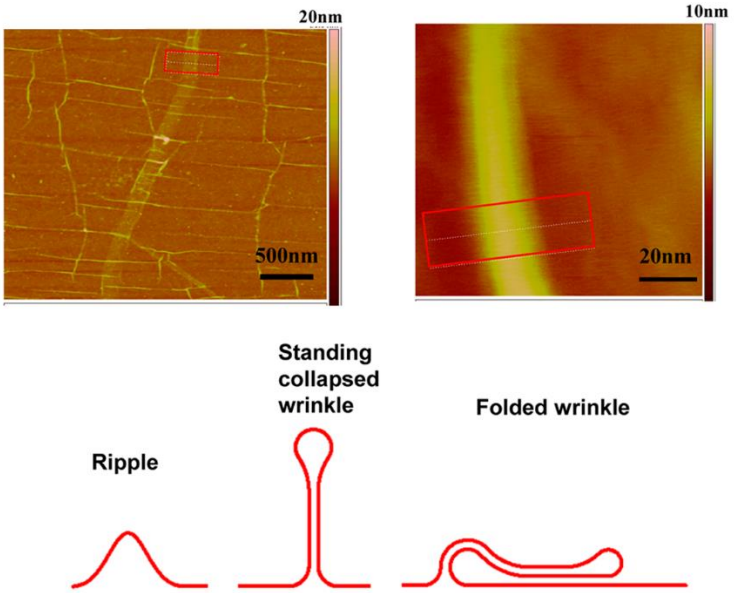

Figure 2-1. Topographies and structures of graphene winkle.[20]

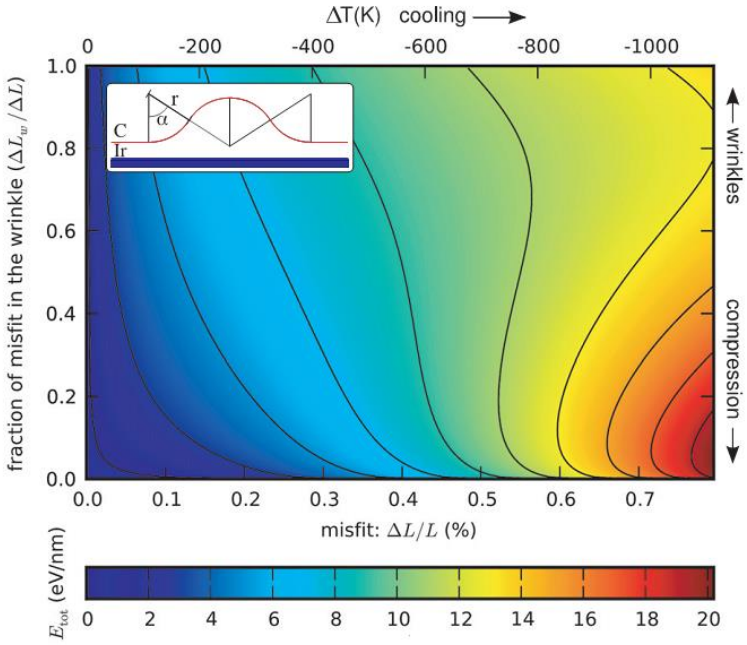

Figure 2-2. Map of E/nm of wrinkle total energy in graphene.[21]

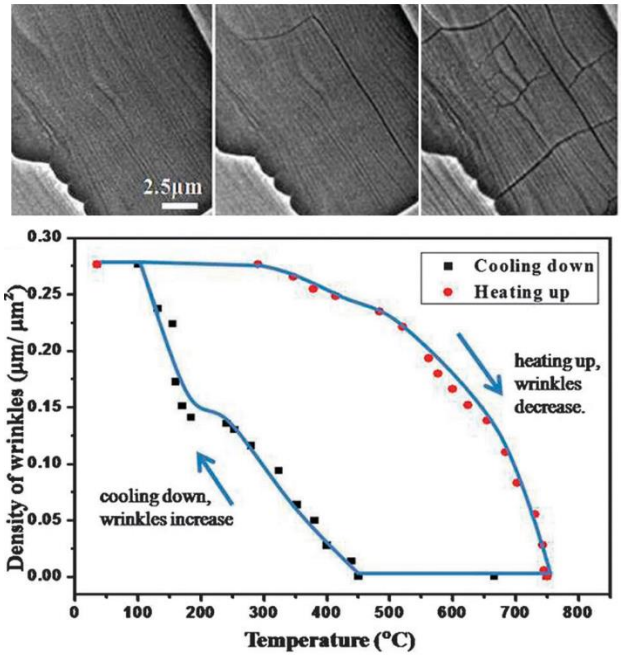

Figure 2-3. Wrinkle-formation of graphene on Pt(111).[19]

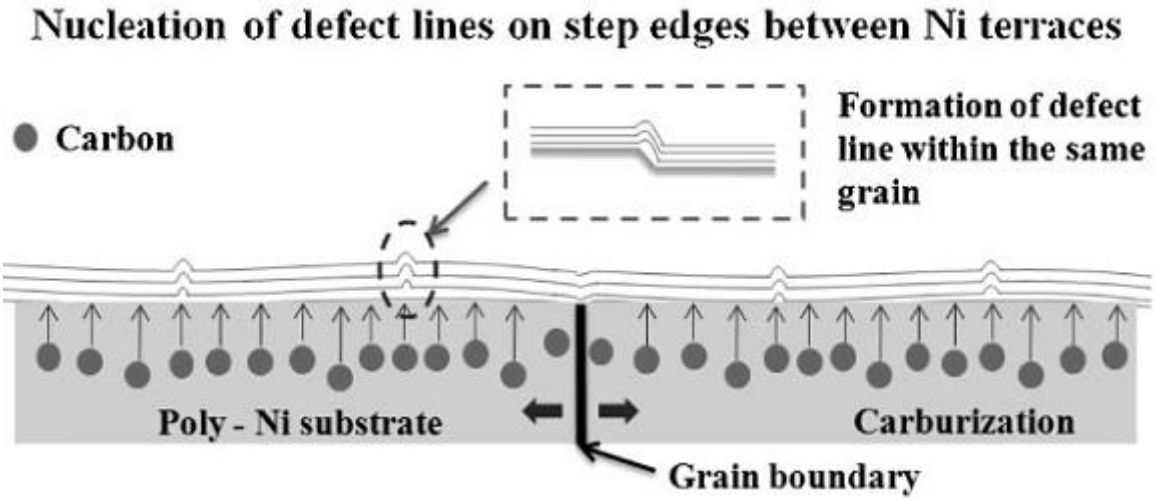

Figure 2-4. Illustration of wrinkle formation on near poly-Ni grain boundary.[22]

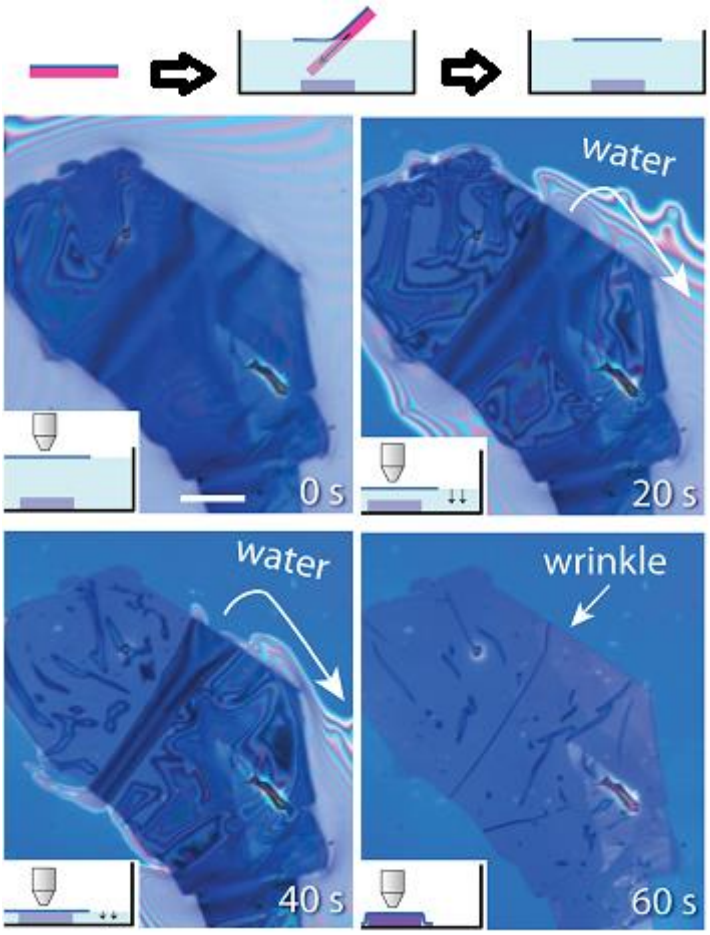

Figure 2-5. Wrinkle-formation during wet transfer onto hydrophilic target substrate.[23]

2.2 Experimental section

In this chapter, a key strategy is applying the texture-controlling of Pt films for growth of wrinkle-free, mono-layer graphene. The Pt films have preferred orientation and controlled crystallinity through abnormal grain growth from polycrystalline Pt films. The growth of Pt grains induces the minimized number of grain boundaries, which will result in the improvement of inhomogeneous graphene formation.

2.2.1 Texture controlled platinum films

In this study, I report that the giant grain growth behavior of Pt films sputtered by Ar/O_2 gas mixtures. On the 4 inch-SiO_2/Si substrate, platinum thin films were deposited by DC magnetron sputtering with Ar/O_2 gas mixture in optimized deposition conditions. In additional to Ar gas, oxygen gas were injected and they enhanced the adhesion property of Pt to SiO_2/Si[32,33] substrate and preferred orientation control was possible.[34] Generally, the lowest surface energy at 111 plane grow preferentially; however, in this research, oxygen was attached on 111 surface and inhibited the growth of Pt. Finally, I obtained relatively 200 orientated Pt films.[35] By fixing temperature, deposition rate, and lowering chamber pressure, I obtained relatively 220 orientated Pt film. In order to remove oxygen and enhance the crystallinity, I annealed the Pt film at 1000 ℃ for one hour. Although 200 orientated Pt film has a small portion of 111 orientation after post annealing, all Pt films carried giant grain growth with enhanced crystallinity property. In general, grains of the metal thin films grow to minimize internal energy of a closed system during the post-annealing process. When the grain growth is caused by driving force to decrease grain boundary, and the grain growth is defined as a normal grain growth as a general bulk.[36] The grains keep growing until the grain size increases two or three times compared with film thickness. Then, the inserted oxygen plays as an inhibition force which dragged the normal grain growth of Pt at low temperature. The inhibition force of grain growth was minimized by inserted oxygen diffusion in Pt lattice at high temperature. The minimization of inhibition force activates the giant grain growth of Pt. It is defined as an abnormal grain growth. The metal thin films, grown by normal grain growth, have columnar structures which show rapid grain growth centered at specific grain with capturing near normal grains. In result, grain size reaches several tens of times bigger than thin film thickness.[37,38] From this fact, the Pt film was orientated along the (200) direction to facilitate oxygen diffusion and removal which resulted in the formation of a Pt film with a grain size on the order of a few hundred microns (figure 2-6 a). Unlike columnar structure of Pt(111), the Pt(200) surface particularly stands out TSK (terrace-step-kink) model as general single crystal surface. From relatively low pressured Pt sputtering and the abnormal grain growth, the giant grain sized Pt(220) film is served. Figure 2-6 (b) and (d) show surface and orientation of the giant grain sized Pt(220) film with grain to 1 mm. The single

crystallinities of the giant grain sized Pt films were demonstrated by seeing the un-intentionally etched surface of the Pt films via an AFM (figure 2-6 **e** and **f**). The un-intentionally etched Pt(200) or (220) morphologies are identical triangular or rhomboid pits, respectively, implying that the giant grain is a single crystal. The AFM images show a surface on $Pt/SiO_2/Si$ substrate with graphene used in CVD process in H_2 gas (50 sccm) and CH_4 gas (5 sccm) at 975 ℃ for 15 min. The pits are generated by removal of oxygen. From the XRD analysis, both Pt(200) and a small portion of (111) growth coexist together. Furthermore, triangular pits 8 nm in depth that can be observed in the diamond structure of Pt(111) are also observed in portions of the unexpectedly etched Pt(200) surface. In the Pt(220) surface, rhombus-shaped or circle pits that were 50 nm in depth can be observed; however, these did not appear to influence the graphene growth.

2.2.2 Growth of graphene on platinum films via chemical vapor deposition

In this study, I could achieve graphene growth by using the CVD method. Graphene growth by means of the CVD process, using a transition metal as a hydrocarbon catalyst, is inherently quite sensitive to temperature. Conventionally, carbon is first dissolved in the metal at high temperatures, followed by precipitation on its surface upon cooling. In terms of metal surface energy, a high energy barrier tends to result in carbon reaction rates that are sensitive to temperature, and thus the graphene quality is dependent on the catalytic reaction kinetics.[39] In this experiments, the CVD process excluded a pre-annealing and pre-treatment progress of Pt surface (figure 2-7). Because of noble properties of the Pt films, the CVD method does not require further treatment process. The further details can refer to the following description. Graphene was grown on giant grain sized Pt films (GGPt) with 400-nm-thick using a LP-CVD (low-pressure CVD) system. 1st, a giant grain sized Pt(200) or (220) film with a area of ~1 × 1 cm^2 was loaded into a quartz chamber of LP-CVD and the quartz chamber was increased up to the growth temperature of T~975 ℃ with a constant flow H_2 (1 sccm) over 40 min. After ranging T~975 ℃, a H_2(50 sccm)/CH_4(5 sccm) gas mixture was inserted into the quartz chamber for 10 min to growth of graphene. Subsequently, the quartz chamber was cooled down to ~700 ℃ without changing the gas conditions. After then the chamber was cooled down to RT (room temperature) under a vacuum state.

2.2.3 Apparatus

(1) For observing surface morphologies of as-grown GGPt films, the surface of GGPt films were analyzed by an atomic force microscopy (Veeco Multimode V, AFM). Using tapping mode, the AFM tool was used to achieve a scan size of 2 × 2 μm^2.

(2) The morphologies of the graphene/GGPt and transferred graphene onto SiO_2 substrates were measured using a field-effect secondary electron microscopy (FEI Nanonova 230, FE-SEM) using an acceleration voltages of 10 to 20 kV.

(3) For optical orientation observation, an orientation mapping was observed by electron beam scattering diffraction (EBSD) with the FE-SEM tool.

(4) The crystallographic orientations of the GGPt films were measured by high resolution X-ray diffraction (HR-XRD) pattern by using an X-ray diffractometer (Bruker D8 Advance) using Cu-Kα X-ray source with λ: 5046 Å.

(5) The chemical states, presence, and of foreign species (doped impurities) in the GGPt films were analyzed by using X-ray photoelectron spectroscopy (Thermo Fisher, XPS). The analyzes of XPS were operated on a K-α spectrometer using 72 W Aluminum-K-α non-mono-chromatic X-ray excitation, with an analysis of ~10 mm area diameter and a 50 eV pass energy for the electron analysis. The chamber was analyzed at ~1×10^{-9} mbar. In the GGPt films, the impurities or dopants was investigated by dividing the individual peaks.

(6) For investigation of successfully transferred graphene, the transferred graphene layers from GGPt films were analyzed by Raman spectroscopy. The Raman spectrums and Raman mapping images were obtained from the transferred graphene layer which was transferred onto a SiO_2/Si substrate (a thickness of SiO_2 layer ~300 nm). The Raman analysis was operated by a 532 nm excitation wavelength (2.33 eV) using a WiTec alpha 300R Micro-Raman system. The Raman laser spot size had ~ 640 nm for a ×50 objective lens with numerical aperture of 0.5 and the power was ~2 mW. The Raman spectrums were investigated and the Raman mapping images were analyzed by x-y translation stage using computer-controls with a raster scan. The spectroscopic Raman mapping images were analyzed by each individual pixel a 50×50 μm^2 step size using a WiTec Project software 2000. The Raman data mentioned in this chapter, such as the intensity ratio of the G-to-2D bands and FWHM values was numerical averages of values that were analyzed at more than 30 different points per one sample.

(7) For domain size and imperceptible observation of transferred graphene, the graphene layers were transferred onto carbon coated gold transmission electron microscopy (TEM) holey grids by utilizing conventional dry transfer method. Next, the bright field (or dark field) TEM graphene images were obtained by using a JEOL-2100F (installed at Korea Institute of Materials Science - KIMS) that used at 200 kV which was equipped with a Gatan imaging filter system. For the image processing and analysis, a Gatan Digital Micrograph software was used.

(8) For analysis of electrical characterizations, the transferred graphene layers were measured by manufacturing a field-effect transistor (FET) device. A gate was bottom (or back) gate using SiO_2/Si substrate. Thus, the FET devices were manufactured by transferring the graphene layers onto p-Si substrates with 300-nm thick thermal oxide for insulating layer. For the FET fabrication, conventional photo-lithography process and the O_2 plasma-etching progress were applied. And the FET device has a 100 μm-channel widths and 200 μm-channel length. For Cr/Au of 10 nm/60 nm were used as source-drain contact electrodes, the electrodes were deposited by an e-beam evaporator. The analysis of electrical properties were measured by standard 4-probes station at room-temperature (MS-tech, Agilent Technologies B1500A).

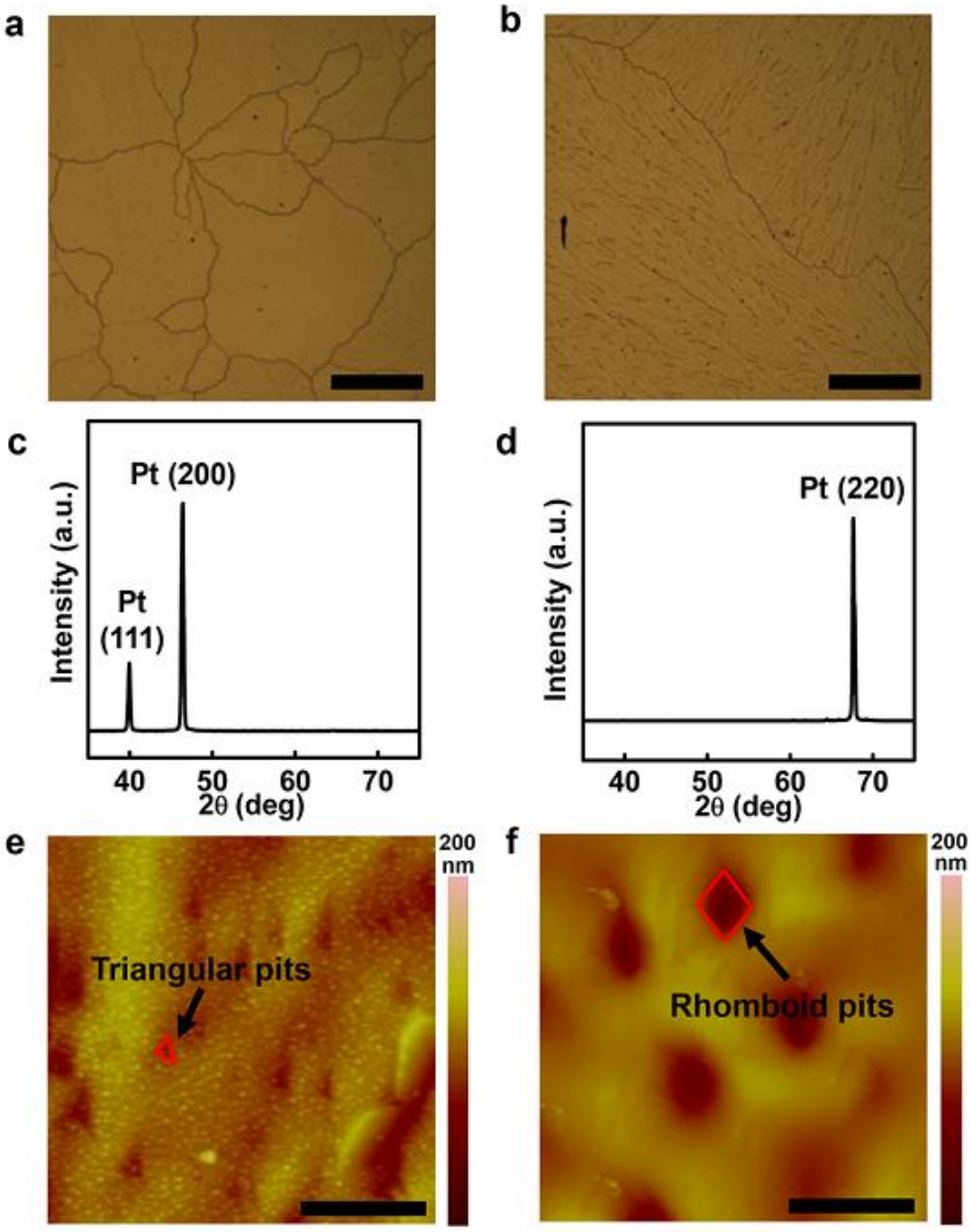

Figure 2-6. Platinum (Pt) thin films with preferred orientations of (200), (220) with giant grains. **a** and **b** show optical images of giant grain of 400-nm-thick Pt films on SiO_2/Si substrate. (a) Surface of Pt(200) with a millimeter-sized grain boundary (GB), and (b) Pt(220) (scale bars: 200 μm). **c** and **d** show corresponding high resolution X-ray diffraction patterns (HR-XRD) of (a) and (b). **e** and **f** show atomic force microscopy (AFM) images of etched surface for (e) Pt(200) and (f) Pt(220) with triangular pits and rhomboid pits, respectively.

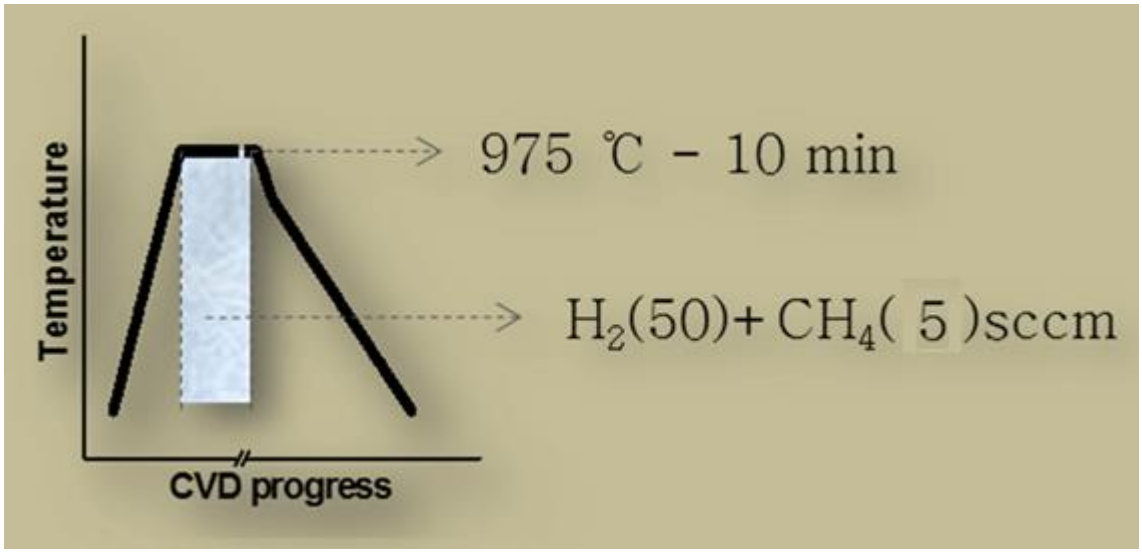

Figure 2-7. Simple chemical vapor deposition route for graphene fabrication using platinum films.

2.3 Results and discussion

In this section, a key point is an orientation sensitive CVD growth for strictly monolayer, wrinkle-free graphene is formed by using the texture controlled Pt(200) and (220) with giant grains (GGPt). The two different orientation of Pt films offer different atomically flatness for surface smoothness and different catalytic surfaces.

2.3.1 Orientation-sensitive growth of graphene on platinum thin films

CVD-graphene synthesis on GGPt (200) and (220) films showed an improvement in graphene crystallinity as a function of increasing temperature, shown in figure 2-8. High quality of graphene was maintained at relatively in long range temperature (975 ℃ to 1015 ℃). The trends are well shown through ratios of the representative Raman intensity of D-bands, G-bands and full width at half maximum (FWHM) results of 2D-bands as temperature. The intensity ratio of D to G bands implies relatively low defect density and high crystallized graphene which was obtained. The 2D peak (2678 cm^{-1}) FWHMs of graphene on GGPt(200) and (220), measured at 31±0.1 cm^{-1}, present ideal value over 975 ℃ for growth of graphene. Furthermore, a well-fitting 2D-band in 975 ℃ growth temperature, it shows a single Lorentzian curve, which is evidence of a uniform monolayer in the resulting graphene sheets (figure 2-9).[40] In short, results of Raman spectrums show G-bands (～1580 cm^{-1}), G*-bands (～2450 cm^{-1}) and 2D-bands (～2700 cm^{-1}). In addition, the G*-bands have small intensities which originate from in-plane phonons, but the G*-band has relatively clear and sharp features in monolayer graphene. The monolayer could also be identified by calculating the intensity ratio of the G and 2D bands (~0.5). The 2D-band fittings with single Lorentzian curve centered at 2680 cm^{-1} are presented in both GGPt(200) and (220). At the result, the 2D-band does not show split for small strains. Even though the GGPt films were dependent upon their orientation, the resulting graphene layers were identified as being predominantly single layer. The GGPt film with a high melting point of 1,768 ℃ and a low TEC of ~11 um m^{-1} K^{-1} at 1000 ℃ contributed to graphene with low defects. However, the formation of graphene on GGPt film was quite sensitive to orientation, as shown in (figure 2-10). In order to observe the relationship and precise mechanism for graphene growth with GGPt film's orientation, orientations of (200) and (220) were used and compared by EBSD mapping analysis. In all instances, graphene was grown at a temperature of 975 ℃ for 10 min in order to ensure full coverage, particularly in the case of GGPt(220). As a result, each GGPt film produced a different graphene morphology. The monolayer graphene films grown on GGPt(200) contain a high density of multi-layer graphene flakes on monolayer graphene, but uniform monolayer was taken on Pt(220). This revealed an unusual property, the metal catalyst surfaces morphology depends on their orientation. From the high resolution x-ray diffraction patterns (HR-XRD) analysis shown in figure 2-6, I found out both GGPt(200) and a small portion of

(111) growth coexist together. In the electron backscatter diffraction (EBSD) map image corresponding to inset SEM image of graphene on GGPt(200) has also shown a small portion of (111) orientation (figure 2-10 **c** and **d**). In GGPt(200), growth of these multilayer graphene flakes were found on surface steps, and grain boundaries (GBs), suggesting that the defects would be main segregation channels for C-atoms diffusing. The radius of multilayer graphene flakes on GGPt(200) surface were maintained as 5~10 um and shape was consistent to isotropic polygonal in any environmental of CVD process. Conversely, strictly monolayer graphene has been achieved on GGPt(220) film. GGPt(220) has predominantly oriented toward a single crystal direction of (110), resulting in a lower carbon diffusion barrier (~0.3-0.8 eV) and an atomically-smooth surface than GGPt(200). The most probable explanation for this phenomenon is that reservoir of interstitial carbon in GGPt(200) substrate may differ from each orientation and can result the formation of multilayer graphene flakes on continuous monolayer. In contrast, GGPt(220) with predominantly one orientation allows relatively low diffusion energy barrier and atomically-flat surface for graphene to achieve monolayer dominantly.

2.3.2 Characterizations of transferred graphene layers from texture controlled platinum films

OM images (a) and (b) of figure 2-11 depict the transferred CVD-graphene onto 300-nm–thick SiO_2/Si substrate following growth on Pt(200) and Pt(220) at 975 ℃ for 10 min (the ratio of H_2/CH_4 is 50:5 sccm). In contrast to the previously reported general transfer methods such as “the electric H_2 bubbling transfer method” or “the dry transfer method”, a novel transfer method was applied by introducing OH^- ionic transfer assisted by “thermal energy”. This transfer method is depicted in chapter 3 “Thermal-Assisted Transfer and Patterned Graphene”. The figure 2-11 (a) shows a successful transfer of monolayer graphene with the multilayer graphene flakes along texture in GGPt(200) surface. Figure 2-11 (c) summarizes micro-Raman mapping image of intensity ratio of G/2D bands and D band for the monolayer graphene with the multilayer graphene flakes on GGPt(200) surface. In Raman mapping image, light green and red sites represent the graphene flakes, and the ratio of G/2D bands remain constant over large areas within multilayer graphene flakes several square micro-meters in size. In addition, the arrows in figure 2-12 indicating multilayer graphene flakes on Raman mapping image suggest that multilayer graphene flakes was grown along the grain boundaries (GBs) and demonstrate that the possibility of preferable segregation of C-atoms may occur more often than other sites. For verification, density of GBs controlled graphene on GGPt(200) surface was transferred to the substrate and analyzed with Raman spectrums. Generally, higher density in GB resulted in more single crystalline structure. The uneven layer thickness distribution was further confirmed by Raman spectra (figure 2-12). It indicates that all the measured Raman spectra showed a negligible D-band at ~1350 cm^{-1} (0.03 of D/G ratio), which indicates high crystal quality of the transferred graphene layers. Unlike in GGPt(200), the graphene growth on GGPt(220) was observed to be predominantly in the form of a

monolayer (figure 2-11 (b)). It can be noted that although graphene grown on GGPt has 50 nm valley like morphology from unexpected etched rhombus-shaped pits by oxygen escaping as gas (figure 2-6 f), no wrinkles were observed on graphene grown at Pt (220) (figure 2-11 b). The origin of the wrinkle formation might have occurred from relaxation of compressive stress induced by distinct thermal expansion coefficient (TEC) between Pt film (~11 um m^{-1} K^{-1} at 1000 ℃) and graphene (~6.5 um m^{-1} K^{-1} at 1000 ℃), or could have induced by a rather high surface roughness of the GGPt films with low melting temperature. Most of the wrinkles in graphene resemble the typical projection of one-dimensional line defects in a crystal, and the winkle can cause unnecessary defects such as folding, tears, and ripples. However, the macro-scale OM image and Raman mapping images in figure 2-12 **b** and **d** show wrinkles, tears, and ripples free monolayer. The graphene layer can also be transferred onto transmission electron microscopy (TEM) Au grids to confirm the domain size of graphene grown on GGPt(220). The low-magnified TEM image in figure 2-13 displays a typical sheet structure of graphene with domains having an area of several of square microns, but no wrinkles were presented. The selected area electron diffraction (SAED) data displays two domains of diffraction pattern, indicating a fully covered monolayer. Notably, the TEM view suggests the well-transferred graphene domains perfectly retain their original shapes. These observations are significant, as previous research has already shown that the electrical properties can be enhanced by reducing the wrinkle density. For analysis of electrical properties of transferred graphene layers from GGPt(200) and GGPt(220), the I-V curve of a source-drain with a 1 cm^2 area was analyzed by using van der pauw method (figure 2-14). The average sheet resistance (~200 Ω/sq) was obtained from graphene grown on GGPt(220) than GGPt(200) (~ 350 Ω/sq) films. As shown carrier motilities plots of transferred graphene layer with a 1 cm^2 area in figure 2-15, the most suitable graphene from GGPt(220) (~8,500 cm^2 V^{-1} s^{-1}) exhibits a carrier mobility 1.7 times greater than transferred graphene layer from GGPt(200) (~5,500 cm^2 V^{-1} s^{-1}) film. The carrier mobility of graphene channel with length of 200 μm demonstrates that our graphene has an improved crystal structure. In recent researches admit that multi domain boundaries may lead to the carriers being trapped periodically in graphene domains, the reports of carrier mobility are not that much greater than theoretical value for graphene large domain. In a sense, increasing graphene domain size is not enough to meet the industrial optimization criteria. Here, I suggest two major reasons which induced enhanced crystallinity and electrical properties for the monolayer graphene form GGPt(220) than the (200). One of the reason is that the GGPt(220) with highly oriented single-crystal induces growth of high-quality graphene by reducing the line defect since the line defects in graphene can be generated by different crystal orientation. A difference of lattice orientations between metal and graphene may lead to domain boundaries of graphene. Therefore, a line defect appears when graphene grains coalesce with differing orientations. And the influence of surface diffusion barrier energy for C-atoms is another reason why the difference of properties of graphene is even more remarkable. Using calculated atomic models of graphene on Pt surfaces with different preferred orientations, it was confirmed that the carbon diffusion

barrier energy follow the controlled Pt orientation using density functional theory. Unlike in GGPt(200) with only one C-diffusion pathway (Hollow to Hollow 1.524 eV), GGPt(220) has a lower the C-diffusion barrier energy and has a several pathways (In-channel 0.841 eV, Cross-channel 0.358~1.106). Thus, some C-atoms originating from the higher barrier energy on GGPt(200) surface do not be crystallized for graphene. It indicates the improved surface perfectness, decreased lattice mismatches and the number of GB of Pt by texture-controlled giant grain growth, which suppresses the undesirable, inhomogeneous carbon atom precipitation, enabling us to grow well-crystallized, homogeneous monolayer graphene films. In addition, the imperfect crystal can be induced the zero-dimensional defect such as an atom dangling bonding, or a carbon atom vacancy for crystallization of graphene structure. The result induce the line defects and disruptions such as wrinkles, ripples, and folding that adversely affect electrical properties of the graphene through the trapping or scattering of the charge carriers. For visualization of wrinkle-free graphene grown on GGPt films, figure 2-17 is presented by comparing graphene/transferred graphene form Cu foil and GGPt films. the result in figure **a** shows the surface characterization of as-grown multilayer graphene flakes/monolayer graphene using copper foil before transfer, where the graphene wrinkles are presented in micro-scale. The graphene films were transferred onto SiO_2/Si substrate to confirm the wrinkles of graphene. The OM image in **b** shows a typical graphene sheet structure with wrinkles for copper foil, but the OM image of graphene/GGPt films does not show the observable wrinkles in figure 2-17 **c-f**. Through the next chapter, these results from the improvements in our transfer method also coincide with an increment in the electrical properties by reduced wrinkle formation.

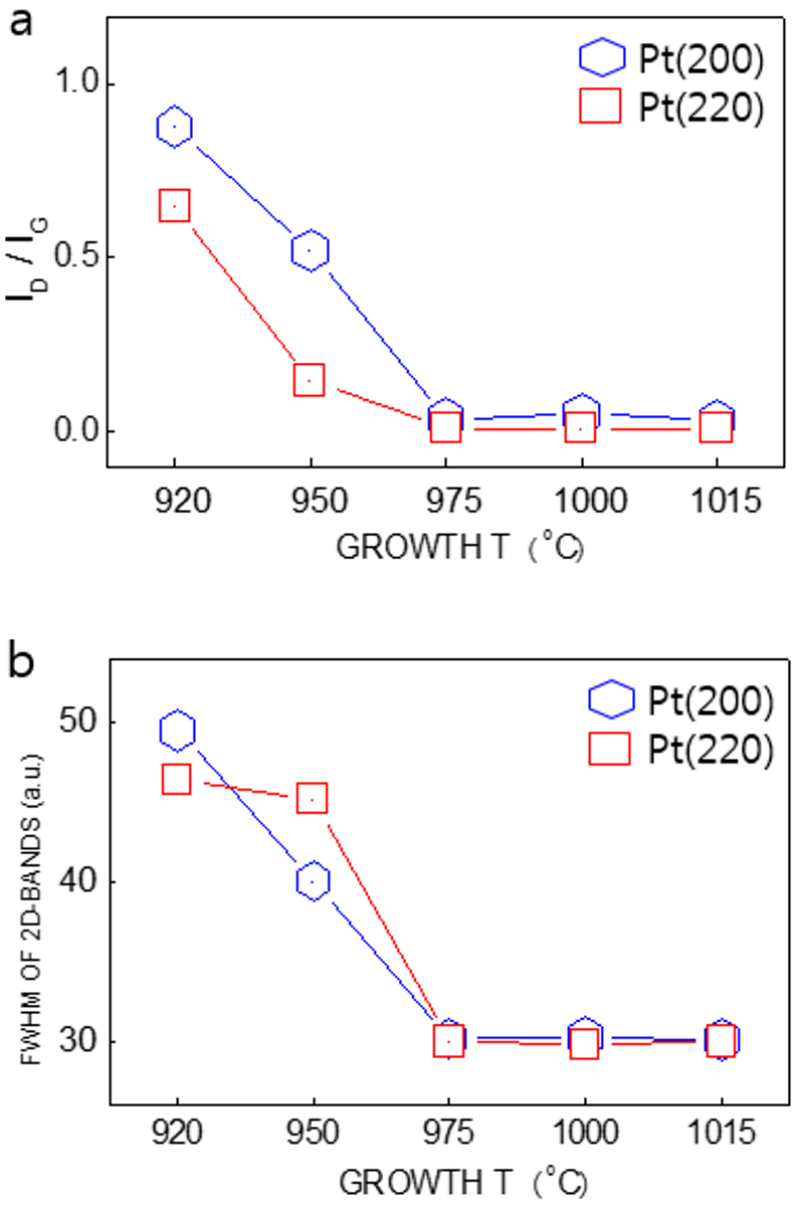

Figure 2-8. Trend of Raman spectrums of graphene with respect to long range temperature (920 ℃ to 1015 ℃) in CVD process. (a) Intensity ratio of Raman D-bands and G-bands. (b) Full width at half maximum (FWHM) of Raman 2D-bands.

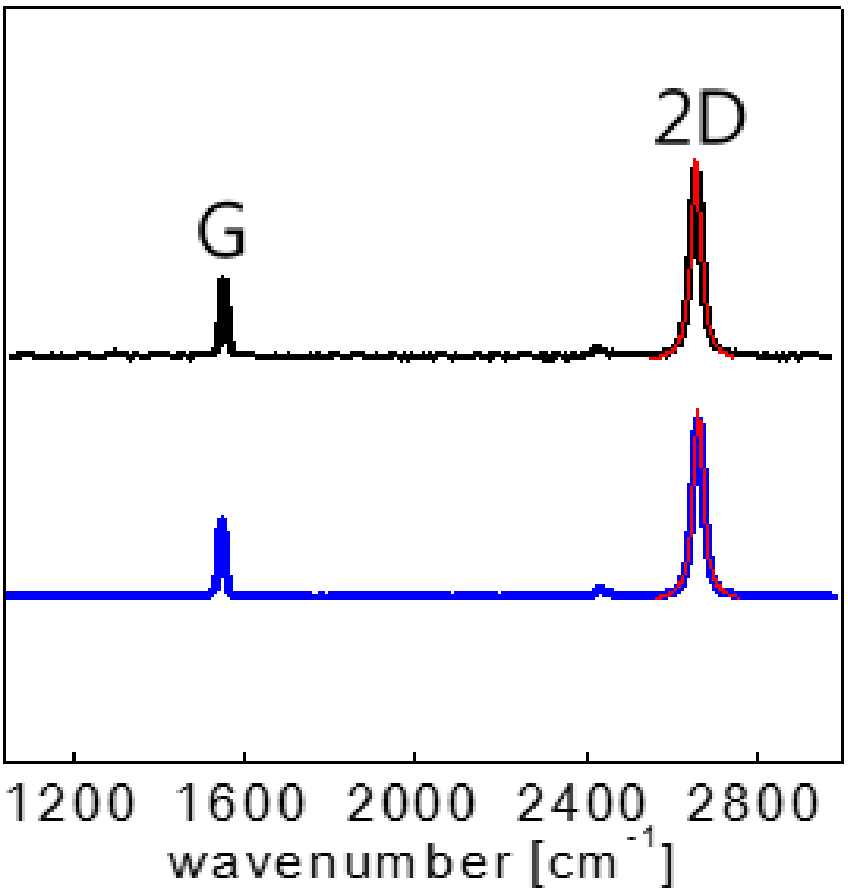

Figure 2-9. Representative Raman spectrums of graphene on the SiO_2 surface for upper Pt(200) and down Pt(220) with single Lorentzian curve.

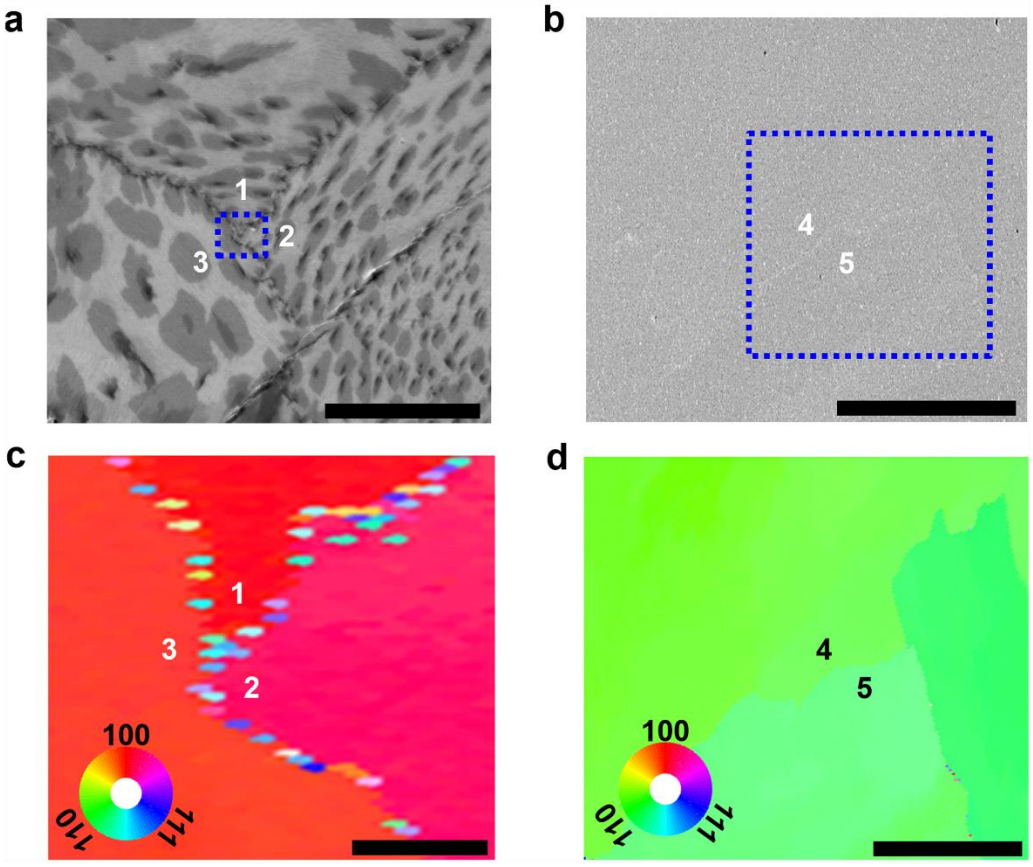

Figure 2-10. Orientation sensitive graphene films grown on GGPt (200) and (220) films. **a** and **b** show representative SEM images of monolayer graphene on (a) GGPt (200) and (b) GGPt (220) surfaces (Scale bars: 100 μm). **c** and **d** show corresponding EBSD mapping images from signed dot boxes of **a** and **b** (Scale bars: 10 μm).

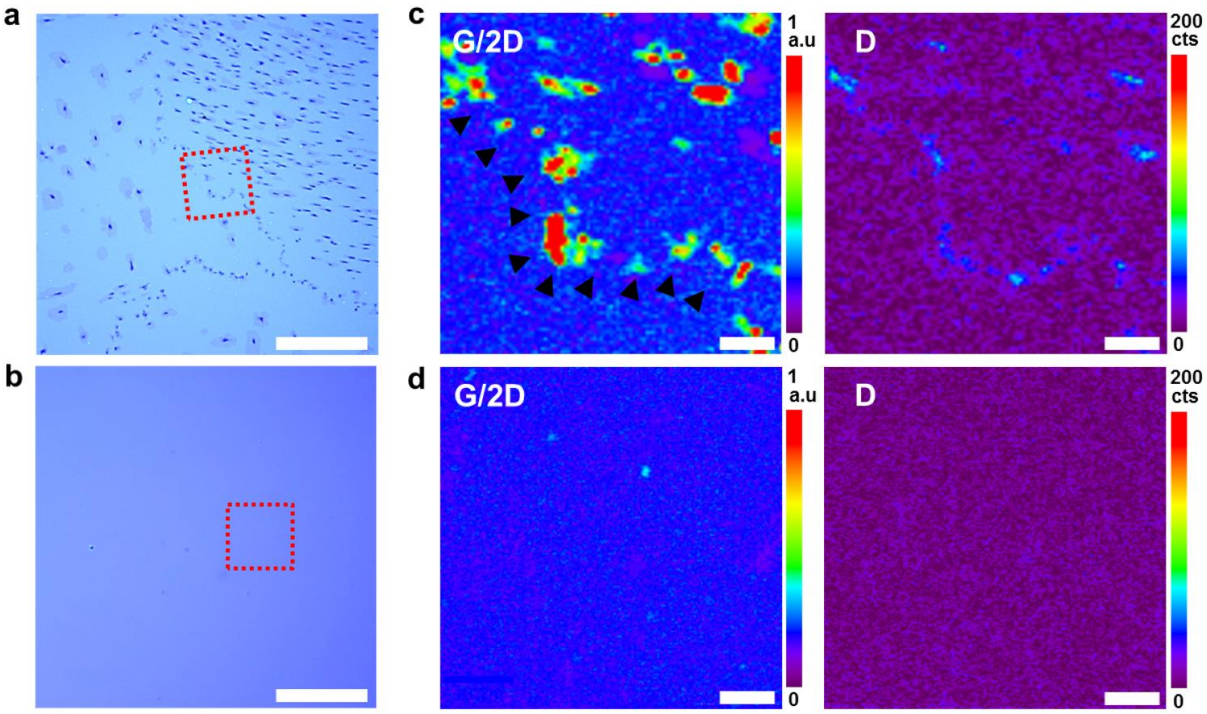

Figure 2-11. Crystallinity of transferred graphene from GGPt (200) and (220) thin films. **a** and **b** show OM images of a large-scale graphene with flakes on SiO_2/Si substrate for (a) GGPt(200) and (b) GGPt(220) (Scale bars: 50 μm). **c** and **d** show corresponding Raman mapping images from signed dot boxes of **a** and **b**. Raman mapping showing the ratio of the G/2D bands and D band for (c) graphene with multilayer graphene flakes versus (d) strictly monolayer on SiO_2/Si substrate (Scale bars: 5 μm).

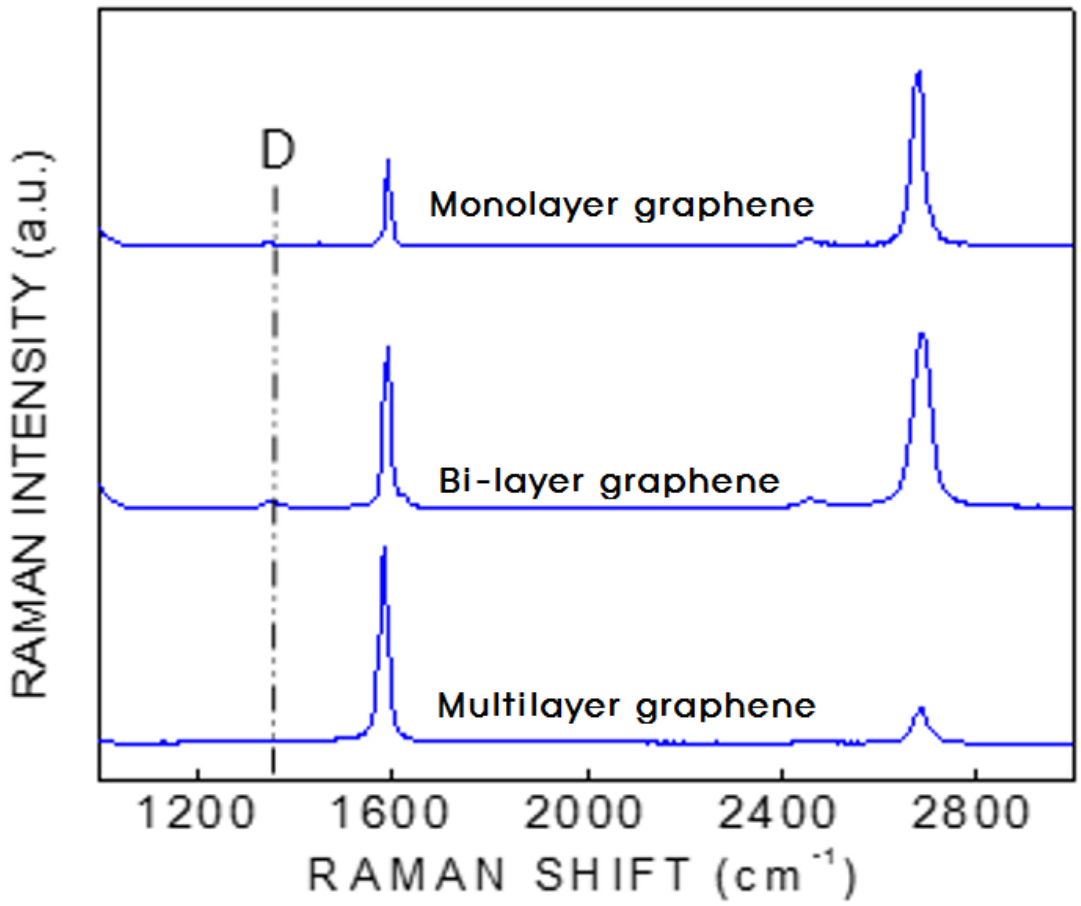

Figure 2-12. Representative Raman spectrums for comparison monolayer, bi-layer, and multilayer graphene or graphene flakes on SiO_2/Si substrate.

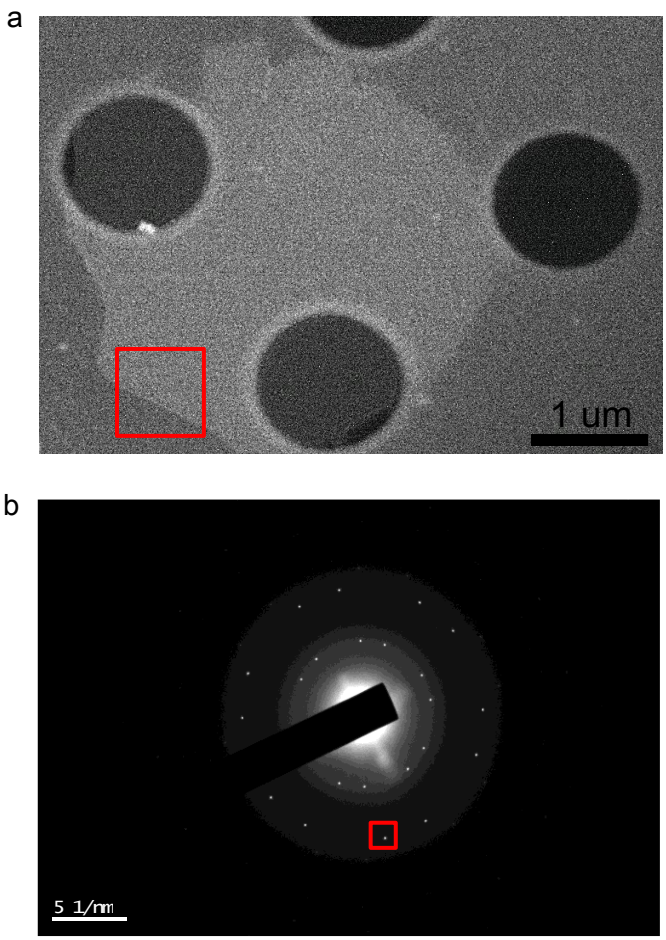

Figure 2-13. (a) Typical low magnification plan-view transmission electron microscopy (TEM) image of graphene grown on Pt(220) then transferred to TEM support hole. (b) The selected area diffraction patterns corresponding to a red box in inset of image **a**.

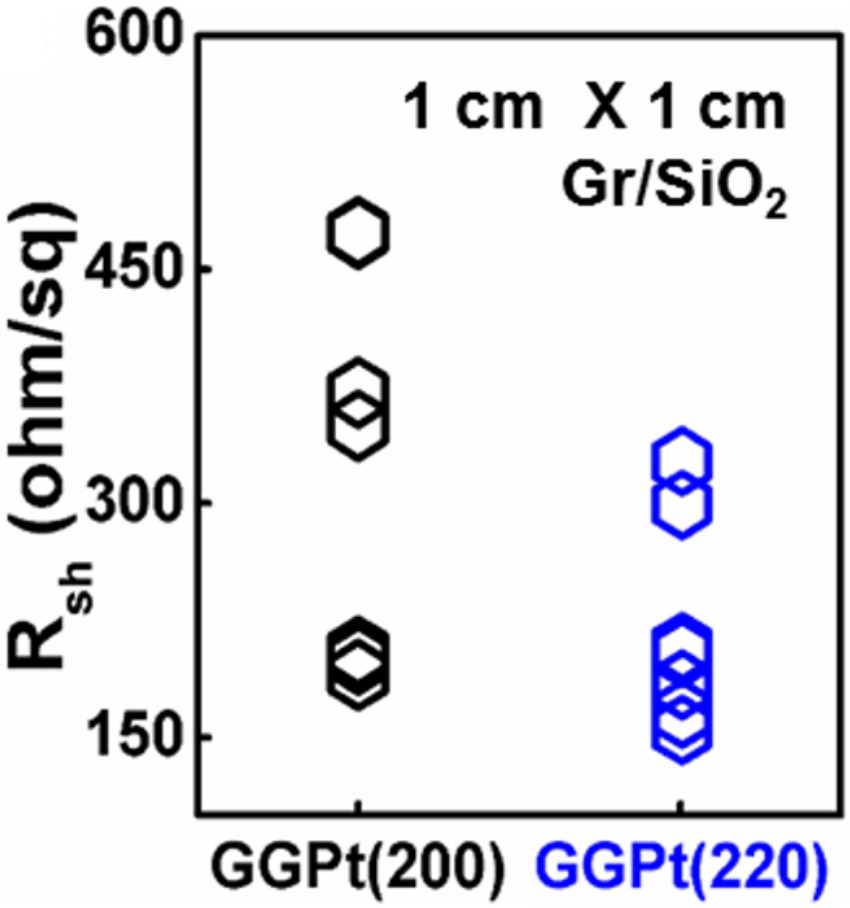

Figure 2-14. Sheet resistance (R_S) averages of 1cm^2 area transferred graphene layers from GGPt(200) and (220) films. The R_S were measured by I_{DS}-V_{DS} curves.

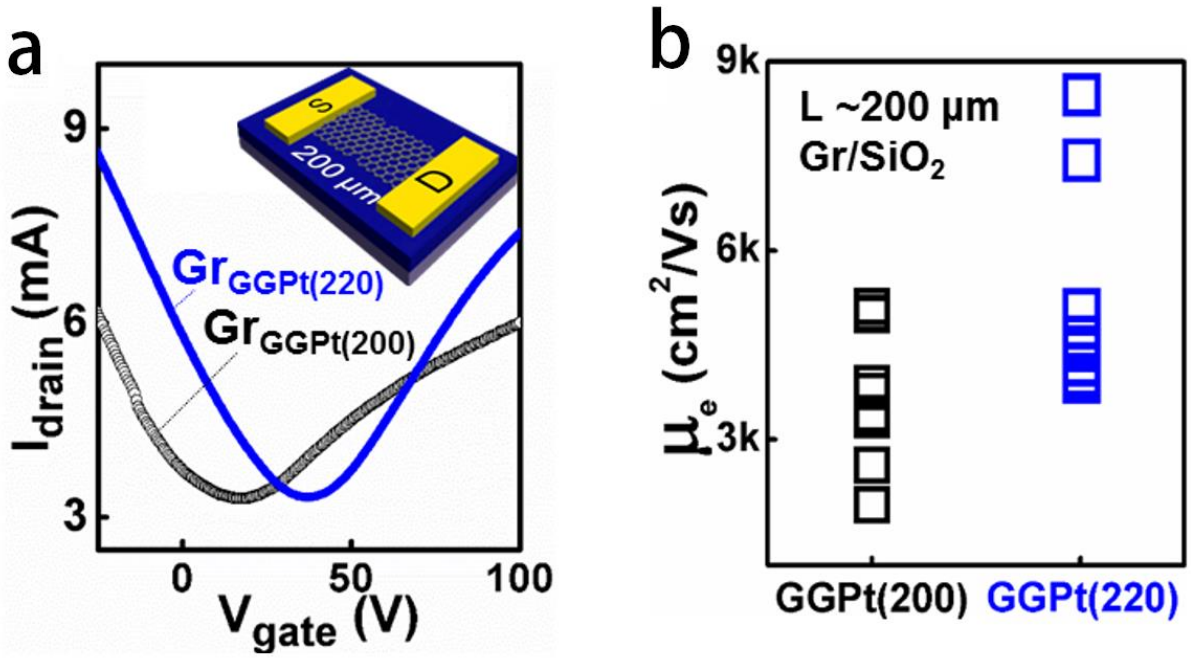

Figure 2-15. (a) Representative I_{DS}-V_{DS} curves of transferred graphene layers from GGPt(200) and (220) films. (b) Comparisons of 1 cm^2 area carrier mobility plots measured from I_{DS}-V_{DS} curves.

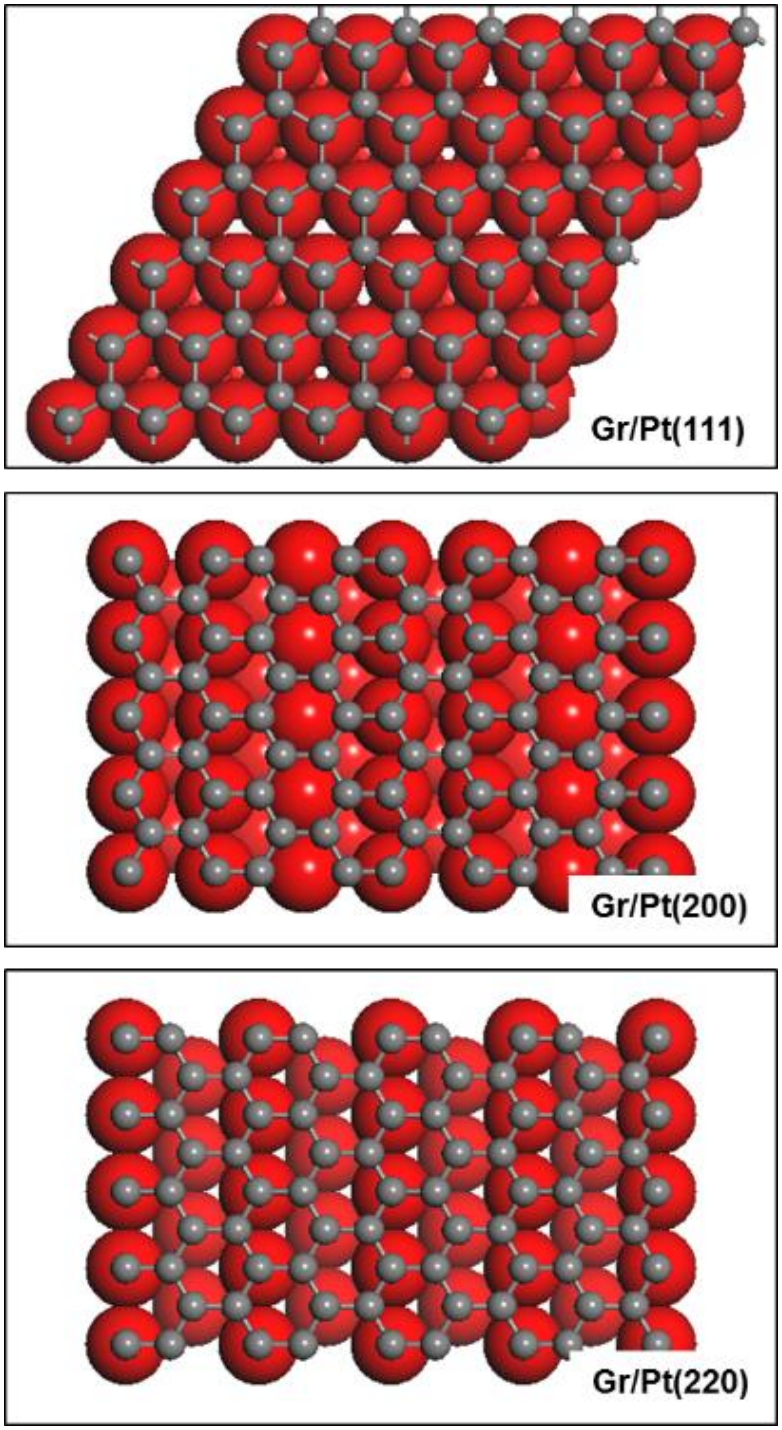

Figure 2-16. Atomic calculated models of graphene on Pt surfaces with different orientations. The calculation of lattice constant differences of different preferred oriented Pt to graphene are Gr/Pt(111) ~12.6 %, Gr/Pt(200) ~30 % and Gr/Pt(220) ~-8 %, respectively.

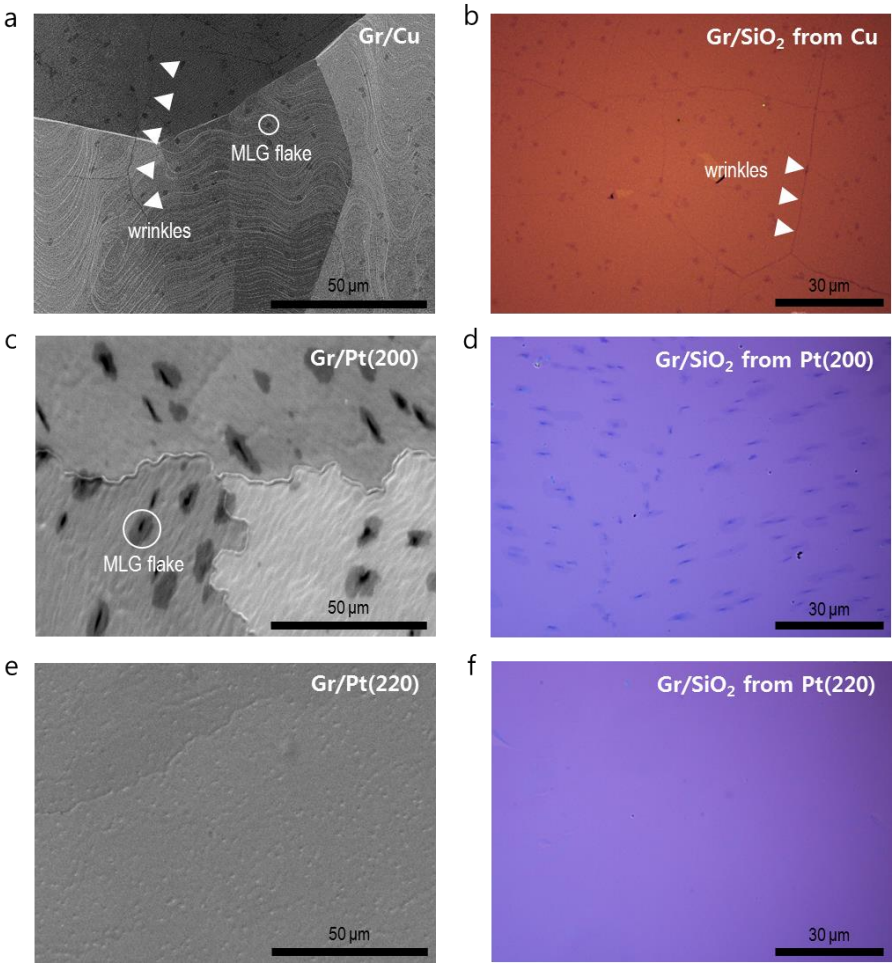

Figure 2-17. Comparisons of graphene wrinkles from Cu foil and Pt thin films. FE-SEM images of large area (a) multilayer graphene flakes/monolayer with wrinkles on the Cu foil using CVD process in H_2 gas (5 sccm) and CH_4 gas (10 sccm) at 1000 ℃ for 30 min, and (b) OM image of transferred graphene on SiO_2/Si. (c) Large area multilayer graphene flakes/monolayer without wrinkles on the GGPt (200) using CVD process H_2 gas (50 sccm) and CH_4 gas (5 sccm) at 975 ℃ for 10 min, and (d) transferred graphene. (e) Strictly monolayer graphene without wrinkles on GGPt (220) film, and (f) transferred graphene.

2.4 Conclusions

In this chapter, a key strategy was applying the texture-controlled Pt films for growth of wrinkle-free graphene and strictly monolayer graphene. The Pt films had both preferred orientation and giant grains. The growth of Pt grains indicated the minimized number of GBs. From these results, the CVD graphene showed orientation sensitive strictly monolayer and wrinkle-free graphene forms on the texture controlled Pt(200) and (220) with giant grains (GGPt). The each samples offer different atomically flatness for surface smoothness and different catalytic surfaces. Therefore, I'd like to summarize by saying that. First, an interest of Pt stems from the facts that Pt is an inoxidizable metal and possesses much lesser difference in TEC to graphene, which will markedly decrease the generation of crystalline defects in the resulting graphene sheets. Second, improved the surface perfectness and limit the number of GB of Pt by texture-controlled giant grain growth suppress the undesirable, inhomogeneous C precipitation, thus enabling us to grow well-crystallized, homogeneous monolayer graphene films. Third, transferred graphene shows almost wrinkle-free characteristics regardless of the orientation types of GGPt, probably due to much lesser difference in TEC (thermal expansion coefficient) to graphene.

Chapter 3. Thermal-Assisted Transfer and Patterned Graphene

3.1 Introduction

Compare to graphene on Cu, graphene on Pt can be seen that the higher efficiency in industrialization aspect can be shown for graphene on Pt for mass production. However, lack of various transfer methods is problematics for graphene on Pt films since the Pt shows excellent corrosive property and noble properties to oxidation. For this, a new transfer method was used for the graphene on GGPt films.

3.1.1 Transfer method for CVD-grown graphene

A CVD-grown graphene transfer method is well-known for graphene/Cu[41] or graphene/Ni[42,43]. Figure 2-18 shows representative transfer methods for graphene production: Removal of catalysts using a supporting layer (chemical etching[41,42], electric bubbling[31]) and dry transfer (reactivity assisted dry transfer[44], PDMS stamping[43], thermal release tape[45]). In the removal of catalysts, the supporting layer uses conventionally poly(methyl methacrylate, PMMA) coated graphene to a SiO_2/Si as target substrate.[41,42] Using this transfer method, a layer of polymeric supporting layer is spin-coated or dip-coated onto the graphene/catalyst substrate. And a chemical etching is applied for removal of metal catalyst. But the resulted graphene layer has mild metal residues due to the imperfect metal etching. Subsequently, the polymeric supporting layer/graphene stack is transferred to target substrate. After then, a solvent is applied for removal of the polymeric supporting layer. However, the resulted graphene layer has mild residues since the imperfect removal of polymeric supporting layer.[41] In addition, there are limit of danger acidic etchants and impossibility of using noble metals in this method. Especially, a case of graphene/Pt is usually impossible to separate between graphene and Pt surface for graphene transfer due to the Pt having excellent corrosive property and freely oxidation. For these limitations, the dry transfer methods was introduced such as thermal release taping method. A releasable tape is placed on graphene/catalyst. For a uniform force onto tape/graphene/catalyst stack, a heating pressure and an evacuation of the bonding chamber is applied. This step should be take care of applying force to improve adhesion and remove air pockets. After then, the tape/graphene is lifted from catalyst surface, which is placed onto target substrate. Finally, the tape is released, using the release temperature. This method is easy and a freely available from dangerous chemicals.[45] However, this method shows low residue in resulted graphene layer, but the transfer area is limited. For the limitations, a new transfer method is applied to the graphene transfer from GGPt films.

A. Example of polymeric supporting layer based transfer method of graphene films grown on Ni or Cu.[42]

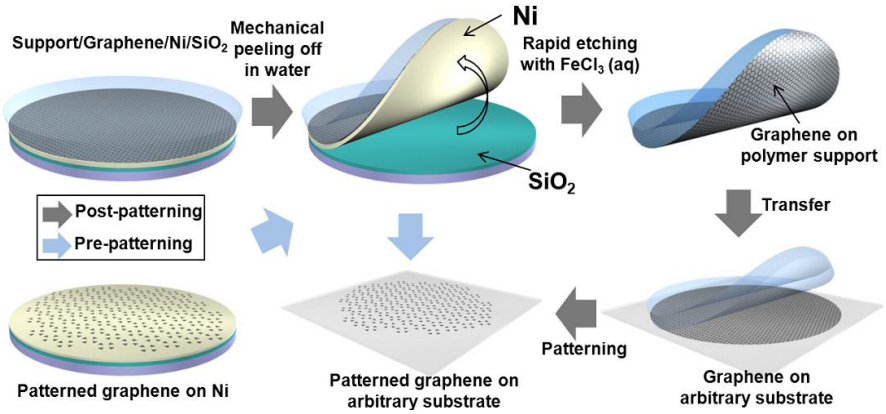

B. Example of dry transfer method of graphene films grown on Ni.[43]

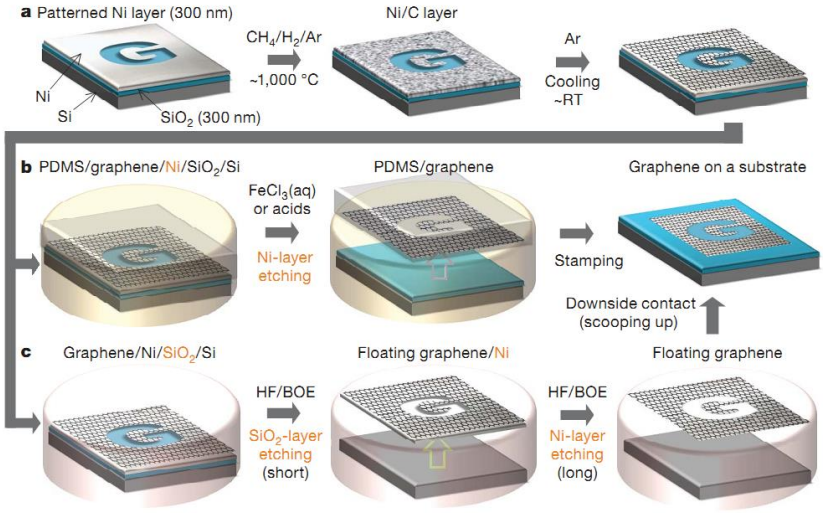

Figure 3-1. Representative conventional graphene transfer methods.

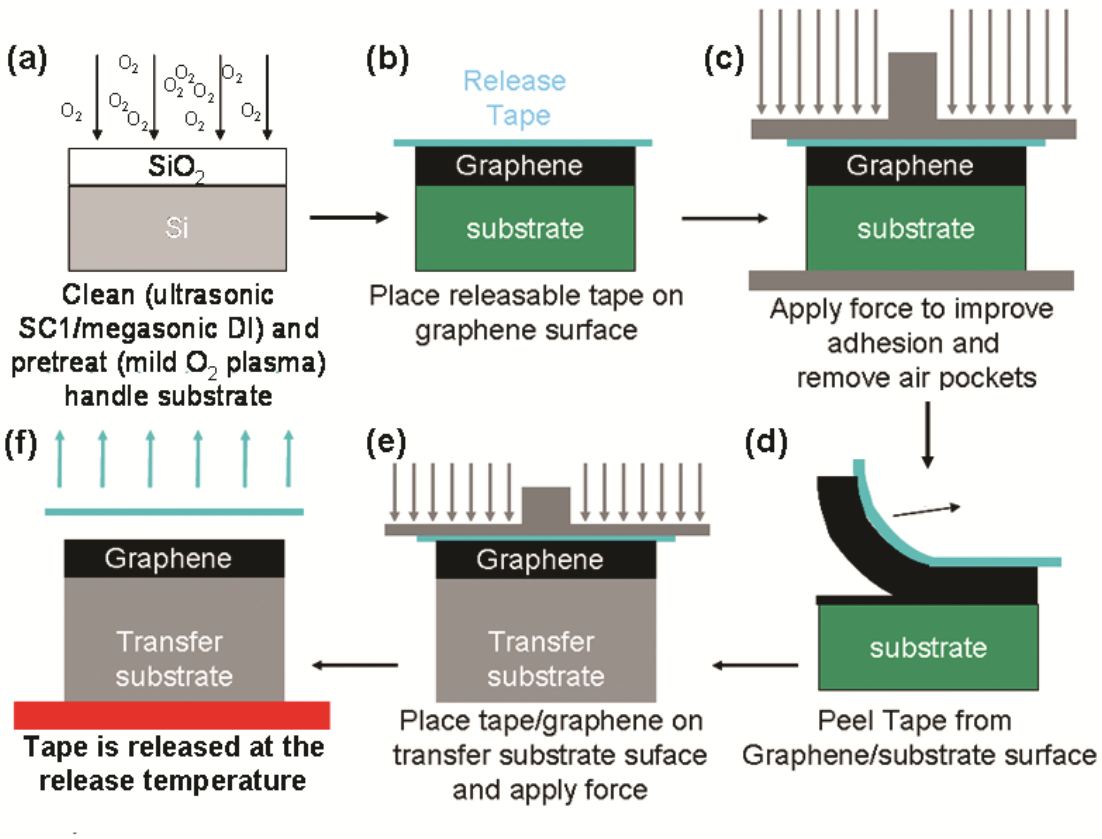

Figure 3-2. Example of thermal release taping transfer method.[45]

3.2 Experimental section

In this section, an advanced transfer method using "near boiling temperature by using NaOH solution with help of thermal energy" is introduced to overcome the limitation of previous transfer methods.

3.2.1 Thermal-assisted transfer method

To transfer graphene from GGPt films and patterned Pt films with SiO_2 regions, the top of the graphene was coated with PMMA [poly(methyl methacrylate), 75,000 GPC molecular weight, 10 wt.% in toluene] at 4,000 rpm for 1 min. Before the coating step, the graphene/GGPt sample side was blocked by Kapton tape. It was fairly efficient to reduce the progress time. After removal of the kapton tape, the PMMA/graphene/GGPt stack was cured at near 135 ℃ for 10 min using a hot plate. Subsequently, the PMMA/graphene/GGPt stack was floated on a NaOH aqueous solution at 90 ℃. The temperature was elevated from 25 to 90 ℃ during the transfer. When complete detaching the PMMA coated graphene assembly from GGPt films, it depended on molarity of NaOH solutions and the aqueous solution temperature. Averagely the PMMA/graphene can be perfectly separated within 60 min in 1 M (mol) - NaOH aqueous solution at 90 ℃. And then, the PMMA/graphene was rinsed in DI water for 30 min. Subsequently, the PMMA/graphene assembly was transferred to SiO_2/Si target substrates. After then, the PMMA/graphene/SiO_2/Si stack was dried at 40 ℃ for 30 min, and baked at 105 ℃ for 10 min with a hot plate. To improve graphene adhesion onto SiO_2/Si target substrates, the annealing is used. Finally, the PMMA was removed by acetone from graphene/SiO_2/Si substrate. The thermal-assisted transfer method allows the transfer for large-scale patterned graphene onto target substrates and is a non-destructive transfer process. Also, this transfer method allows the resulted graphene layer without any wrinkles or ripples formation. Besides, the thermal-assisted transfer method can be applicable to the conventional Cu based catalytic metals. But the Cu film or foil was oxidized, because the Cu has high chemical reactivity, and it is similar to the reported electrochemical transfer method such as a bubbling transfer method.

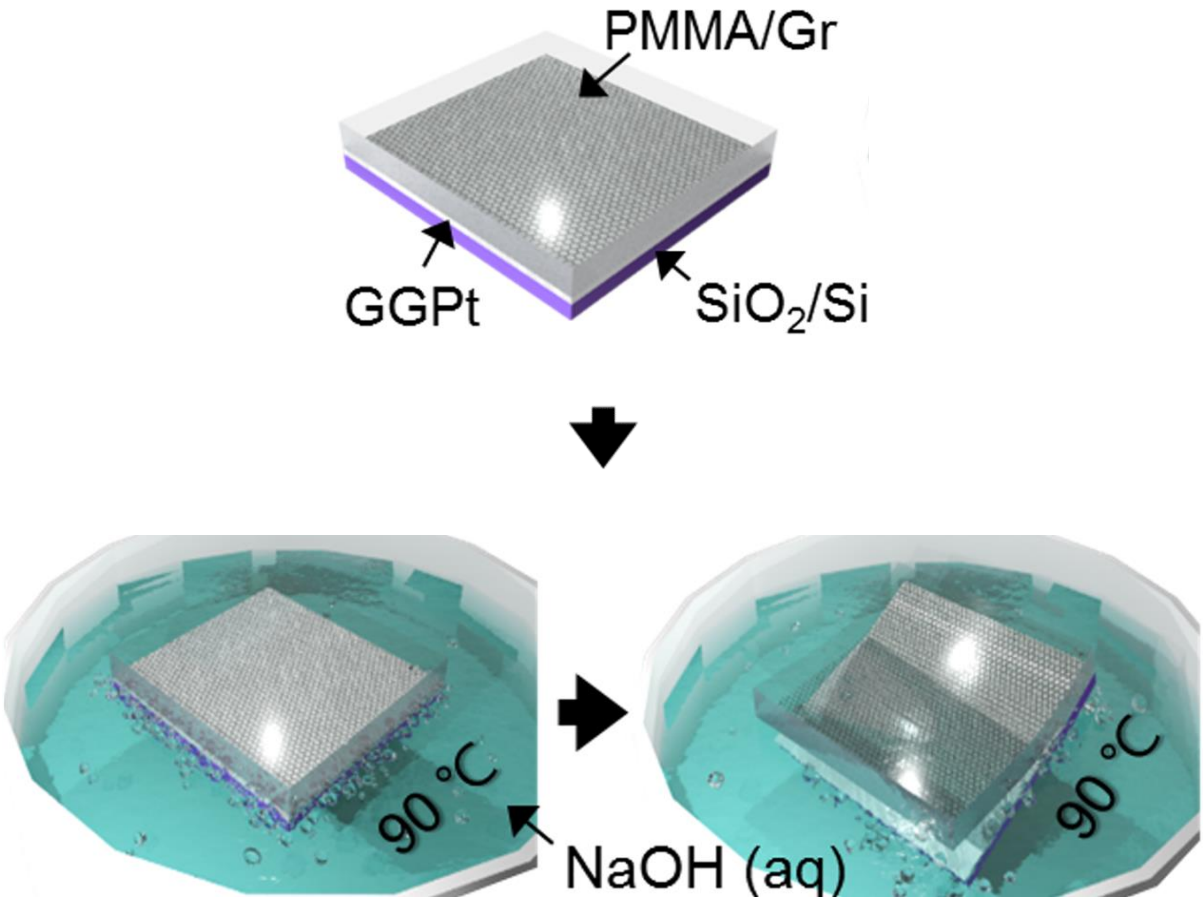

Figure 3-3. Schematic diagram of aqueous solution of NaOH based transfer method of graphene films grown on GGPt/SiO_2/Si films.

3.3 Results and discussion

In this section, the introduced thermal-assisted transfer method allow to obtain tens of microns of patterned graphene transfer and show excellent in reversibility.

3.3.1 Thermal-assisted transfer

Figure 3-4 and 3-5 show that it is impossible to separate the PMMA/graphene layer from the GGPt films using heated aqueous solutions other than the NaOH, such as deionized (DI) water or NaCl. In boiling NaOH solution, the OH^- ions (hydroxide) were responsible for the reaction between the graphene and GGPt surface. Once again, the graphene/Pt interfacial reaction with the hydroxide was studied for transfer process purpose. Generally, metals are attacked by NaOH solution to form hydroxide metal (e.g. platinum hydroxide) but the attack occurs at a temperature higher than 300 ℃[46,47], which is considerably higher than the temperatures in our transfer method. The thermal-assisted transfer method shows slower process time to separate between graphene and GGPt surface than the electro-chemical bubbling transfer method. But our method shows the resulting of graphene layer without any additional defects such as tears or folds. Although NaOH solution does not attack the Pt to become the platinum hydroxide, relatively low temperature (~90 ℃) may provide enough thermal energy for OH^- ion to swim in between graphene and Pt. In the same vein, the sodium hydroxide is also frequently used as an industrial cleaning agent. It is added to water, heated, and then used to dissolve grease, oils, fats and protein based deposits, and our mechanism of the transfer use the same principle. In a similar vein, the time of separation between the PMMA/graphene from the GGPt interface strongly depends on the molarities of NaOH solutions. Figure 3-6 shows the dependence of separation time in NaOH solute morality for graphene/GGPt. By increasing the molarity of the NaOH solution from 0.5 to 4 M, the separation time was reduced by increasing hydroxide ions from ~90 to ~30 min. The separation time for graphene/Pt was saturated which is shown after 4 M of NaOH. Recent research has focused on separation using wettability between graphene and metal surface. However, the force by wettability was more sensitive to substrate morphology, where graphene on rough surfaces resulted in tears. On the other hand, the thermal-assisted transfer process could prevent additional damages on both graphene and GGPt films. The evidence is admitted by analyzing of Pt-4f XPS spectra in figure 3-7. The Pt-4f XPS spectra were taken at the same time, following a pristine Pt, graphene/Pt, and graphene-free Pt after transfer process. The spectrums revealed the Pt-$4f_{5/2}$ peaks at binding energy of 74±0.2 eV. In addition, changes in the relative intensities of the Pt-$4f_{5/2}$ and Pt-$4f_{7/2}$ peaks were also observed. These features indicate the impurity and doping free Pt was retained.[48] Therefore, it demonstrates excellent recycle properties due to the high corrosion resistance of GGPt as a carbon catalyst.

3.3.2 Patterned graphene

Figure 3-8 shows mechanisms of the transfer process of large area graphene (I) and patterned graphene (II) from patterned platinum films. The process of patterned graphene transfer was confirmed by the following steps. A layer of poly(methyl methacrylate) (PMMA) was coated on the patterned graphene/Pt/SiO_2/Si assembly. Afterwards the patterned graphene/Pt/SiO_2/Si assembly was semi-floated on an aqueous NaOH (1 M) solution at 90 ℃, the PMMA coated graphene stack was separated from the both Pt/ SiO_2 and SiO_2 surface. During the reaction between 300 nm-thick-SiO_2 surfaces with NaOH (1M) solution at 90 ℃, the PMMA supporting layer with graphene was partially etched by sodium ions. The chemical reactions are the following:

$$SiO_2\ (s) + 2NaOH\ (l) \rightarrow Na_2SiO_3\ (s) + H_2O\ (g)$$

This is a chemical reaction in the solid state where NaOH aqueous solution and SiO_2 are fused together by heat; however, the 300 nm-thick-SiO_2 coating film react a little bit but that is enough to separate the PMMA/SiO_2 interface.[49] After separation of PMMA on patterned graphene, the stack is put in DI water and transferred to target substrate (SiO_2/Si substrate). This permits the active motion of molecules, and allows Si and Na^+ to react with each other. The OH^- ions were subsequently reacted to the Pt patterns, and the PMMA/graphene was separated from patterned Pt surface. As illustrated in figure 3-9, this transfer method is effective for the transfer of patterned graphene, and by producing strain in all directions within the PMMA on patterned graphene it inhibits the formation of wrinkles. An excellent patterned graphene was transferred on SiO_2/Si substrate after removal of PMMA (figure 3-9 **c**). From Raman spectroscopy and mapping images, the films were identified as predominantly single-layer graphene (inset of figure 3-9 **b** and **c**). This method is beneficial as it does not require wet etching of the Pt, applicable with insulating SiO_2 substrate. Compared to that electric bubbling, the used transfer method is free from damage of graphene due to slower separation time.

In order to analyze properties of the graphene grown on rectangular Patterned Pt (200), a thermal assisted transfer method was used. The patterned Pt film has qualities of multi-grained patterns (5 mm^2 ~ 1 mm^2) and single-grained patterns (2.5 mm^2 ~ 10^4 μm^2). Since the limited density of GBs, the relatively small sized patterns had single-GBs. Figure 3-10 **c** and **d** show that the micro-sized graphene layers could be perfectly transferred onto SiO_2 substrate via our transfer method. From Raman spectroscopy, I found that the poly-crystalline graphene was grown onto the single-grained Pt patterns. In contrast, the monolayer mostly at multi-grained Pt patterns. On the basis of the results, I suggest that a nucleation of graphene on Pt should be associated with preferred oriented morphologies for C-atoms diffusion, such as terraces and GBs in the Pt films.

Also, I have demonstrated recycle ability of patterned Pt film. The re-grown graphene at the same CVD condition was transferred by using a NaOH solution at 90 ℃. Figure 3-11 **c** indicates the properties of graphene as number of re-growth. Raman intensity ratio of the D and G bands was maintained low values regardless of the recycled process. Intensity ratios of the G and 2D peaks have shown similar results. Little increased in sheet resistance of the graphene films is negligible. Consequently, our transfer method could also help to overcome additional damages of the Pt film.

3.3.3 In-situ growth of graphene on sintered platinum film and its crystallinity

Among the excellent graphene properties, its hydrophobic surface and mechanical/chemical stabilities allow the water desalinations or distillation. Especially a fabrication of porous graphene, it could be used as an effective water desalination membranes.[50] Recently, there are various ongoing researches for super-hydrophobic membrane, membrane distillation around the world. Specially, there are research groups working on graphene to replace the previous membrane rarely.[50,51] Due to the nearly total lack of research such as desalination, nonetheless, it is difficult to get near the commercialization. Besides, super-hydrophobic graphene is difficult to grow. In these regards, the underlying cause is that graphene defects disappeared without a trace after growth. In order to overcome the limitation, following factors should be improved in the graphene membrane; minimum wrinkles, minimum folded, and many pores. At that same time, graphene membrane should maintain a reproducibility and economically superiority by enhancing the studying standards. In this research, I emphasized to improve graphene synthesis for high-grade graphene-based membrane. Additionally, graphene-based membrane is a breakthrough technology to solve the wetting property and inefficiency as the main factors impeding the commercialization of membrane distillation (MD) process over the past 30 years. If evaluation of the graphene-based membrane is to be effective, this process will allow the desalination or concentration of waste water and derelict-gas-liquid filtration. Besides, this research is expected to obtain creative knowledge through technologies such as growth of graphene films at low temperature, patterning of graphene, and organic membrane transfer. Membrane distillation (MD) has meant that phase changes occur at hydrophobic surface of the membrane, and then a vapor goes through the process which condenses and separates the vapor via micro-pores.

There are a variety of research groups for super-hydrophobic membrane, membrane distillation around the world. Besides, there are also research groups for graphene to replace the previous membrane (table 3-1).[50-54] However, the MD process also has limitations, which have resulted in a lack of general interest in the process. The process solutions must be aqueous and sufficiently dilute to prevent wetting of the hydrophobic microporous membrane. This limits MD to applications such as desalination (currently dominated by RO), removal of trace volatile organic compounds from waste water, and concentration

of ionic, colloid, or other relatively non-volatile aqueous solutions. In these researches, membrane distillation (MD) is once again rising globally in terms of energy saving and a low cost, although MD process has a long history as an alternative to conventional separation processes such as distillation and reverse osmosis (RO). Then, membrane is at the mercy of essential factors for MD process (table 3-2). More advantages of MD process than other separation processes stem from: (1) Perfectly rejection of ions, macro-molecules, colloids, cells, and other non-volatiles, (2) lower operating temperatures than conventional distillation, (3) lower operating pressures than conventional pressure-driven membrane separation processes, (4) reduced chemical interaction between membrane and process solutions, (5) less demanding membrane mechanical property requirements, and (6) reduced vapor spaces compared to conventional distillation processes. In the graphene based porous membrane, an effectiveness of water desalination or distillation is very sensitive to the pores. In other words, the desalination abilities are strongly affected by pore sizes, pore densities, chemical functionalities, and endurance against applied pressure (figure 3-12).[51] Therefore, the synthesis of porous graphene layer is hard to get in the conventional CVD method using Cu or Ni catalyst. Previous conventional methods to achieve hydrophobic surface suffer following problems; complex process, expensive, limited scale, and harmful. But the graphene layer can be overcome such limitations.

In this section, I show a synthesis of porous graphene using controlled Pt (111) film. After CVD process without pre-annealing process, I achieved a fully hydrophobic graphene layer from Pt (111) film. From previous properties of Pt such as an inoxidizable metal with a high melting point, the result of graphene showed a hydrophobic surface without impurities or wrinkles (figure 3-13). As I mentioned that the Pt films have recycle ability by using thermal-assisted transfer method. The recycle ability of Pt film will be necessary to develop reproducible application, and the patterned graphene will be applied to water desalination membrane. The graphene membranes could be allowed their suitable application in the size-selective separation and flexible ability, as shown in figure 3-11 **d**. As I introduced, the Pt films included the PtO as adhesion layer between Pt film and SiO_2/Si substrate. Surely, the Pt with PtO had typical properties as shown figure 3-14. Before the graphene growth on Pt (111), I applied a pre-annealing step at 975 ℃ in hydrogen (H_2) atmosphere during 2 min ~ 2 hours. As shown figure 3-15, the properties of pore relied on pre-annealing time. Therefore, As-sputtered Pt films enable to make the pores using pre-annealing process, which allows to control density of Pt pores in H_2 atmosphere. Because the oxygen is inserted during Pt film sputtering, the Pt sintering occurs with oxygen diffusion during pre-annealing step in H_2 atmosphere. The chemical reaction of mechanism is shown in the equations.

I. At surface of Pt block

$$\mathbf{H_2 \rightarrow 2H}$$

II. At oxide-metal interface

$$\mathbf{2H + PtO \rightarrow 2Pt + H_2O\ (g)}$$

It can be described that the platinum etching event activated by hydrogen gas reaction with PtO. During pre-annealing in hydrogen gas, the reaction generates steam bubbles in PtO. Finally, the hydrogen gas makes the pores or protrusions of platinum films. Surely, when the carbon source starts to pull in CVD chamber, the reaction does not take any more. I suggest that the steam can't escape. Already, the similar theory was shown on the copper and copper oxide films.[55] From the results, I performed pre-annealing step for 4 min, subsequently graphene was grown for 10 min after feeding methane (CH_4) gas. I obtained porous graphene membrane with pore radius of ~2.5 μm and density of ~ 10^5 cm^{-2} (figure 3-16). Surprisingly, the graphene layer was formed continually on both Pt surface and pores. In order to prove that the fact, I performed the pre-annealing for 6 min. As shown figure 3-17, the characteristics of Raman spectrum show the presence of graphene inside and outside the pores. To investigate the Pt sintering, I performed the pre-annealing step for 30 min and graphene was grown for 10 min. In this result, even though I obtained graphene on Pt islands shaped film, the graphene was transferred only islands from Pt islands (figure 3-18). In special case, the transfer was allowed for graphene islands from Pt islands. Using this technique, we obtained graphene islands which will be valuable seed layers for epitaxial structures.[56,57] To investigate why the graphene exists inside the hole, the pre-annealing step was performed for long-time, subsequently graphene was grown for 10 minutes. Using the SEM-EDX analysis, I found out many small Pt particles in inside Pt pores, which acted as a carbon catalyst to formation of graphene (figure 3-19). To synthesis a perfect porous graphene membrane, the graphene/Pt islands assembly was used as shown OM image in figure 3-20 **a**. after graphene transfer onto SiO_2 substrate, the perfect porous graphene membrane was obtained by applying modified transfer method. The OM images in figure 3-20 show that graphene was successfully transferred to target substrate except for the graphene grown on the Pt islands. Consequentially, the porous graphene membrane was obtained by the Pt (111) film with a controllability of pore-density/size.

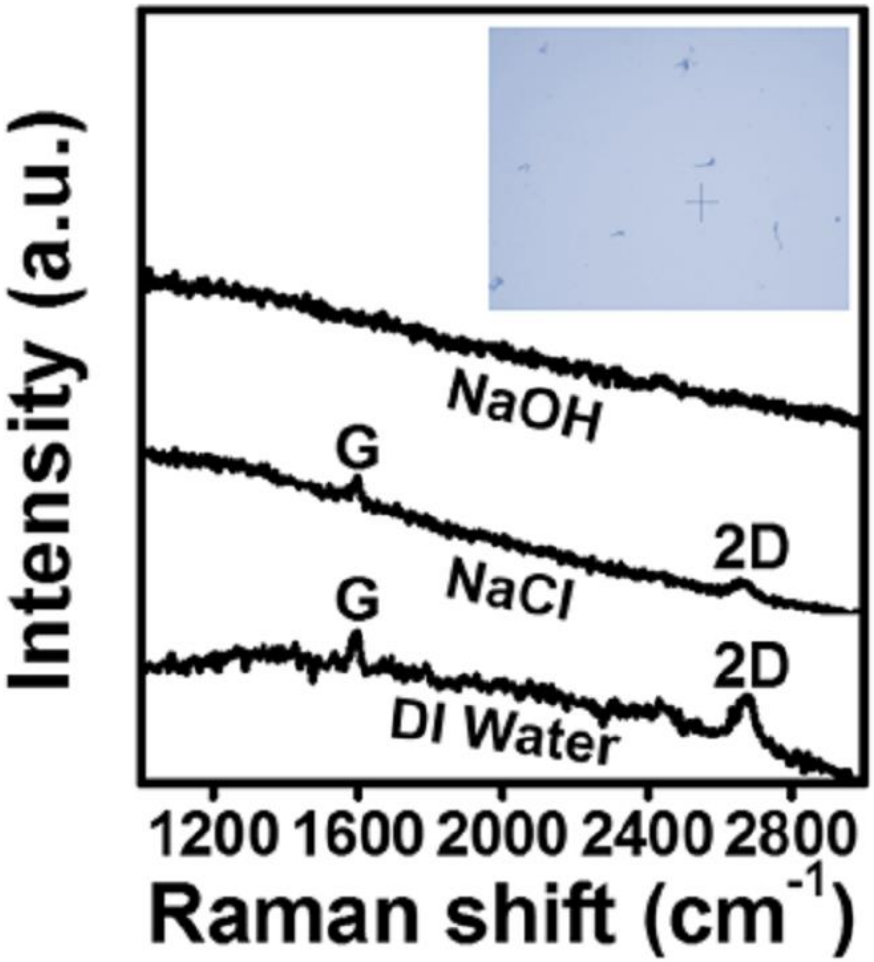

Figure 3-4. Raman spectrums for graphene on GGPt films after applying the thermal-assisted transfer process as various 90 ℃ boiling solutions of NaOH (top), NaCl (middle), and DI water (bottom). OM image of Inset shows graphene-free GGPt surface after the thermal-assisted transfer process.

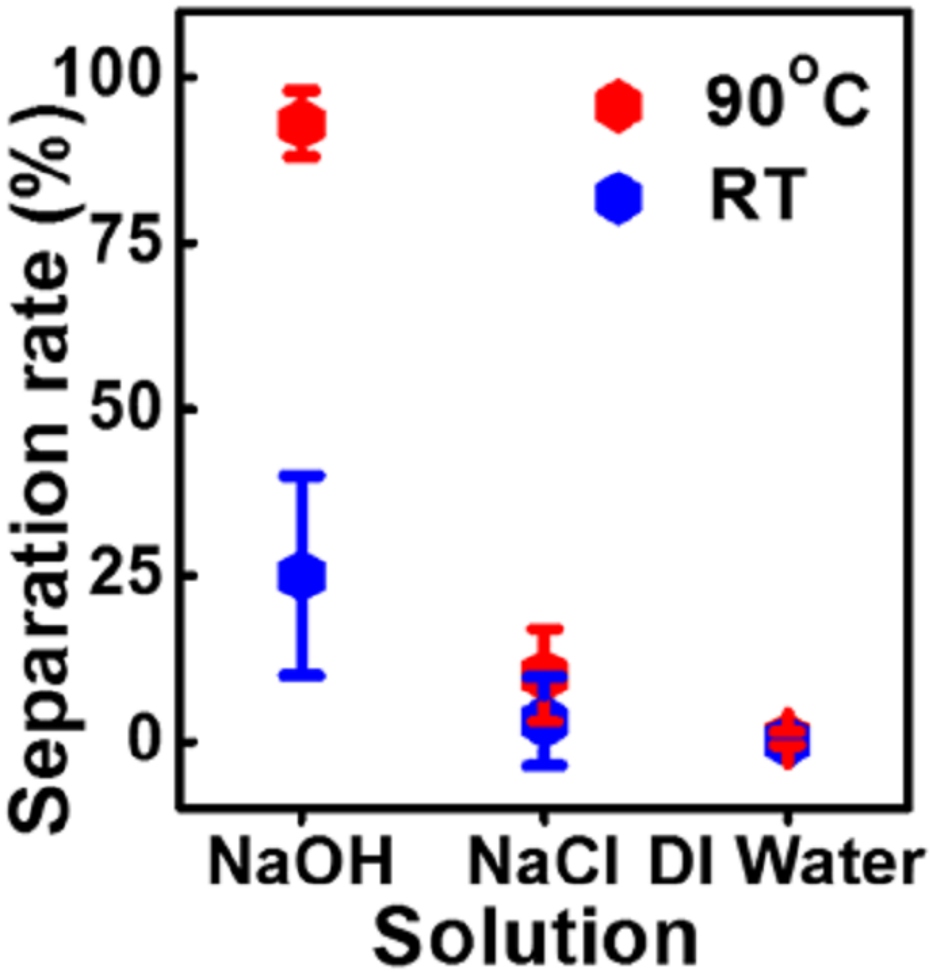

Figure 3-5. Plot of a separation rate between graphene and GGPt surface in various solution (NaOH, NaCl, and DI water) at room temperature (25 ℃) versus near boiling temperature (90 ℃).

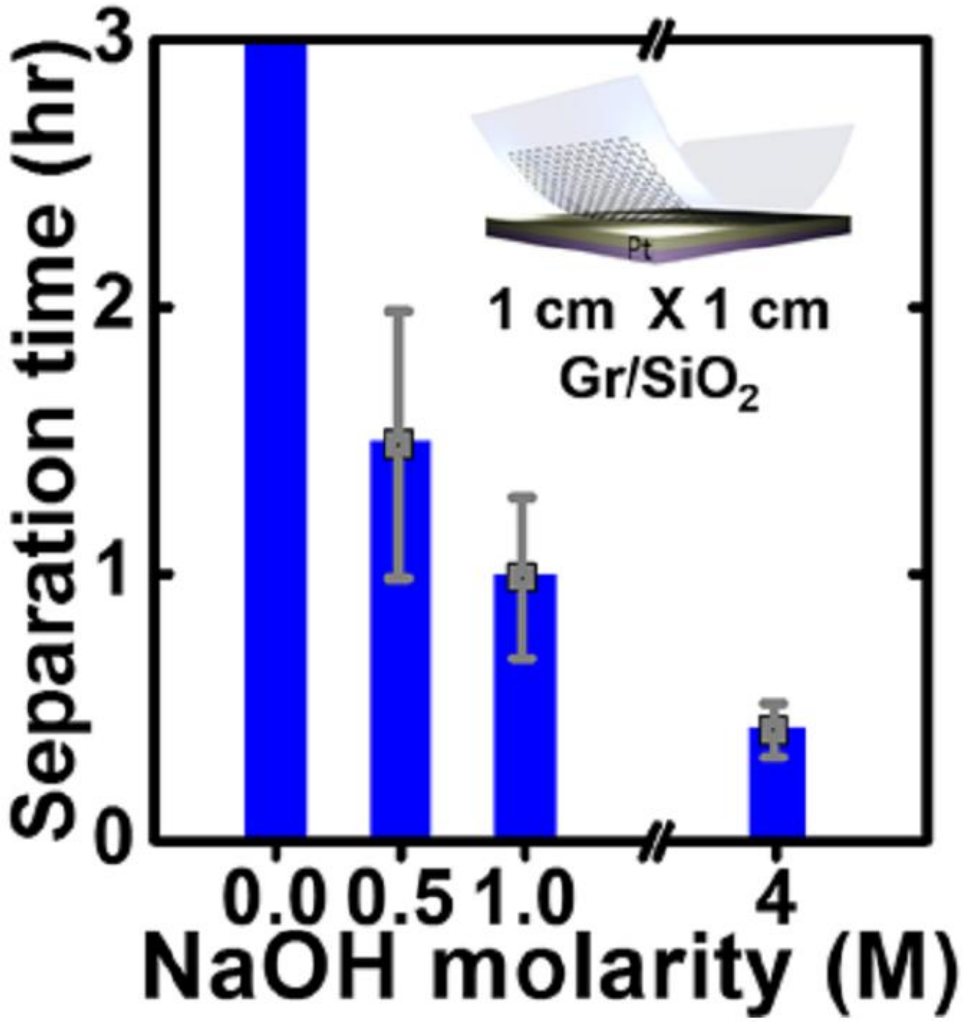

Figure 3-6. Graph of a separation time for graphene and GGPt surface under various NaOH molarities at near boiling temperature (90 ℃).

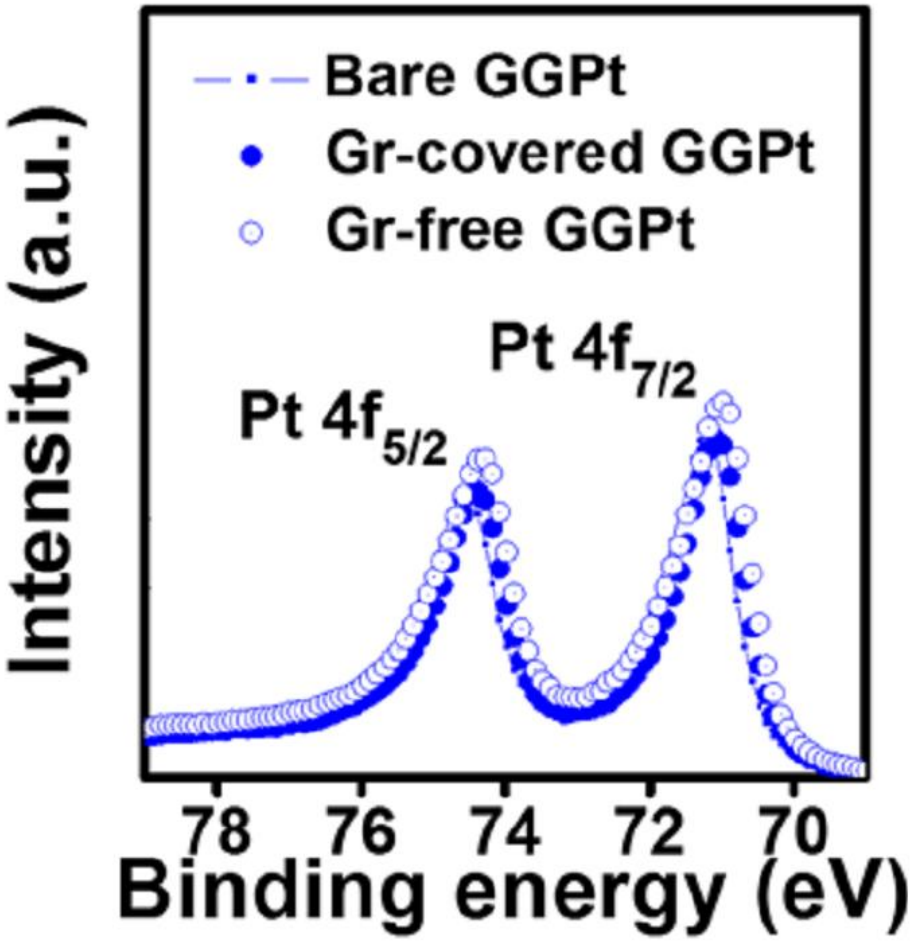

Figure 3-7. High resolution Pt-$4f_{5/2}$ and Pt-$4f_{7/2}$ XPS spectrums of as-received GGPt film, graphene-grown GGPt film, and GGPt film without graphene layer after the thermal-assisted transfer process.

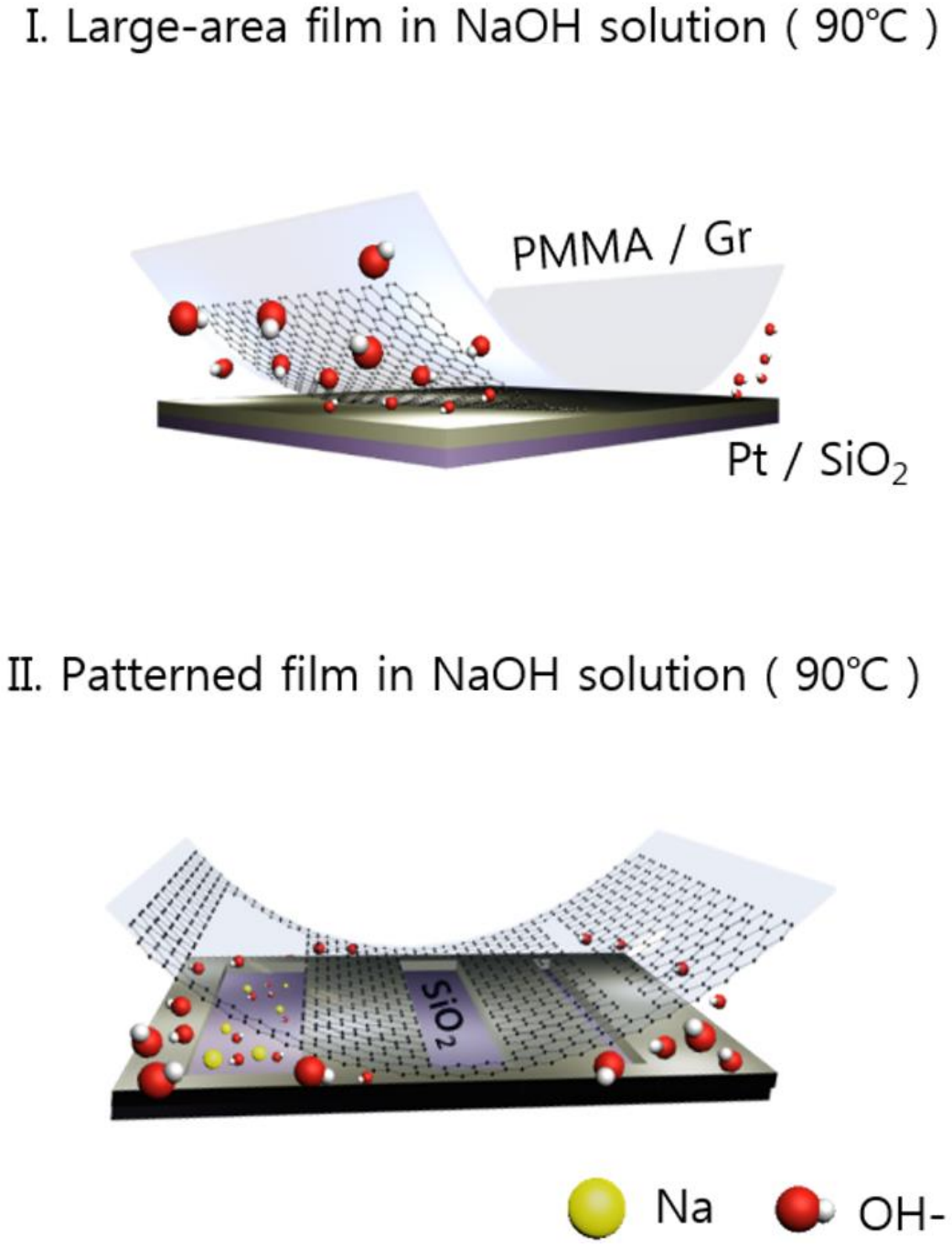

Figure 3-8. Illustrations for mechanism of hydroxide ionic bubbling transfer assisted by thermal energy from large-area Pt and patterned Pt films.

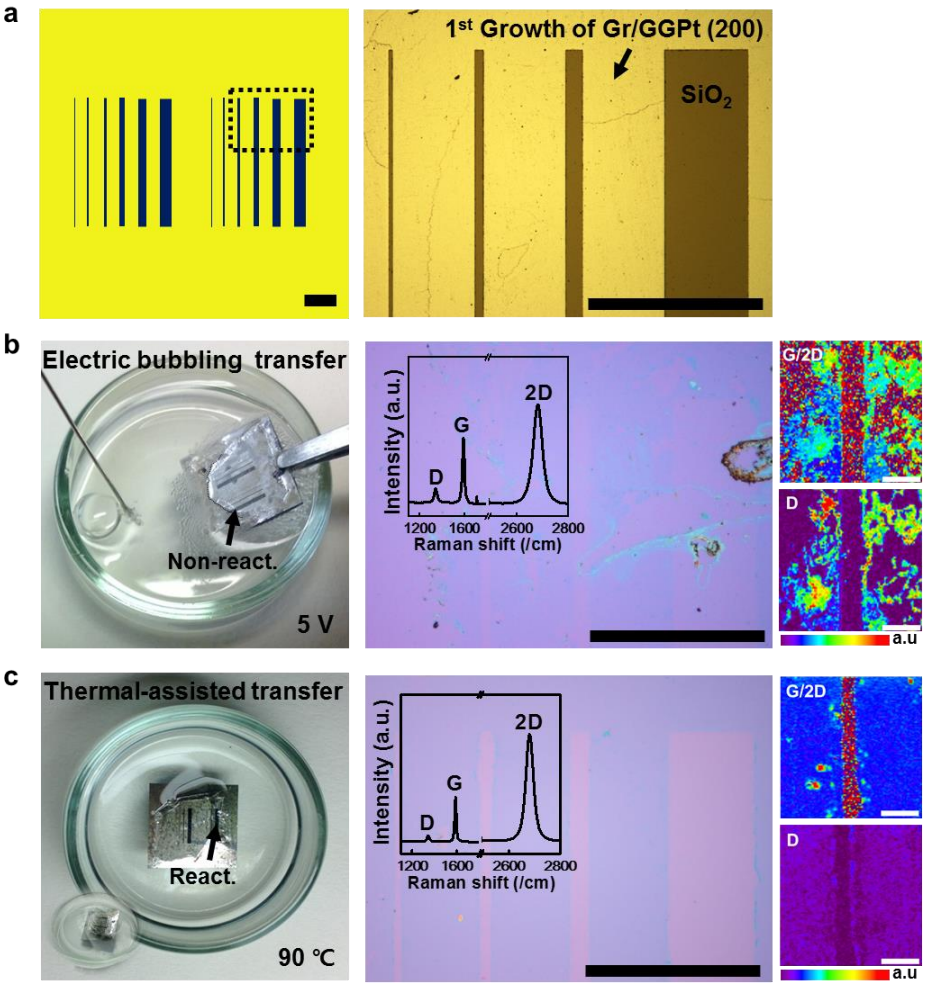

Figure 3-9. Comparison of graphene transfer for patterned platinum film. (a) (Left) Illustration of patterned graphene films (400 nm-thick-Pt/300 nm-thick-SiO_2 on Si substrate). (Right) OM image of the patterned Pt film with grown graphene. (**b** and **c**) Comparison of graphene transfer from box in inset of (b) illustration using an electrochemical transfer method and the thermal assisted transfer method. (Left) The PMMA/graphene is gradually separated from the patterned Pt film driven by the H_2 bubbles produced at the cathode after applying a constant voltage (5 V, 25 ℃), and a Pt rod is used as an anode. The H_2 bubbles were not produced at insulating SiO_2 surface. (Right) OM image of the incompletely separated graphene on SiO_2 substrate after removal of PMMA supporting layer. (c) (Left) The PMMA/graphene/Pt stack semi-floated on NaOH solution (1M) at 90 ℃, and the PMMA/graphene was gradually separated by Na and OH^- ions from the both surface of Pt and SiO_2, respectively. (Right) OM image of the completely transferred graphene on SiO_2/Si substrate after removal of PMMA supporting layer.

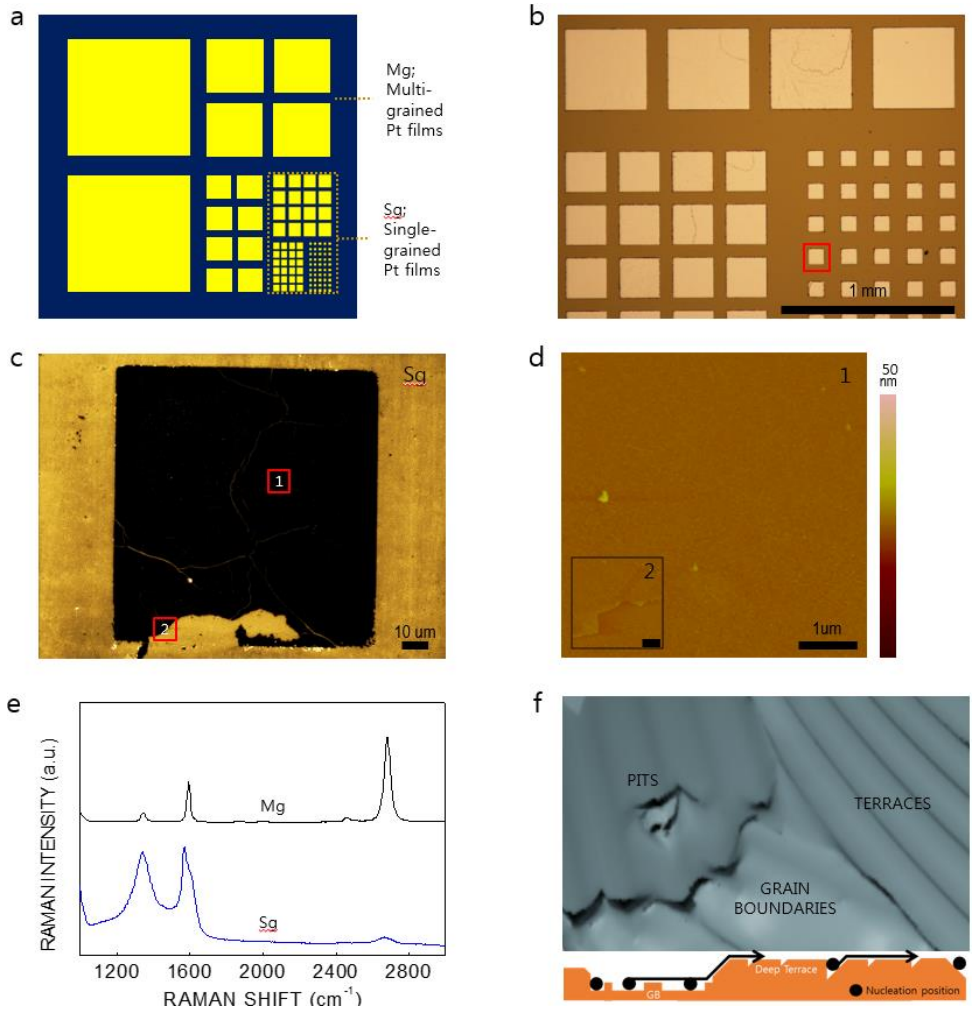

Figure 3-10. (a) An illustration of patterned graphene films on 400 nm-Pt/SiO_2/Si substrate. (b) Electron backscattering diffraction (EBSD) image of the patterned Pt (200) film. (c) Scanning electron microscope (SEM) image of transferred graphene using CVD process in H_2 gas (50 sccm) and CH_4 gas (5 sccm) at 975 ℃ for 10 min corresponding to 100 μm sized pattern. (d) AFM images for monolayer graphene (scale bar 1 μm) corresponding to red boxes of image c. (e) Representative Raman spectrums of transferred graphene from multi-grained patterns (5 mm^2 ~ 1 mm^2), and single-grained patterns (2.5 mm^2 ~ 10^4 μm^2). The graphene formed on single-giant grain Pt has polycrystalline structure. (f) A Sketch allows presumption of morphology of grain boundaries and terraces as preferred orientations for graphene nucleation site.

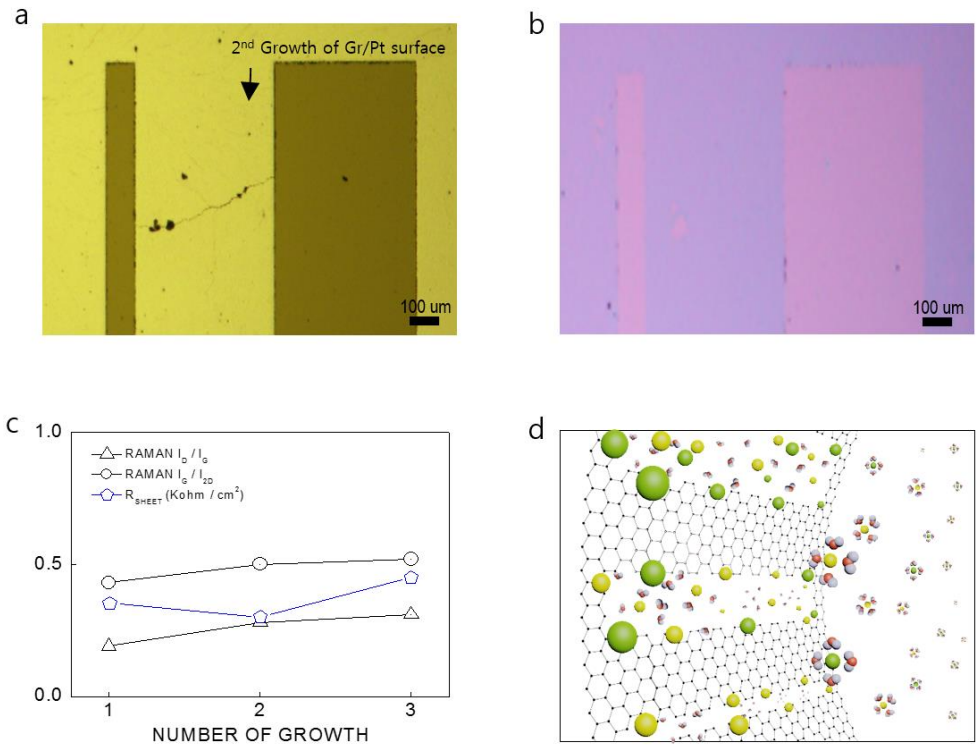

Figure 3-11. (a) Optical microscopy (OM) image of patterned $Pt/SiO_2/Si$ substrate with second growth of graphene using CVD process in H_2 gas (50 sccm) and CH_4 gas (5 sccm) at 975 ℃ for 10 min. (b) OM image of the incompletely separated graphene on SiO_2 substrate after removal of PMMA supporting layer. (c) Graph of the comparisons of ratio of Raman intensities and sheet resistances on number of growth with recycled Pt film. (d) An illustration of patterned hydrophobic membrane for water desalination facilities.

A head of research institution	Representative subject and results
Nagoya Univ.	- Super-hydrophobic Silicon using Microwave Plasma CVD - The application for super-hydrophobic glass or plastics as low formation T
SKKU / SAIT	- Wafer-scale synthesis and transfer of graphene / Ni films using CVD process - Graphene films with sheet resistance of 280 Ω/sq (80% transparent)
U. Texas Austin	- Graphene channel was measured to be higher than 4000 cm^2/V in field-effect transistor using large-scale cu foil
MIT, Cambridge	- An investigation into the role of chemical functional groups bonded to the edges of graphene pores suggests that commonly occurring hydroxyl groups can roughly double the water flux thanks to their hydrophilic character.
RIST / KORES / KIGAM	- largest RO seawater desalination plants using lithium carbonate

Table 3-1. Research status related MD process.

Category	Requirement
1. Surface	A super-hydrophobic
2. Morphology	Many porous
3. Process	No capillary condensation should take place inside the pores of the membrane
4. Affects	Not alter the vapor-liquid equilibrium of the different components in the process
5. Atmosphere	Partial pressure gradient in the vapor phase for membrane operation

Table 3-2. Essential factors of membrane for MD process.

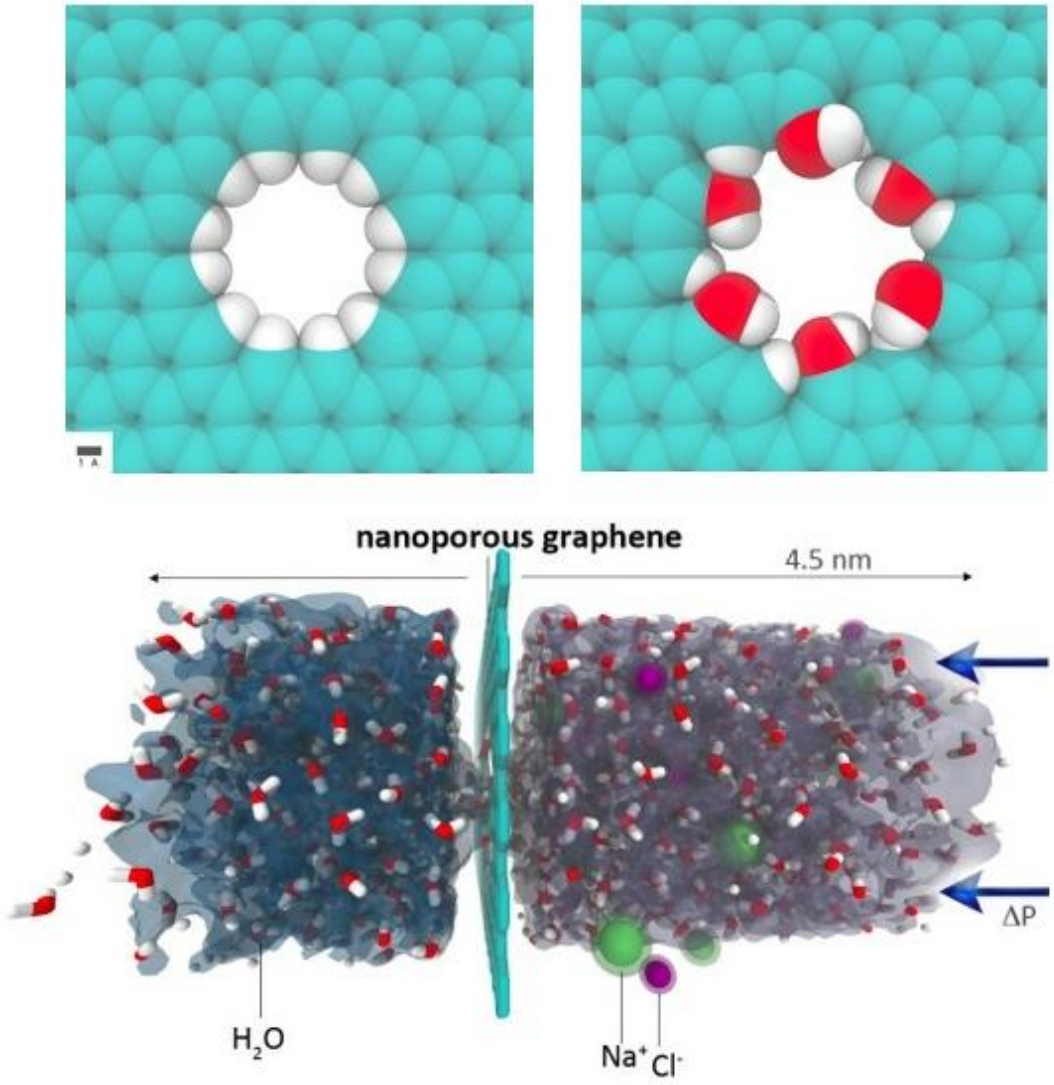

Figure 3-12. An example of graphene based membrane for water desalination.[51]

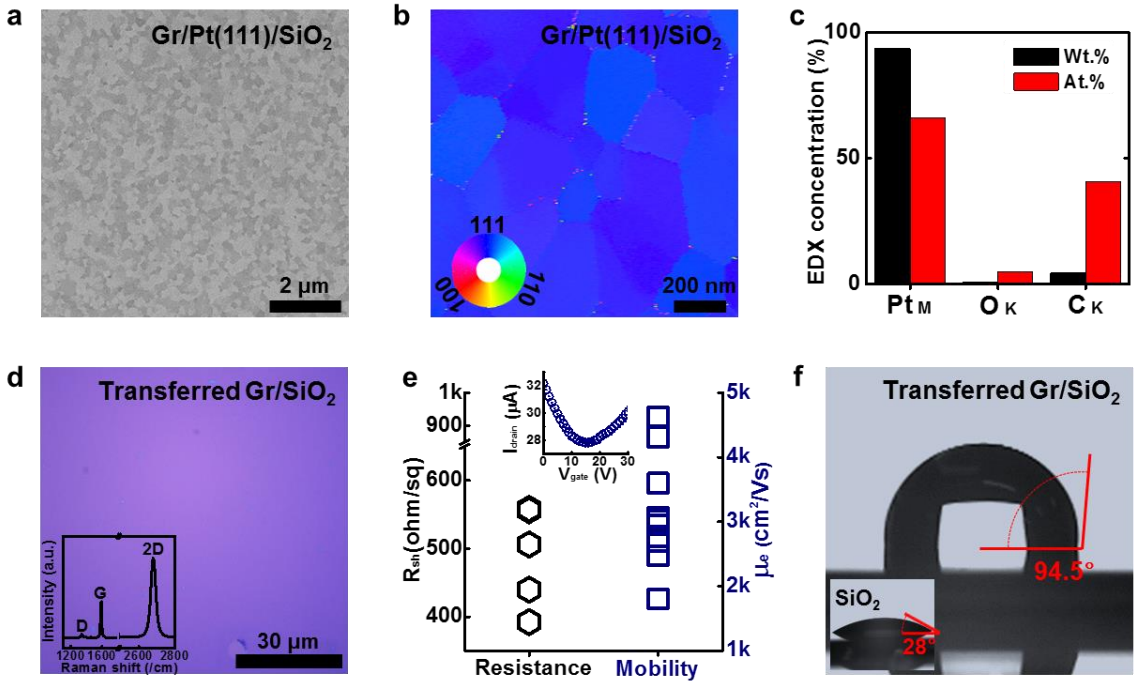

Figure 3-13. CVD Graphene grown for 10 min, without pre-annealing step. (a-b) A typical graphene grown on 80 nm-thick-Pt(111)/SiO_2/Si. (c) Purity of graphene/Pt(111) after CVD process. (d-e) Raman and electrical characteristics of high-quality transferred graphene/SiO_2/Si. (f) Hydrophobic property of a graphene layer.

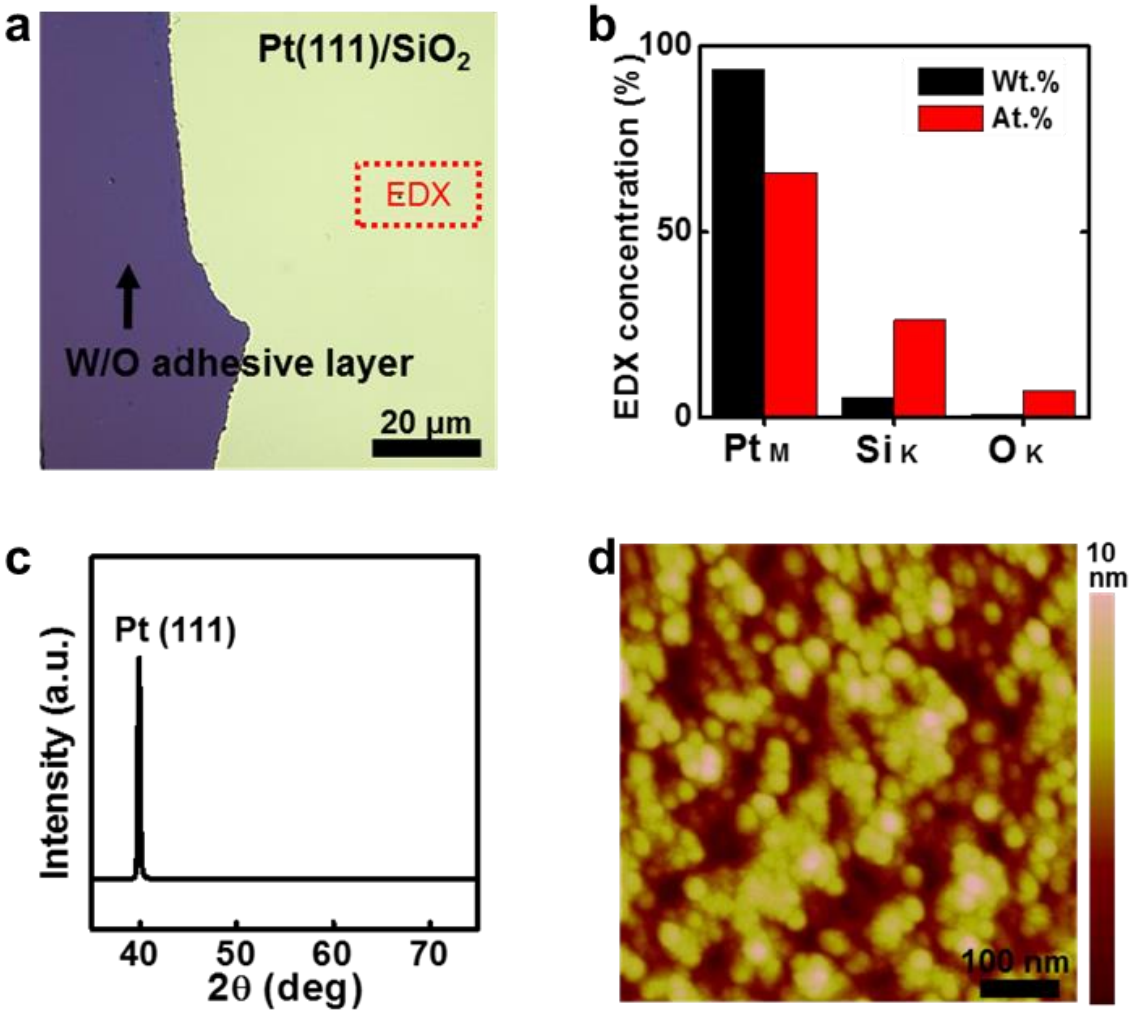

Figure 3-14. During Pt film sputtering, the inserted oxygen for adhesion between Pt and SiO_2. As the results of Pt(111), they show the typical characteristics by using (a) OM, (b) EDX, (c) XRD, and (d) AFM. Since noble metals have low solubility in oxygen, entrapped oxygen gas work as adhesion layer by forming platinum oxide.

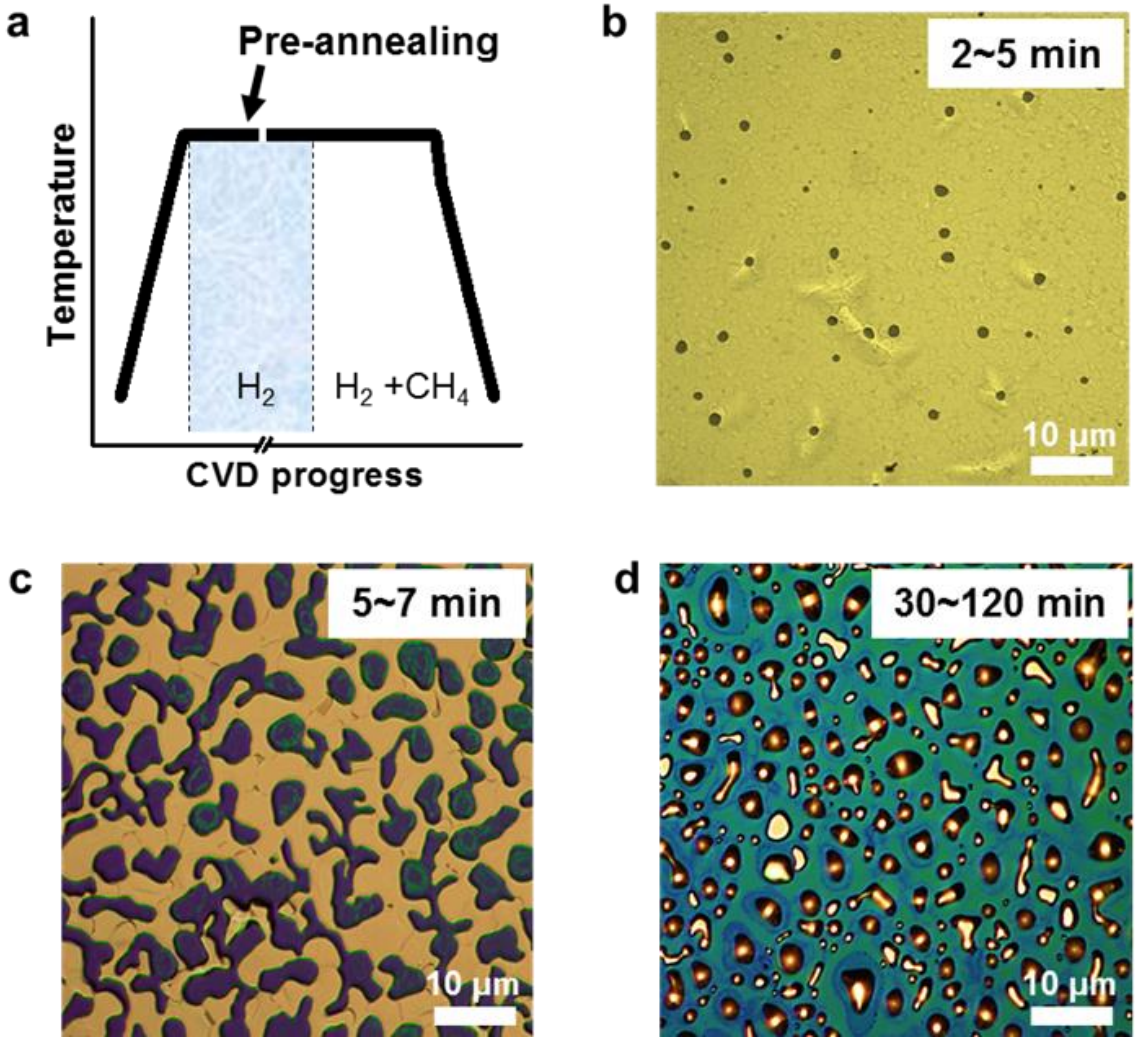

Figure 3-15. A pre-annealing time dependent porous Pt(111) film. The pre-annealing step at 975 ℃ in H_2 atmosphere during 2 min ~ 2 hours.

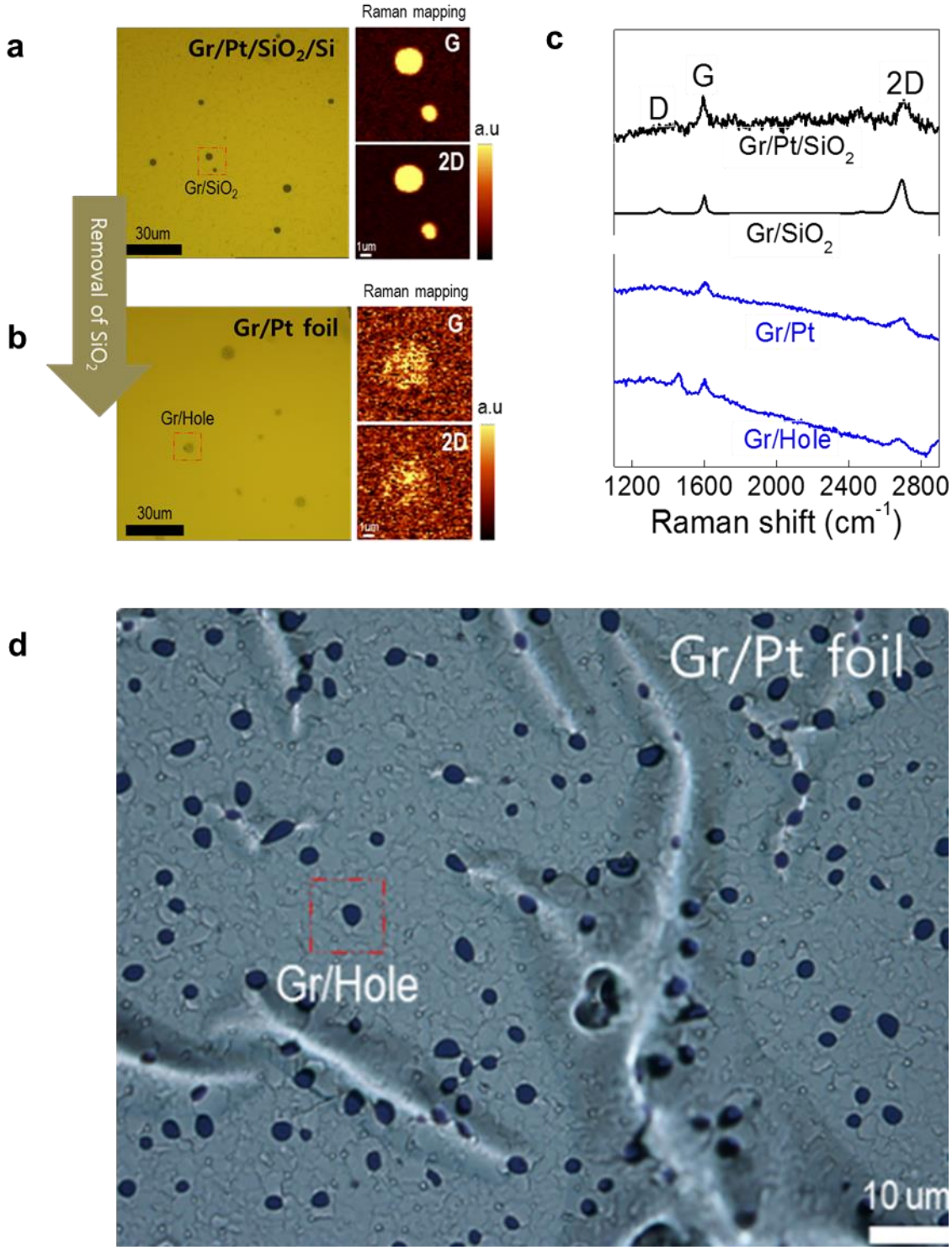

Figure 3-16. Pre-annealing step was performed for 4 min, subsequently graphene was grown for 10 min. (a) OM, Raman map images of graphene grown on Pt(111)/SiO_2/Si with a few μm pores. (b) To confirm continuously grown graphene, the graphene/Pt films separated from SiO_2 by chemical etching. (c) Raman spectrums of the graphene on Pt film.

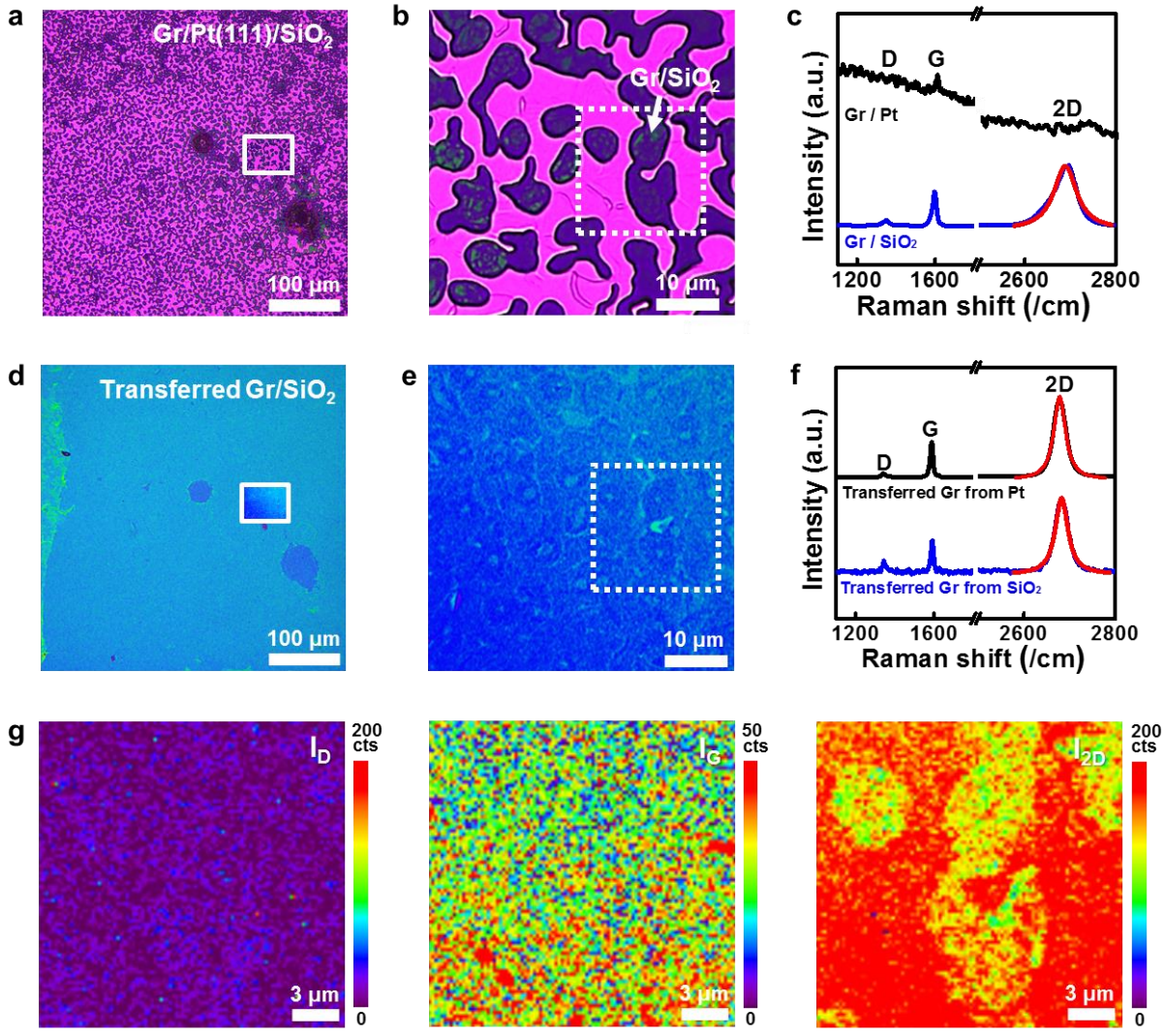

Figure 3-17. Pre-annealing step was performed for 6 min, subsequently graphene was grown for 10 min. (a-c) OM images of graphene grown on Pt(111)/SiO_2/Si in H_2 gas (50 sccm) at 975 ℃ for 6 min and adding CH4 gas (5 sccm) for 10 min, resulting in direct formation of graphene onto the SiO_2 surface. (b-f) Transferred graphene onto SiO_2/Si substrate from Pt corresponding to (a-b) using thermal-assisted transfer method. (g) Corresponding Raman map images obtained from the regions highlighted by the dotted rectangles in (e).

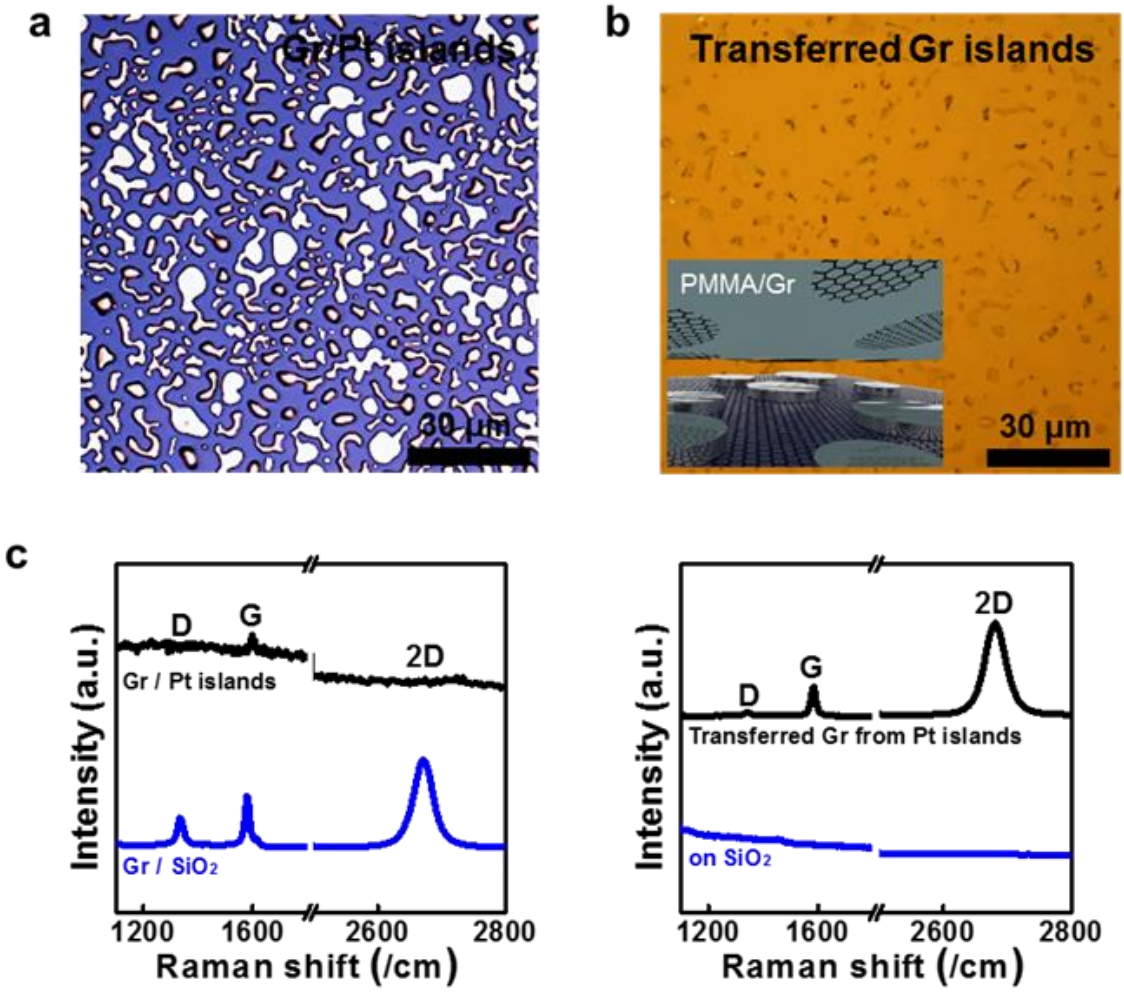

Figure 3-18. Pre-annealing step was performed for 30 min, subsequently graphene was grown for 10 min. (a) OM image of graphene grown on Pt islands in pre-annealed for 30 min, resulting in direct formation of graphene onto the SiO_2 surface. (b) Successful transferred graphene onto SiO_2 via thermal-assisted transfer method, and corresponding Raman spectrums.

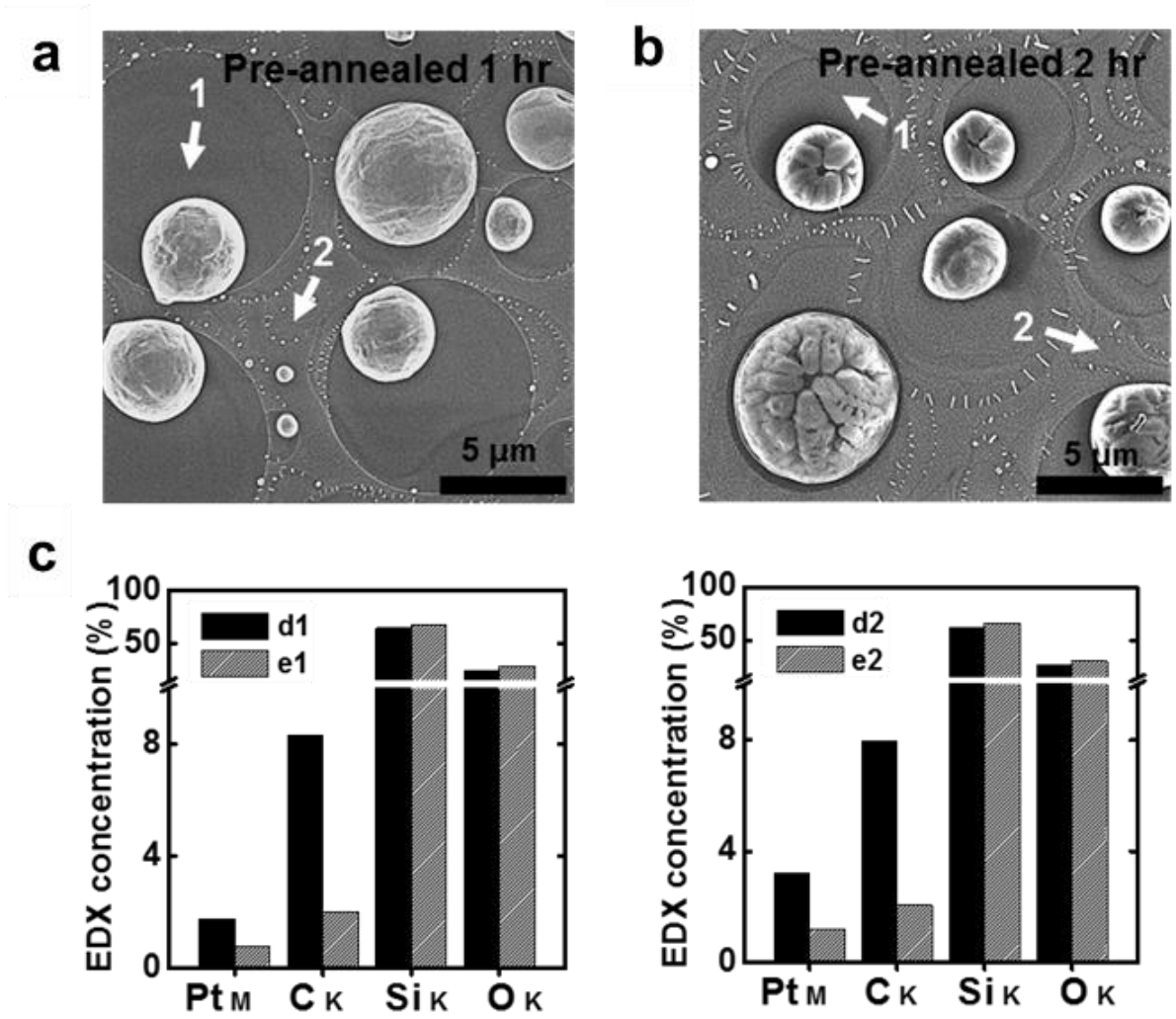

Figure 3-19. Pre-annealing step was performed for 1 ~ 2 hours, subsequently graphene was grown for 10 min. (a,b) SEM images of pre-annealed (for 1hr, 2hr) graphene on agglomerated Pt islands. (c) Corresponding EDX analysis from numbering sites in (a-b) images.

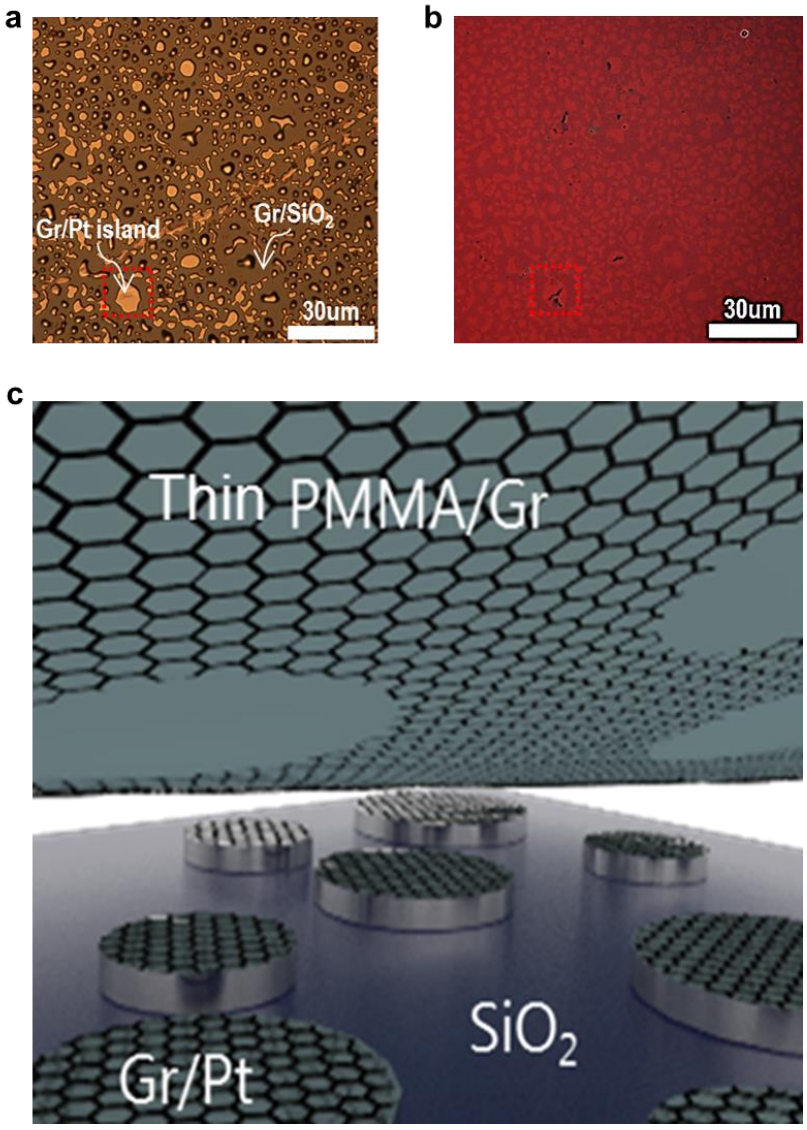

Figure 3-20. Pre-annealing step was performed for 30 minutes, subsequently graphene was grown for 10 min. OM image of graphene grown on Pt(111)/SiO_2/Si in H_2 gas (50 sccm) at 975 ℃ for 30 min and adding CH_4 gas (5 sccm) for 10 min, resulting in direct formation of graphene onto the SiO_2 surface. (b) Successful transferred graphene/SiO_2 via thermal-assisted transfer method after coating of the thin PMMA (< 5 wt%). (c) During transfer with thin supporting layer which allows transfer from only SiO_2 substrate.

3.4 Conclusions

In this chapter, large-scale and patterned graphene films can be successfully transferred onto arbitrary substrates via thermal-assisted transfer method and the Pt substrates can be repeatedly used for the proliferation of graphene applications. From that the Pt is an inoxidizable metal with a high melting point, which will markedly decrease the defects such as impurities in the resulting hydrophobic surface of graphene membrane. For this, I achieved porous graphene membrane using controlled Pt(111) film to get near the commercialization.

Chapter 4. Applications and Summary

4.1 Introduction

Graphene is an extremely interesting and potentially important material with unique and desirable physical characteristics. A few of the practical applications envisioned for graphene include graphene based electric-device like a optoelectronic coating layer, graphene based bio-device like a scaffold, and so on.

4.1.1 A brief overview of the graphene based LED epitaxial structures

III-nitride semiconductors (III-Ns) have attracted considerable attention as a field of solid state optical devices such as LED (light emitting diode), LD (LASER diode), photo-detector, and FET (field effect transistor), because the III-Ns have a direct band gap ranging from 0.7 eV (InN) to 6.2 eV (AlN) which covers the entire visible spectrum, ultraviolet (UV) and infrared (IR). Particularly, the GaN based LEDs with shorter wavelength emission than 540 nm have been studied for over a decade owing to UV-blue light or efficient white light source.[58-62] Unfortunately, there were no GaN substrates available for high crystallinity of LED epi-structure and its commercial usage. Thus, the GaN based LED epi-structures were typically grown on C-plane sapphire (0001) substrate with GaN buffer layer. However, the growth of GaN/C-sapphire is much more complicated because it involves a relatively large lattice mismatch (~16 %) result in wurtzite/corundum hetero-structures[63]. Besides, a polarized charges are induced by crystal polarity in N- or Ga- face GaN/C-sapphire hetero-structures[64-65]. As the polarized charges are fixed in InGaN/GaN multi quantum well structures (MQWs) of GaN based LED epi-structures, a built-in electric field is generated by them. Then, an effective recombination is decreased by a spatially separation between electrons and holes. Because the fixed charge in electric field does not contribute as mobile carriers in principle[66-68]. According to recent report, considering that the built-in electric field induces energy band slope, which is a case where the energy band structure of the GaN based MQWs can definitely be regulated by increasing injection currents[66]. With increasing injection currents, however, the energy band shows blue-shift emission spectrum toward shorter wavelengths[69]. The energy band is also related with a compressive strain or tensile strain of epi-structures that originated from a crystallographic orientation. Consequently, the GaN based LED epi-structures have the strain that induced static electric fields originated from heterojunctions with polarized behavior[70-71]. To minimize the strain in LED epi-structures, many research groups have tried to make growth of either epitaxial lateral overgrowth (ELO) or non-/semi-polar GaN for avoidance of the polarized behavior[72-77]. For examples, Kim J. et al. have demonstrated the relaxed-strain through the ELO obtained by using silica hollow nano-spheres[70], while Ingrid L. Koslow et al. and Kim et al. used semi-polar (11-22)[71-73]. In

addition, Vin-Cent Su et al. and Yao-Hong You et al. have shown both the ELO based LED epi-structures and enhanced internal quantum efficiency (IQE) through pattern sapphire substrates (PSS)[76-77]. Recently reports have also demonstrated both the strain relaxation and the weak polarization through amorphous substrate with a non-polar behavior[78-85]. Interestingly, they commonly used a graphene intermediate layer for epitaxial growth of GaN on amorphous substrates. Due to unique properties of the graphene such as honeycomb lattice and high thermal/mechanical stability[85-89], which signified that they were reduced the lattice/thermal mismatch between GaN and substrate interface[78-82]. However, the as-synthesized graphene cannot contribute to form GaN nucleation because it has an atomically smooth surface and relatively free of dangling bonds. Thus, the modified graphene has been used by an ionic doping, UV treatment, oxygen plasma etching or ZnO-nanowall (NW) coating for GaN nucleation[81-82]. In spite of these efforts, the techniques could not be close to commercial approach because an additional process of very thick GaN buffer layer is required to make high crystallinity of GaN based LED epi-structures.

4.1.2 A brief overview of the graphene based bio-scaffolds

Current tissue engineering approaches and cell therapeutic applications combine different scaffold materials with good biocompatibility and tissue-specific inductive capabilities. The artificial scaffolds could be used for different desired cell types in mechanically, functionally similar or better tissue engineering.[90-93] Recently, there has been active research into scaffold materials such as poly-vinyl alcohol (PVA), chitosan, and low-dimensional carbon structures (carbon nanotube, graphene, graphene oxide).[94-99] But the polymeric PVA scaffold suffers from humidity instability in the air, and the chitosan scaffold has a restricted application without structural modifications.[98-101] For these reasons, they have limited the widespread use of stem cell research. In the case of the low-dimensional carbon structures for biocompatible and implantable platform, they also have problems such as high process costs, high temperature processing, the use of flammable gases (CH_4), and additional transfer methods. In particular, it is difficult to attach functional groups which result in a hydrophobic surface for cell adhesion. For this, the structurally modified graphene oxide (GO) is an issue there, but it involves a toxic chemical process.[102]

4.2 Applications

In this section, the graphene layer was applied for the optoelectronic coating layer on LED epitaxial structure and stem-cell cultured bio-scaffolds. For these applications, the graphene layers were applied by DAS and CVD method. The detail experimental synthesis of graphene as follows;

(1) DAS-Graphene preparation

Polycrystalline Ni (thickness: 50 nm) is deposited by using electron-beam evaporation (E-beam evap.) at room temperatures on sapphire (for LED epitaxy) and silica-glass (for scaffold) substrates. The sapphire (2 inch) and transparent glass (1 inch) substrates were used as-received. Next the Ni film on sapphire or glass stack was placed onto a molybdenum holder and the stack was covered with graphite powder (Aldrich, product number 496596), then the graphite powder was pressed onto the top of stack. And the graphene grown by Diffusion-assisted synthesis (DAS) method at 360 ℃ for 90 min (Argon atmosphere).[89]

(2) Conventional CVD graphene preparation

The synthesis of CVD-graphene used transition metals Pt (111, 220) film substrates. Before the transferring process to transparent substrate, monolayer graphene was synthesized by using Pt film (80nm-thickness, The G-Mek corp.) on the SiO_2/Si. After the Pt (111 or 220) substrate was loaded into a CVD chamber, the sample was elevated to the process temperature of 975 ℃ and maintained for 10 min under CH_4/H_2 gas mixture (5 and 50 sccm, respectively). Next, the chamber was cooled down to room temperature with natural cooling rates. The layer of PMMA is coated onto the graphene to act as a support. Then, acetone are used to remove the PMMA.

4.2.1 Transparent conducting layer on graphene-based LED epitaxial structures

In this section, I have synthesized the strain relaxed InGaN/GaN MQWs on GaN/graphene/sapphire (GGS) hetero-system as based on our previous results via metal-organic chemical vapor deposition (MOCVD). For this, I employed the previous of the one-step growth of GaN thin film, and it had been achieved by DAS (diffusion-assisted synthesis)-graphene coating layer without low temperature-GaN (LT-GaN) buffer layer.[82,89] In addition, our current study provides a selective area growth (SAG) through DAS-graphene patterns on C-sapphire substrate, while many reports are trying to the use of non-photolithographic patterning fabrication because previous patterning techniques have been shown residues and complicated, expensive process for high quality of III-N LED epi-structures (figure 4-

1).[103-107] Here, the structural properties of GGS based LED epi-structures were analyzed by atomic force microscopy (AFM) and transmission electron microscopy (TEM) (table 4-1 and figure 4-2). It should be noted that the DAS-graphene coating layer contributed to the strain relaxation of epi-structures, and it was demonstrated by reciprocal lattice mapping measurement of high-resolution x-ray diffraction (HR-XRD). I propose that the strain relaxation originated from laterally overgrown GGS heterostructures.[108-109] The GGS template also contributed to a favorable result such as built-in electric fields free in near InGaN/GaN MQWs, it was shown to result of power-dependent photoluminescence (PL) with un-shifted emission peaks. In addition, I found a phenomenon of phase-separation in InGaN/GaN active layers through analysis of cathode-luminescence (CL) emission mapping, which originated from a rough surface of GGS template (figure 4-3). On the basis of these results, the GGS based InGaN/GaN MQWs have higher optoelectronic performances such an internal quantum efficiency of ~0.55, compared to the MQWs grown on a conventional GaN buffer template. Besides, we suggest a new stack design, which is graphene double-sided III-N LED epi-structures for transparent metal-free electrodes (figure 4-4). The graphene has possibilities as a transparent and current spreading electrode for many different types of III-V based LEDs, while conventional previous rigid metallic electrodes such an indium tin oxide (ITO) with deficiency of natural indium resources is weak in acidic solution and low level transmittance value in UV range.[110-111] Here, the introduced graphene top layer allows more transparent in near UV range and enhanced I-V curves than ITO layer and Au/Cr metal anodes, respectively (figure 4-4). Especially, we believe that the transferred graphene top layer is attributed to a full contact on even rough surface of P-GaN epi-layer. In conclusion, I studied that the enhanced opto-electrical performances of patterned InGaN/GaN MQWs by using double-sided graphene layers (GGS). The GGS based InGaN/GaN MQWs show enhancement of indium phase separation with a rougher GaN surface than conventional LT-GaN based MQWs. In addition to, the GGS-based three-period InGaN/GaN MQWs displayed enhancing of IQE and negligible shifts of emission wavelength along the high current density variation, resulting in built-in electric field free in near MQWs.

Furthermore, the transferred graphene on top of the LED epi-structure showed relatively high optical transmittance over 80 % at UV region, thus the LED showed decreased forward voltage of 2~3 V. Also, the graphene layer covered even naturally textured V-shaped pits of P-type GaN epilayer. The introduction of graphene double-sided MQW structures may provide a new stacking solution for III-Nitride based light emitting diode (LED) applications. The most important thing at this study is the collaborative research with Goh-Myeong Bae.[112]

4.2.2 Graphene based bio-scaffold for stem-cell experiments

Herein, large-area graphene films were grown directly on desired substrates such as glass, quartz, indium tin oxide and flexible polymer by the DAS process at low temperatures (≤ 360 ℃), as shown in figure 4-5.[89] First, polycrystalline Ni films were deposited by using an electron-beam evaporator at room temperature on a transparent glass substrate. The average grain size of Ni on substrate was about 50 nm. To obtain the structure with high-density graphene ridges, the as-deposited Ni films need no further thermal treatments. This resulted in the atomic impurities of oxygen and hydrogen remaining on the Ni films.[89] Next, the graphite powder was strewed on the Ni film as a solid C source. The C-Ni/substrate diffusion couple, which was pressed at ~1 MPa, was then annealed under a flow of argon gas at atmospheric pressure after being heated up to 360 ˚C for 90 min. Following this procedure the solid C source was removed, the samples were cleaned by sonication for a few seconds, and the Ni films were etched from the substrate. The resulting Ni films have the polycrystalline grain boundaries (GB), thus indicating the formation of ridges from the C-atoms diffused into the GB.[89] I demonstrate the applicability of our approach to prepare graphene on silica-glass, indium-tin-oxide (ITO) glass and quartz plate. As shown AFM image of DAS-graphene in figure 4-6, 4 nm-thick polycrystalline graphene layers were grown on glass. The spacing between neighboring graphene ridges was 2 μm. The thickness of the graphene ridges was measured by AFM profile, and it was 3 nm from bottom of the graphene (~4 nm). This ratio of ridge and bottom is very similar to the quartz plate, which means it has become a 3-dimensional structure for better tissue engineering. But, it is hard to distinguish the morphology of the graphene on ITO glass because the 150-nm-thick ITO films are rough. In contrast to the flat morphology of conventional graphene, our graphene showed a polycrystalline graphene and 3-dimensional structure, and the crystallinity of DAS-graphene was analyzed by the Raman spectroscopy (figure 4-6). They show three primary features: a D band at ~1350 cm^{-1}, a G band at ~1590 cm^{-1} and a 2D band at ~2680 cm^{-1}, all expected peak positions for graphene. The poor results of 2D band indicate that graphene growth was doped by O, H impurities[113], polycrystalline structures[114-115], and unwanted scattering to the background of substrates. For the graphene layers grown on all substrates at 360 ℃ during 90 min, the visible transmittance decreased by only about 2 % (at 550 nm) compared to the transmittance of the substrate without a graphene coating layer. It can be allowed to enhance visibility for fluorescence bio-imaging. Regardless of the type of substrate, the multilayer graphene ridges of regions covered with continuous graphene were formed by GB. In the light of these results, our graphene morphologies heavily upon morphologies of Ni films. Therefore, our graphene offers multiple advantages for bio-scaffolds based on cell shapes. In particular, the multilayer graphene ridge can rein the growth, adhesion and eventual fate of stem cells. This is because the resulting of DAS-graphene was included O and H impurities from the Ni film, and indicating that they had a hydrophilic surface.[116-119] They are mainly functionalized at multilayer ridges due to high edge roughness, it is an appropriate

region for chemical modification compared to conventional graphene or graphene oxide (GO).[120-121] In this regard, our graphene presents rough regions compared to CVD-graphene. The root mean square roughness (Rq) of DAS-graphene surfaces was studied by using AFM images. With the exception of the rough ITO glass, the roughness of DAS-graphene has increased approximately 4-fold from the bare substrates as shown in figure 4-6. However, the Rq of CVD-graphene/glass has only increased 0.25 nm from the bare glass. This evidence shows the existence of 3-dimensional architectures such as CNT, fluorine, and multilayer GO for functional sites such as carboxyl (R-), epoxy (C-O) and hydroxyl (O-H) groups on the 3D edge site of carbon based scaffolds.[122-125] Then, the presence of functional groups in DAS-graphene was confirmed by Fourier transform infrared spectroscopy (FTIR) compared to CVD-graphene (figure 4-7). In contrast to the CVD-graphene, the DAS-graphene shows molecular vibrations by the R- (COO-), C-O and O-H groups. The peak of DAS-graphene at 1500 - 2500 cm^{-1} is related to the vibrations of C-C or C-O groups, and the peak at 2500 - 3800 cm^{-1} is related to the hydroxyl groups. In particular, the broad H-O-H stretching band between 3000 and 3750 cm^{-1} is highly visible here, and which is related to concentration of water (H_2O).[126-129] But the peak of C-H bonding (3170 cm^{-1}) is rarely seen in both DAS- and CVD-graphene. The CVD-graphene only shows the peak of C-C groups, which is based on a good crystalline carbon structure. Notable is that the peak of C-H bonding is not shown here, too. It is because no hydrocarbon sources were used during the DAS process, and the protecting polymer layer was not used for transfer. Eventually, the rough surface and functionalized structure are affecting the wettability. For this, the contact angles of our graphene films were compared to the conventional CVD-graphene with hydrophobic surface (> 60°). But it is known that the hydrophobic scaffold exhibits poor adhesion for aqueous bio sample such as protein.[130] On the contrary the DAS-graphene without surface treatments had a naturally-formed hydrophilic property, regardless of any given substrates (figure 4-8). It basically means that the DAS-graphene has improved wetting properties compared to CVD-graphene, as shown by previous research that showed the wetting behaviors of DAS-graphene to be hetero-junctions.[113] Since their wetting behavior is determined by the intermolecular interactions between wetting atoms and the substrate they rest on[131-133], it is expected that the DAS-graphene would be ideally used for the hydrophilic–lipophilic scaffolds and approach an eco-friendly process.[134,135] In conclusion, I studied that the DAS-graphene layers exhibited tunable structural properties depending on the substrates, which will influence on the proliferation, an undifferentiated state, and self-renewal ability of the stem cells. We found that our polycrystalline graphene scaffolds provided a favorable environment for stem cell culture since they showed a hydrophilic property, in contrast to the conventional graphene with a hydrophobic nature. The ability of DAS-graphene based scaffolds may open up new possibilities for stem cell research such as the response to wettability and electrical stimulation.[136-137]

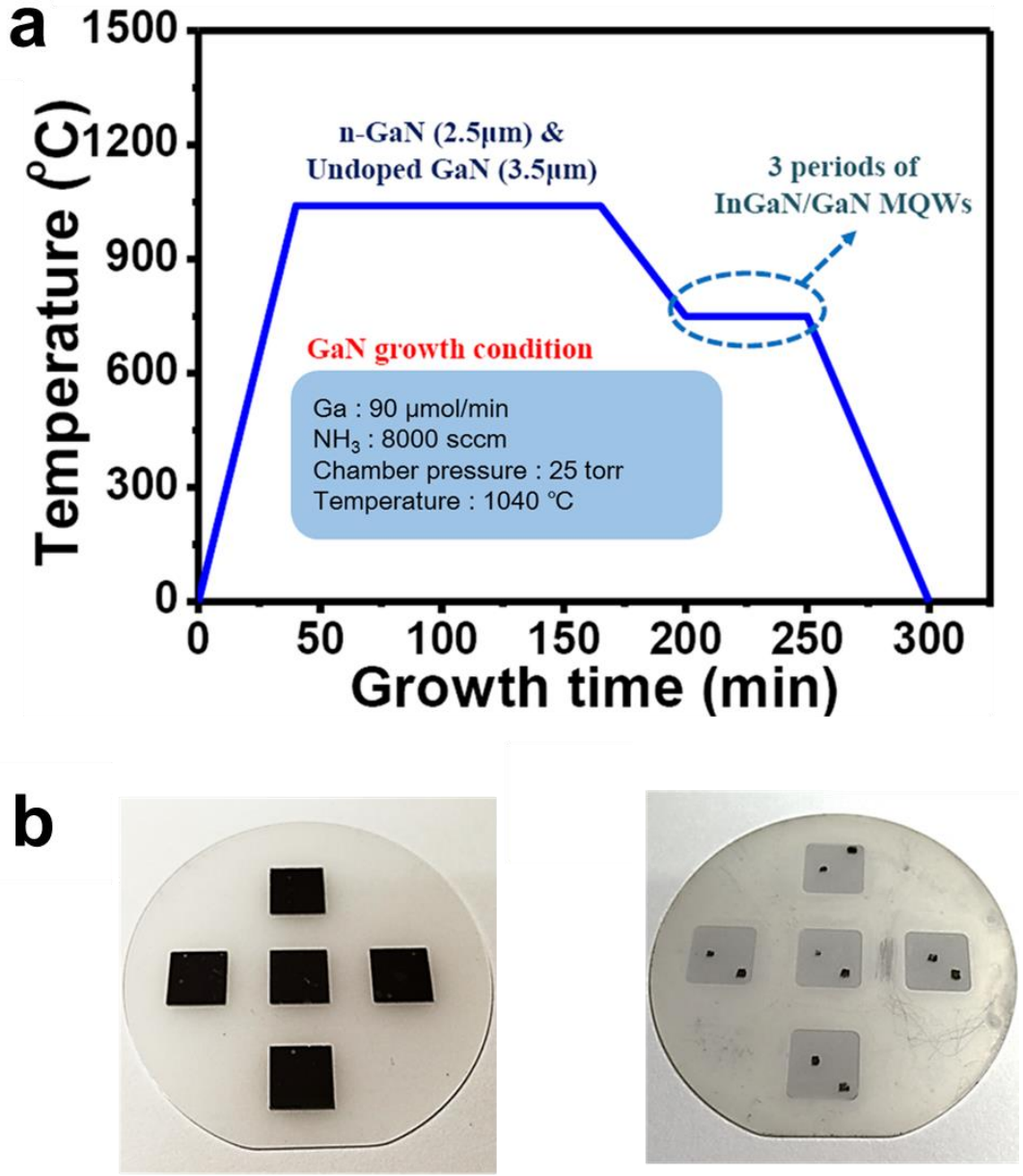

Figure 4-1. Schematic pictures of selectively patterned MQWs structure using graphene-based one-step GaN growth. (a) Experimental scheme of MOCVD growth recipe. (b) Photo of Ni-coated patterned sapphire substrate and III-N LED Epi-structures with Au/Cr electrodes.

RMS Roughness (nm)	Conventional GaN on LT-GaN/sapphire	GaN on GGS
Undoped GaN	0.397	1.56
p-GaN/MQW /n-GaN	0.445	1.78

Table 4-1. Surface roughness of the two types of MQWs measured by an AFM images of DAS-graphene coated c-plane sapphire substrate, one-step growth GaN template and MQWs structures.

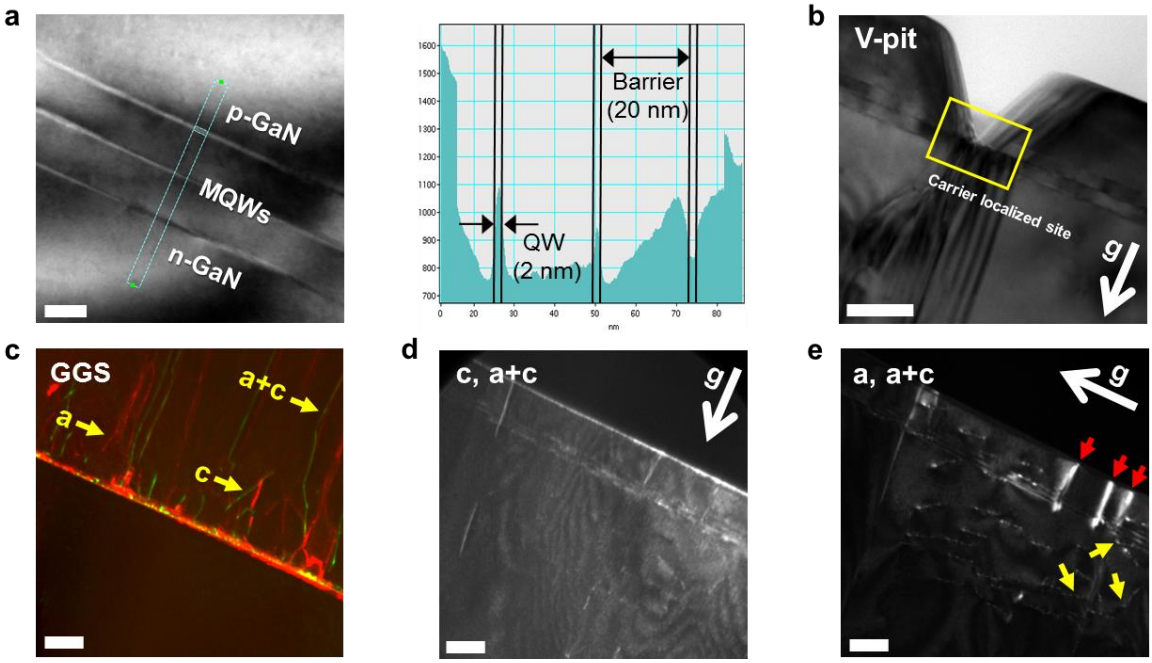

Figure 4-2. (a) Representative cross-sectional transmission electron microscopy images of the DAS-graphene based multiple quantum well structures and corresponding line profiles. (scale bar 20 nm) (b) The graphene based TDs induce large V-defect along the [0001] direction. (scale bar 1 μm) Threading dislocation of (c) GGS interface and (d-e) near MQW regions, bright field image taken under (d) g = (0002) and (e) g = (-2110) direction with Burgers vectors. (scale bars 0.2 μm)

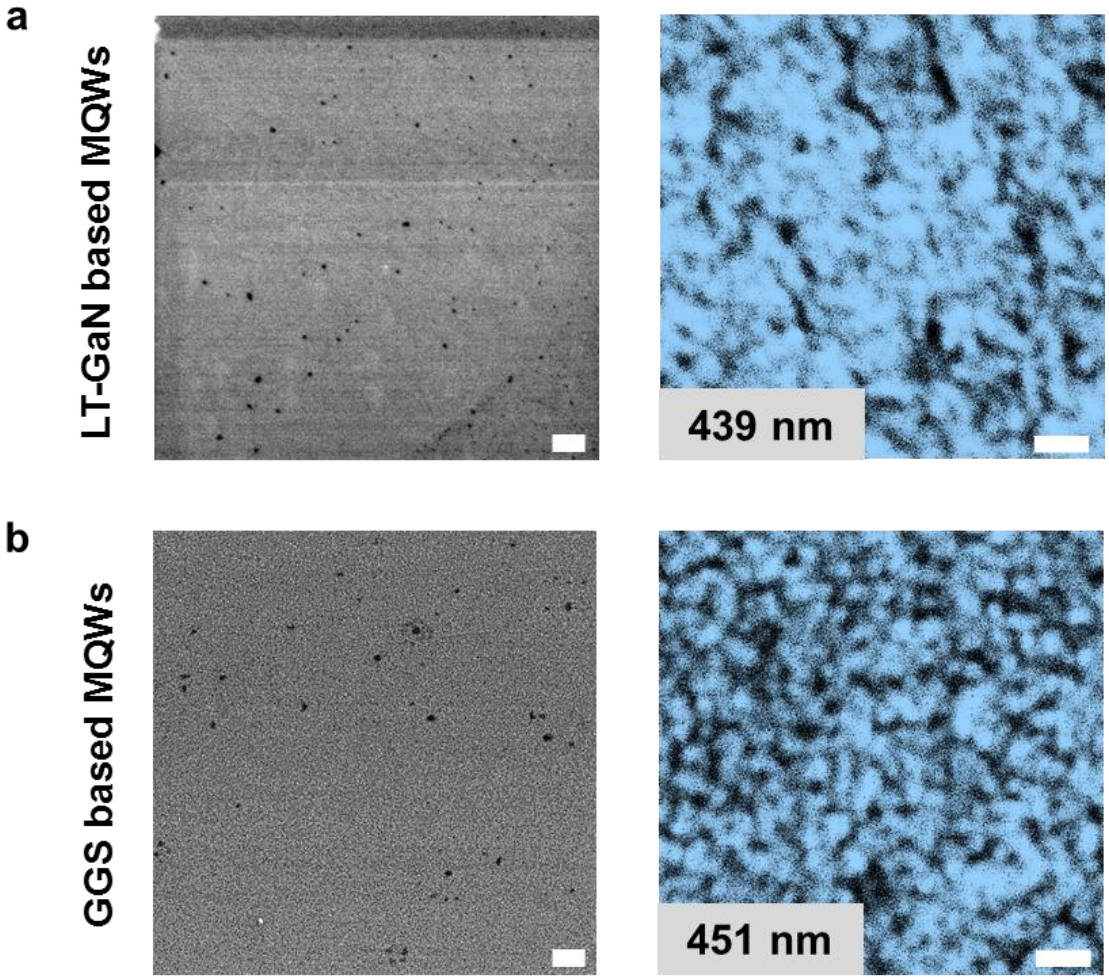

Figure 4-3. SEM images (left) and corresponding LT (77K) monochromatic CL mapping images (right) of 3 pairs of InGaN/GaN MQWs grown on LT-GaN buffer layer in (a) and graphene coating layer in (b). (scale bar 2 μm)

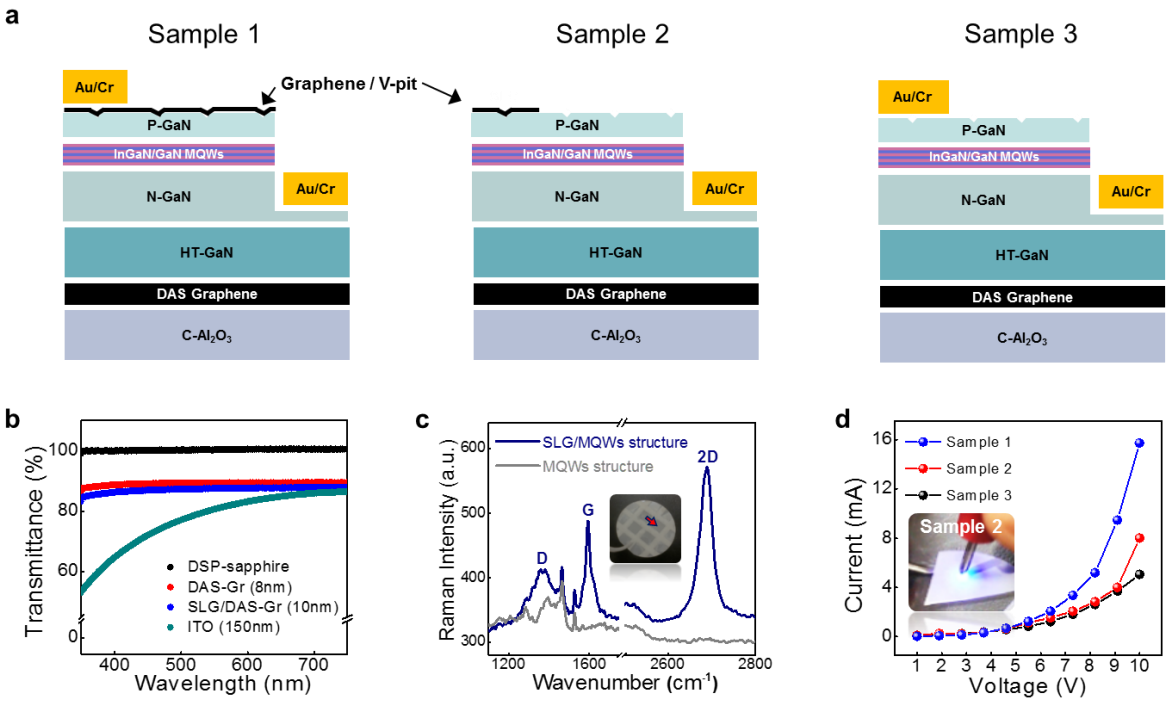

Figure 4-4. (a) Schematic illustrations of three types of samples with metal/graphene (sample 1), graphene (sample 2), and metal electrode (sample 3). (b) Transmittance data of DAS-graphene, DAS-graphene with a single layer graphene (SLG), and ITO (150nm) under the double-sided polished (DSP) sapphire base line. (c) Representative Raman spectra of SLG electrode coated- and bare- DAS-graphene based MQWs structure. Inset shows picture of SLG electrode coated, 1cm×1cm patterned MQWs structures on 2-inch C-sapphire substrate. (d) I-V curves of sample 1~3 in (a). Inset shows luminescence of sample 2 using power source meter (5 V).

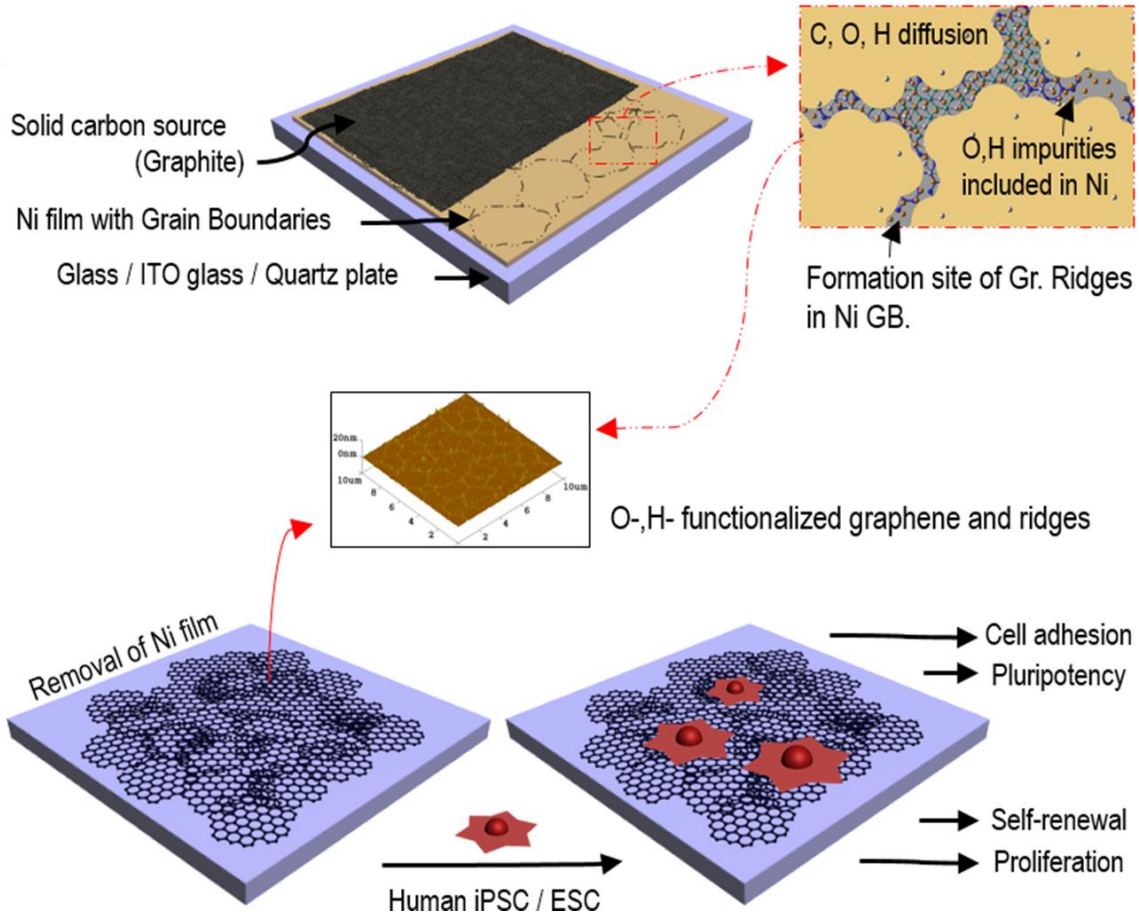

Figure 4-5. Schematic illustrations of direct synthesis of large-area graphene on desired substrates using DAS process for graphene based scaffolds.

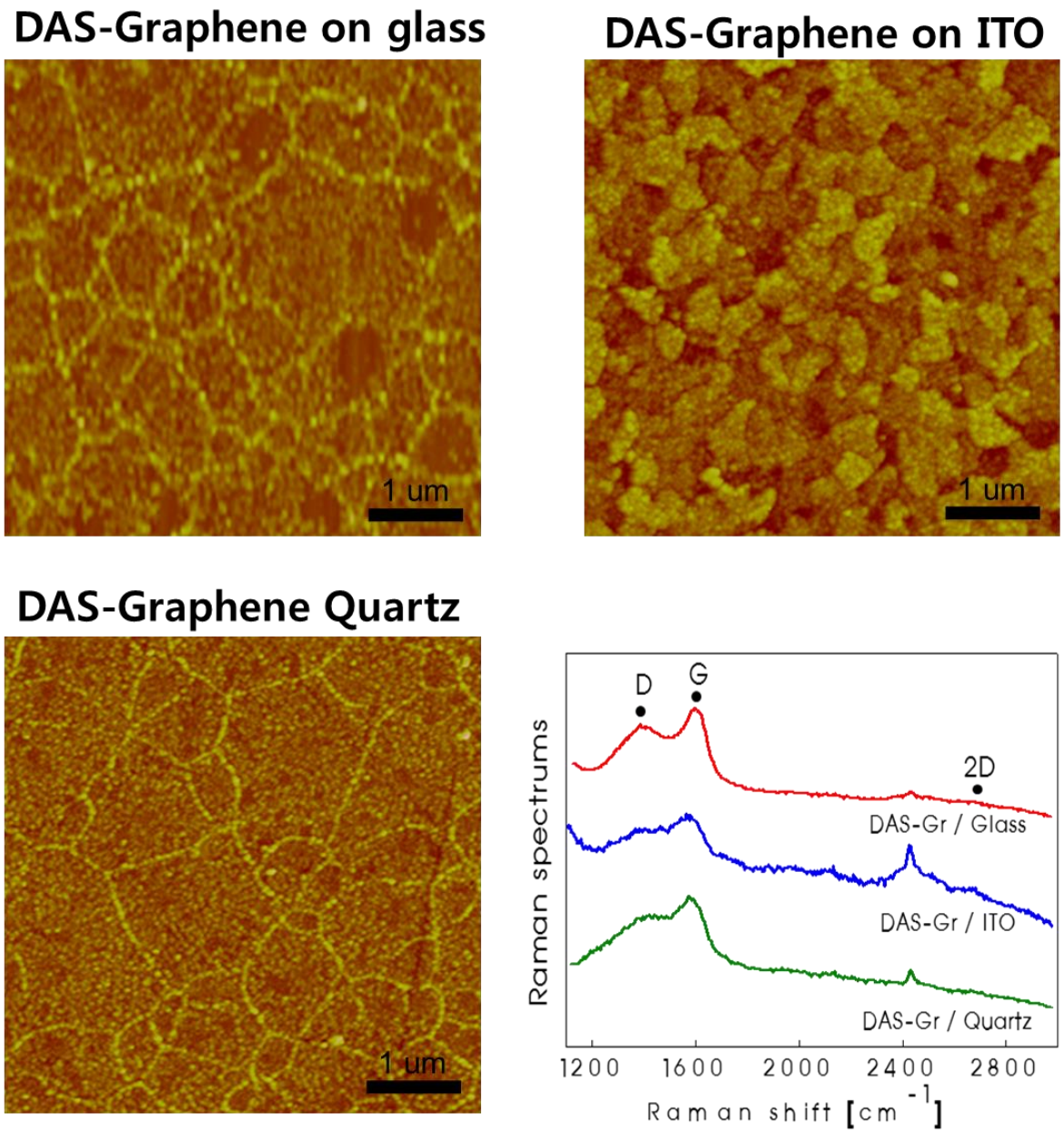

Figure 4-6. Atomic force microscopy (AFM) images, showing the naturally-formed multilayer graphene directly synthesized onto Glass, ITO/glass, Quartz plate and transferred onto SiO_2 after conventional CVD processes. The Raman spectrums of graphene coated on each substrates using DAS process at 360 ℃ for 90 min.

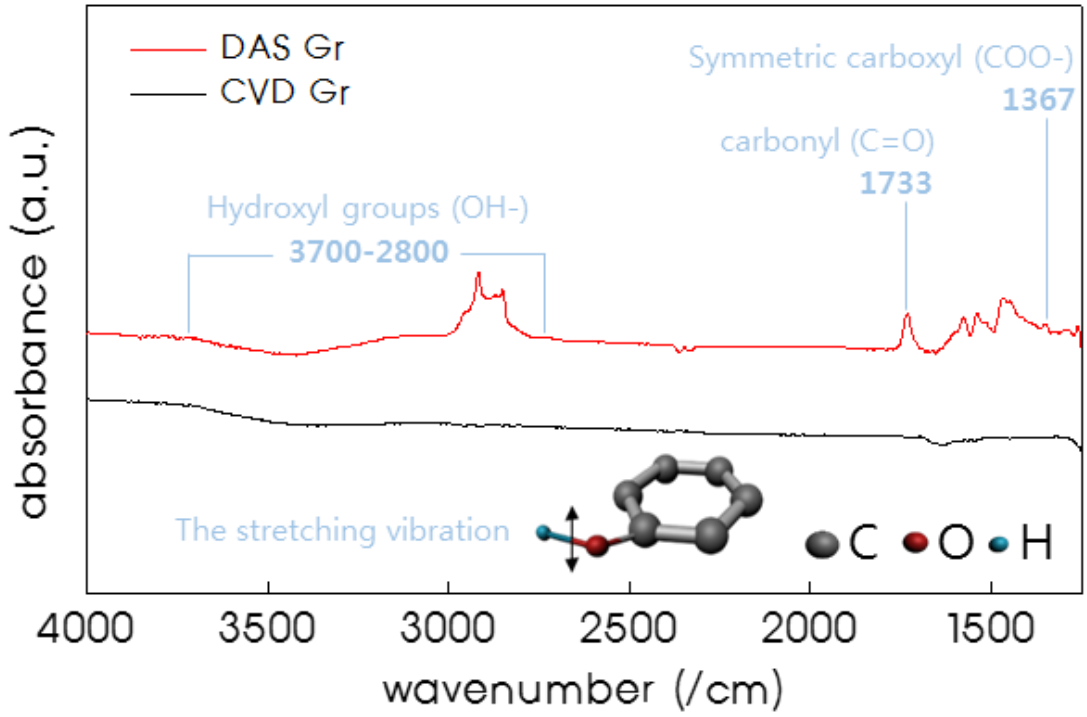

Figure 4-7. ATR-FTIR (Fourier transform infrared) spectra of graphene on SiO_2/Si samples isolated from (red line) DAS process and (black line) conventional CVD process. Major bands and proposed assignments: 1367 cm^{-1} (COO^- stretch), 1733 cm^{-1} (C=O stretch), from 2800 to 3700 cm^{-1} (O-H stretching vibrations).

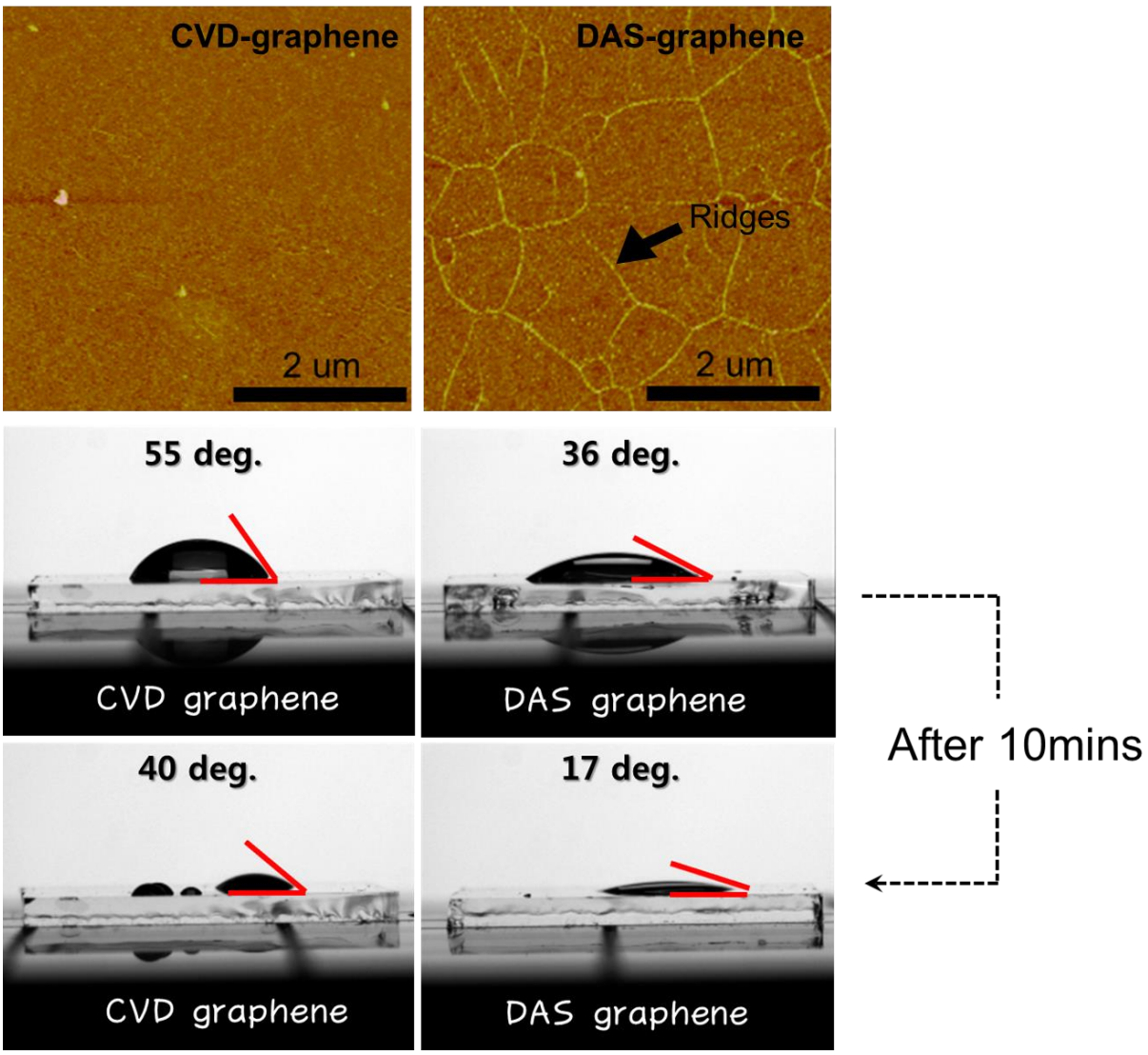

Figure 4-8. Surface wettability of graphene coated glass substrates using a contact angle for the culture fluids.

Summary

In summary, using the CVD method, I demonstrated that the orientation-sensitive graphene was grown by Pt thin films with preferred orientations of (200, 220) and controlled giant grains. The graphene showed wrinkle-free characteristic. In addition, the large-scale and patterned graphene films can be successfully transferred onto arbitrary substrates via the hydroxide ionic transfer assisted thermal energy. The successful graphene transfer from surface modified Pt films demonstrated its recycle ability. I have also demonstrated the effectiveness of transferring patterned graphene without incurring damage. Using the noble properties of Pt and the thermal-assisted transfer method, I achieved porous graphene membrane using controlled Pt(111) film to get near the commercialization, which will markedly decrease the defects such as impurities in the resulting hydrophobic surface of graphene membrane. Using the graphene, I applied the transparent metal-free electrodes for graphene double-sided III-N LED epi-structures and the graphene-based scaffolds for stem-cell differentiation.

References

1. Oshima, Chuhei, and Ayato Nagashima. "Ultra-thin epitaxial films of graphite and hexagonal boron nitride on solid surfaces." *Journal of Physics: Condensed Matter* 9.1 (1997): 1.
2. Boehm, Hans Peter, R. Setton, and E. Stumpp. "Nomenclature and terminology of graphite intercalation compounds (IUPAC Recommendations 1994)." *Pure and Applied Chemistry* 66.9 (1994): 1893-1901.
3. Lee, Changgu, et al. "Measurement of the elastic properties and intrinsic strength of monolayer graphene." *science* 321.5887 (2008): 385-388.
4. landin, Alexander A., et al. "Superior thermal conductivity of single-layer graphene." *Nano letters* 8.3 (2008): 902-907.
5. Chen, Jian-Hao, et al. "Intrinsic and extrinsic performance limits of graphene devices on SiO2." *Nature nanotechnology* 3.4 (2008): 206-209.
6. Avouris, Phaedon, Zhihong Chen, and Vasili Perebeinos. "Carbon-based electronics." *Nature nanotechnology* 2.10 (2007): 605-615.
7. Novoselov, Kostya S., et al. "Electric field effect in atomically thin carbon films." *science* 306.5696 (2004): 666-669.
8. Geim, Andre K., and Konstantin S. Novoselov. "The rise of graphene." *Nature materials* 6.3 (2007): 183-191.
9. Seol, Jae Hun, et al. "Two-dimensional phonon transport in supported graphene." *Science* 328.5975 (2010): 213-216.
10. Zhao, Shihua, Yi Lv, and Xinju Yang. "Layer-dependent nanoscale electrical properties of graphene studied by conductive scanning probe microscopy." *Nanoscale research letters* 6.1 (2011): 1-6.
11. Wang, Yingying, et al. "Stacking-dependent optical conductivity of bilayer graphene." *ACS nano* 4.7 (2010): 4074-4080.
12. Zhu, Shou-En, and G. C. A. M. Janssen. "Optical transmittance of multilayer graphene." *EPL (Europhysics Letters)* 108.1 (2014): 17007.
13. Tung, Vincent C., et al. "High-throughput solution processing of large-scale graphene." *Nature nanotechnology* 4.1 (2009): 25-29.
14. Park, Sungjin, and Rodney S. Ruoff. "Chemical methods for the production of graphenes." *Nature nanotechnology* 4.4 (2009): 217-224.
15. Varchon, François, et al. "Electronic structure of epitaxial graphene layers on SiC: effect of the substrate." *Physical review letters* 99.12 (2007): 126805.

16. Kim, Keun Soo, et al. "Large-scale pattern growth of graphene films for stretchable transparent electrodes." *Nature* 457.7230 (2009): 706-710.
17. Kwak, Jinsung, et al. "In situ observations of gas phase dynamics during graphene growth using solid-state carbon sources." *Physical Chemistry Chemical Physics* 15.25 (2013): 10446-10452.
18. Novoselov, Konstantin S., et al. "A roadmap for graphene." *Nature* 490.7419 (2012): 192-200.
19. Zhang, Yanhong, et al. "Enhanced reactivity of graphene wrinkles and their function as nanosized gas inlets for reactions under graphene." *Phys. Chem. Chem. Phys.* 15.43 (2013): 19042-19048.
20. Zhu, Wenjuan, et al. "Structure and electronic transport in graphene wrinkles." *Nano letters* 12.7 (2012): 3431-3436.
21. Van Gastel, Raoul, et al. "In situ observation of stress relaxation in epitaxial graphene." *New Journal of Physics* 11.11 (2009): 113056.
22. Chae, Seung Jin, et al. "Synthesis of large-area graphene layers on poly-nickel substrate by chemical vapor deposition: wrinkle formation." *Adv. Mater* 21.22 (2009): 2328-2333.
23. Calado, V. E., et al. "Formation and control of wrinkles in graphene by the wedging transfer method." *Applied Physics Letters* 101.10 (2012): 103116.
24. Li, Xuesong, et al. "Large-area synthesis of high-quality and uniform graphene films on copper foils." *Science* 324.5932 (2009): 1312-1314.
25. Lahiri, Jayeeta, et al. "Graphene growth and stability at nickel surfaces." *New Journal of Physics* 13.2 (2011): 025001.
26. Sutter, Peter, Jerzy T. Sadowski, and Eli Sutter. "Graphene on Pt (111): Growth and substrate interaction." *Physical Review B* 80.24 (2009): 245411.
27. Sutter, Peter W., Jan-Ingo Flege, and Eli A. Sutter. "Epitaxial graphene on ruthenium." *Nature materials* 7.5 (2008): 406-411.
28. Kwon, Soon-Yong, et al. "Growth of semiconducting graphene on palladium." *Nano letters* 9.12 (2009): 3985-3990.
29. Liu, Wei, et al. "Synthesis of high-quality monolayer and bilayer graphene on copper using chemical vapor deposition." Carbon 49.13 (2011): 4122-4130.
30. Yoon, Duhee, Young-Woo Son, and Hyeonsik Cheong. "Negative thermal expansion coefficient of graphene measured by Raman spectroscopy." *Nano letters* 11.8 (2011): 3227-3231.
31. Gao, Libo, et al. "Repeated growth and bubbling transfer of graphene with millimetre-size single-crystal grains using platinum." *Nature communications* 3 (2012): 699.
32. Akazawa, Housei. "Correlation between Adhesive Strength and the Oxidized and Reduced States of Pt Films Electron Cyclotron Resonance Plasma Sputtered on SiO2." *Japanese Journal of Applied Physics* 50.6R (2011): 065805.
33. Hecq, M., and A. Hecq. "A glow discharge mass spectrometry study of reactive sputtering." *Thin Solid Films* 76.1 (1981): 35-44.

34. Hecq, M., and A. Hecq. "Oxygen induced preferred orientation of dc sputtered platinum." *Journal of Vacuum Science & Technology* 18.2 (1981): 219-222.
35. Thompson, Carl V. "On the grain size and coalescence stress resulting from nucleation and growth processes during formation of polycrystalline thin films." *Journal of materials research* 14.07 (1999): 3164-3168.
36. Mullins, W. W. "The effect of thermal grooving on grain boundary motion." *Acta metallurgica* 6.6 (1958): 414-427.
37. Thompson, C. V., H. J. Frost, and F. Spaepen. "The relative rates of secondary and normal grain growth." *Acta Metallurgica* 35.4 (1987): 887-890.
38. Frost, H. J., C. V. Thompson, and D. T. Walton. "Simulation of thin film grain structures—II. Abnormal grain growth." *Acta metallurgica et materialia* 40.4 (1992): 779-793.
39. Miao, Congqin, et al. *Chemical vapor deposition of graphene.* INTECH Open Access Publisher, 2011.
40. Malard, L. M., et al. "Raman spectroscopy in graphene." *Physics Reports* 473.5 (2009): 51-87.
41. Mattevi, Cecilia, Hokwon Kim, and Manish Chhowalla. "A review of chemical vapour deposition of graphene on copper." *Journal of Materials Chemistry* 21.10 (2011): 3324-3334.
42. Bae, Sukang, et al. "Towards industrial applications of graphene electrodes." *Physica Scripta* 2012.T146 (2012): 014024.
43. Kim, Keun Soo, et al. "Large-scale pattern growth of graphene films for stretchable transparent electrodes." *Nature* 457.7230 (2009): 706-710.
44. Lock, Evgeniya H., et al. "High-quality uniform dry transfer of graphene to polymers." *Nano letters* 12.1 (2011): 102-107.
45. Caldwell, Joshua D., et al. "Technique for the dry transfer of epitaxial graphene onto arbitrary substrates." *ACS nano* 4.2 (2010): 1108-1114.
46. Anantatmula, R. P., S. G. Pitman, and A. L. Lund. *Selection of replacement material for the failed surface level gauge wire in Hanford waste tanks.* No. WHC-SA--2990-FP; CONF-960389--6. Westinghouse Hanford Co., Richland, WA (United States), 1995.
47. Azaroual, Mohamed, et al. "Solubility of platinum in aqueous solutions at 25 C and pHs 4 to 10 under oxidizing conditions." *Geochimica et Cosmochimica Acta* 65.24 (2001): 4453-4466.
48. Parkinson, C. R., M. Walker, and C. F. McConville. "Reaction of atomic oxygen with a Pt (111) surface: chemical and structural determination using XPS, CAICISS and LEED." *Surface Science* 545.1 (2003): 19-33.
49. Reina, Alfonso, et al. "Transferring and identification of single-and few-layer graphene on arbitrary substrates." *The Journal of Physical Chemistry C* 112.46 (2008): 17741-17744.
50. Surwade, Sumedh P., et al. "Water desalination using nanoporous single-layer graphene." *Nature nanotechnology* 10.5 (2015): 459-464.

51. Cohen-Tanugi, David, and Jeffrey C. Grossman. "Water desalination across nanoporous graphene." *Nano letters* 12.7 (2012): 3602-3608.
52. Lawson, Kevin W., and Douglas R. Lloyd. "Membrane distillation." *Journal of membrane Science* 124.1 (1997): 1-25.
53. Konatham, Deepthi, et al. "Simulation insights for graphene-based water desalination membranes." *Langmuir* 29.38 (2013): 11884-11897.
54. Humplik, T., et al. "Nanostructured materials for water desalination." *Nanotechnology* 22.29 (2011): 292001.
55. Talbot, D. E. J. "Effects of hydrogen in aluminium, magnesium, copper, and their alloys." *International Metallurgical Reviews* 20.1 (1975): 166-184.
56. Wang, Hong, et al. "Lateral homoepitaxial growth of graphene." *CrystEngComm* 16.13 (2014): 2593-2597.
57. Xu, Sheng, and Zhong Lin Wang. "One-dimensional ZnO nanostructures: solution growth and functional properties." *Nano Research* 4.11 (2011): 1013-1098.
58. Nakamura, Shuji, Takashi Mukai, and Masayuki Senoh. "High-brightness InGaN/AlGaN double-heterostructure blue-green-light-emitting diodes." *Journal of Applied Physics* 76.12 (1994): 8189-8191.
59. Ponce, F. A., and D. P. Bour. "Nitride-based semiconductors for blue and green light-emitting devices." *Nature* (1997).
60. Mohammad, S. N., and Hadis Morkoç. "Progress and prospects of group-III nitride semiconductors." *Progress in Quantum Electronics* 20.5 (1996): 361-525.
61. Khan, M. Asif, et al. "Insulating gate III-N heterostructure field-effect transistors for high-power microwave and switching applications." Microwave Theory and Techniques, *IEEE Transactions on* 51.2 (2003): 624-633.
62. Khan, M. Asif, et al. "III–nitride UV devices." *Japanese Journal of Applied Physics* 44.10R (2005): 7191.
63. Vispute, R. D., et al. "Heteroepitaxy of ZnO on GaN and its implications for fabrication of hybrid optoelectronic devices." *Applied Physics Letters* 73.3 (1998): 348-350.
64. Yao, Takafumi, and Soon-Ku Hong, eds. *Oxide and nitride semiconductors: processing, properties, and applications.* Vol. 12. Springer Science & Business Media, 2009.
65. Bernardini, Fabio, Vincenzo Fiorentini, and David Vanderbilt. "Spontaneous polarization and piezoelectric constants of III-V nitrides." *Physical Review B* 56.16 (1997): R10024.
66. Nakamura, Shuji, Stephen Pearton, and Gerhard Fasol. *The blue laser diode: the complete story.* Springer Science & Business Media, 2013.
67. Bernardini, Fabio, Vincenzo Fiorentini, and David Vanderbilt. "Polarization-based calculation of the dielectric tensor of polar crystals." *Physical review letters* 79.20 (1997): 3958.

68. Li, Y-L., Y-R. Huang, and Y-H. Lai. "Efficiency droop behaviors of InGaN/ GaN multiple-quantum-well light-emitting diodes with varying quantum well thickness." *Applied Physics Letters* 91.18 (2007): 181113.
69. Martin, G., et al. "Valence-band discontinuities of wurtzite GaN, AlN, and InN heterojunctions measured by x-ray photoemission spectroscopy." *Applied Physics Letters* 68.18 (1996): 2541-2543.
70. Ambacher, O., et al. "Two dimensional electron gases induced by spontaneous and piezoelectric polarization in undoped and doped AlGaN/GaN heterostructures." *Journal of applied physics* 87.1 (2000): 334-344.
71. Kim, Jonghak, et al. "Less strained and more efficient GaN light-emitting diodes with embedded silica hollow nanospheres." *Scientific reports* 3 (2013).
72. Park, Seoung-Hwan, et al. "Polarization characteristics of semipolar (11$\bar{2}$2) InGaN/GaN quantum well structures grown on relaxed InGaN buffer layers and comparison with experiment." *Optics express* 22.12 (2014): 14850-14858.
73. Kim, Jaehwan, et al. "Strain relaxation of thick (11–22) semipolar InGaN layer for long wavelength nitride-based device." *Journal of Applied Physics* 116.16 (2014): 163109.
74. Koslow, Ingrid L., et al. "Onset of plastic relaxation in semipolar (11-22) $In_xGa_{1-x}N$/GaN heterostructures." *Journal of Crystal Growth* 388 (2014): 48-53.
75. Su, Vin-Cent, et al. "Suppressed quantum-confined Stark effect in InGaN-based LEDs with nano-sized patterned sapphire substrates." *Optics express* 21.24 (2013): 30065-30073.
76. You, Yao-Hong, et al. "Influence of patterned sapphire substrates with different symmetry on the light output power of InGaN-based LEDs." *Nanoscale research letters* 9.1 (2014): 1-8.
77. Chung, Kunook, Chul-Ho Lee, and Gyu-Chul Yi. "Transferable GaN layers grown on ZnO-coated graphene layers for optoelectronic devices." *Science* 330.6004 (2010): 655-657.
78. Seo, Tae Hoon, et al. "Direct growth of GaN layer on carbon nanotube-graphene hybrid structure and its application for light emitting diodes." *Scientific reports* 5 (2015).
79. aek, Hyeonjun, et al. "Epitaxial GaN microdisk lasers grown on graphene microdots." *Nano letters* 13.6 (2013): 2782-2785.
80. Han, Nam, et al. "Improved heat dissipation in gallium nitride light-emitting diodes with embedded graphene oxide pattern." *Nature communications* 4 (2013): 1452.
81. JináChae, Seung, et al. "Direct growth of etch pit-free GaN crystals on few-layer graphene." *RSC Advances* 5.2 (2015): 1343-1349.
82. Choi, Jae-Kyung, et al. "One-step graphene coating of heteroepitaxial GaN films." *Nanotechnology* 23.43 (2012): 435603.
83. Ryu, Beo Deul, et al. "Fabrication and Characteristics of GaN-Based Light-Emitting Diodes with a Reduced Graphene Oxide Current-Spreading Layer." *ACS applied materials & interfaces* 6.24 (2014): 22451-22456.

84. Chung, Kunook, et al. "High-quality GaN films grown on chemical vapor-deposited graphene films." *NPG Asia Materials* 4.9 (2012): e24.
85. Yoon, Duhee, Young-Woo Son, and Hyeonsik Cheong. "Negative thermal expansion coefficient of graphene measured by Raman spectroscopy." *Nano letters* 11.8 (2011): 3227-3231.
86. Kwon, Soon-Yong, et al. "Growth of semiconducting graphene on palladium." *Nano letters* 9.12 (2009): 3985-3990.
87. Avouris, Phaedon. "Graphene: electronic and photonic properties and devices." *Nano letters* 10.11 (2010): 4285-4294.
88. Choi, Jae-Kyung, et al. "Growth of Wrinkle-Free Graphene on Texture-Controlled Platinum Films and Thermal-Assisted Transfer of Large-Scale Patterned Graphene." *ACS nano* 9.1 (2014): 679-686.
89. Kwak, Jinsung, et al. "Near room-temperature synthesis of transfer-free graphene films." *Nature communications* 3 (2012): 645.
90. Dalby, Matthew J., et al. "The control of human mesenchymal cell differentiation using nanoscale symmetry and disorder." *Nature materials* 6.12 (2007): 997-1003.
91. Engler, Adam J., et al. "Matrix elasticity directs stem cell lineage specification." *Cell* 126.4 (2006): 677-689.
92. Harding, Frances, et al. "Surface bound amine functional group density influences embryonic stem cell maintenance." *Advanced healthcare materials* 2.4 (2013): 585-590.
93. Benoit, Danielle SW, et al. "Small functional groups for controlled differentiation of hydrogel-encapsulated human mesenchymal stem cells." *Nature materials* 7.10 (2008): 816-823.
94. Wu, Amanda S., and Tsu-Wei Chou. "Carbon nanotube fibers for advanced composites." *Materials Today* 15.7 (2012): 302-310.
95. Shuai, Cijun, et al. "Fabrication of porous polyvinyl alcohol scaffold for bone tissue engineering via selective laser sintering." *Biofabrication* 5.1 (2013): 015014.
96. Li, Ning, et al. "Three-dimensional graphene foam as a biocompatible and conductive scaffold for neural stem cells." *Scientific reports* 3 (2013).
97. Nayak, Tapas R., et al. "Graphene for controlled and accelerated osteogenic differentiation of human mesenchymal stem cells." *ACS nano* 5.6 (2011): 4670-4678.
98. Nwe, Nitar, Tetsuya Furuike, and Hiroshi Tamura. "The mechanical and biological properties of chitosan scaffolds for tissue regeneration templates are significantly enhanced by chitosan from Gongronella butleri." *Materials* 2.2 (2009): 374-398.
99. Martins, Ana M., et al. "Electrically conductive chitosan/carbon scaffolds for cardiac tissue engineering." *Biomacromolecules* 15.2 (2014): 635-643.
100. Thompson, R., and M. Yaszemski. "Polymer Scaffold Processing. Principles of Tissue Engineering." (1997): 263-272.

101. Chen, Y-T., and H. L. Kao. "Humidity sensors made on polyvinyl-alcohol film coated SAW devices." *Electronics Letters* 42.16 (2006): 948-950.

102. Rao, C. emsp14N emsp14R, et al. "Graphene: The New Two-Dimensional Nanomaterial." *Angewandte Chemie International Edition* 48.42 (2009): 7752-7777.

103. Kang, Dong-Hun, et al. "Growth and evaluation of GaN grown on patterned sapphire substrates." *Journal of Korean Physical Society* 52 (2008): 1895.

104. Suihkonen, S., et al. "Patterning of sapphire/GaN substrates." *physica status solidi (c)* 8.5 (2011): 1509-1512.

105. Chen, Lung-Chien, and Wen-Fang Tsai. "Properties of GaN-based light-emitting diodes on patterned sapphire substrate coated with silver nanoparticles prepared by mask-free chemical etching." *Nanoscale research letters* 8.1 (2013): 1-6.

106. Jo, Gunho, et al. "Large-scale patterned multi-layer graphene films as transparent conducting electrodes for GaN light-emitting diodes." *Nanotechnology* 21.17 (2010): 175201.

107. Nam, Ok-Hyun, et al. "Lateral epitaxy of low defect density GaN layers via organometallic vapor phase epitaxy." *Applied physics letters* 71.18 (1997): 2638-2640.

108. Yan, P. F., K. Du, and M. L. Sui. "Pyramidal dislocation induced strain relaxation in hexagonal structured InGaN/AlGaN/GaN multilayer." *Journal of Applied Physics* 112.8 (2012): 083502.

109. Shiojiri, M., et al. "Structure and formation mechanism of V defects in multiple InGaN/GaN quantum well layers." *Journal of applied physics* 99.7 (2006): 073505.

110. Lee, Jung Min, et al. "Metal/graphene sheets as p-type transparent conducting electrodes in GaN light emitting diodes." *Applied Physics Letters* 99.4 (2011): 041115.

111. Na, Seok-In, et al. "Efficient and flexible ITO-free organic solar cells using highly conductive polymer anodes." *Adv. Mater* 20.21 (2008): 4061-4067.

112. Bae, Goh-Myeong. "III-N LEDs with graphene double-sided InGaN/GaN multiple quantum well structures." (2015).

113. Casiraghi, C. "Doping dependence of the Raman peaks intensity of graphene close to the Dirac point." *Physical Review B* 80.23 (2009): 233407.

114. Ferrari, A. C., et al. "Raman spectrum of graphene and graphene layers." *Physical review letters* 97.18 (2006): 187401.

115. Ferrari, Andrea C. "Raman spectroscopy of graphene and graphite: disorder, electron–phonon coupling, doping and nonadiabatic effects." *Solid state communications* 143.1 (2007): 47-57.

116. Novoselov, Konstantin S., et al. "A roadmap for graphene." *Nature* 490.7419 (2012): 192-200.

117. Shen, He, et al. "Biomedical applications of graphene." *Theranostics* 2.3 (2012): 283.

118. Liu, Zhuang, et al. "PEGylated nanographene oxide for delivery of water-insoluble cancer drugs." *Journal of the American Chemical Society* 130.33 (2008): 10876-10877.

119. Misra, Ambikanandan, et al. "Drug delivery to the central nervous system: a review." *J Pharm Pharm Sci* 6.2 (2003): 252-73.

120. Pan, Dengyu, et al. "Hydrothermal route for cutting graphene sheets into blue-luminescent graphene quantum dots." *Advanced Materials* 22.6 (2010): 734-738.

121. Georgakilas, Vasilios, et al. "Functionalization of graphene: covalent and non-covalent approaches, derivatives and applications." *Chemical reviews* 112.11 (2012): 6156-6214.

122. Chen, Zongping, et al. "Three-dimensional flexible and conductive interconnected graphene networks grown by chemical vapour deposition." *Nature materials* 10.6 (2011): 424-428.

123. Hutmacher, Dietmar W. "Scaffold design and fabrication technologies for engineering tissues—state of the art and future perspectives." *Journal of Biomaterials Science, Polymer Edition* 12.1 (2001): 107-124.

124. Shahini, Aref, et al. "3D conductive nanocomposite scaffold for bone tissue engineering." *International journal of nanomedicine* 9 (2014): 167.

125. Robinson, Jeremy T., et al. "Wafer-scale reduced graphene oxide films for nanomechanical devices." *Nano letters* 8.10 (2008): 3441-3445.

126. Acik, M., et al. "Unusual infrared-absorption mechanism in thermally reduced graphene oxide." *Nature materials* 9.10 (2010): 840-845.

127. Szabó, Tamás, et al. "Evolution of surface functional groups in a series of progressively oxidized graphite oxides." *Chemistry of materials* 18.11 (2006): 2740-2749.

128. Liang, Yanyu, et al. "Dispersion of graphene sheets in organic solvent supported by ionic interactions." *Advanced materials* 21.17 (2009): 1679-1683.

129. Israr, Muhammad Qadir, et al. "Structural characterization and biocompatible applications of graphene nanosheets for miniaturization of potentiometric cholesterol biosensor." *Journal of Biosensors & Bioelectronics* 2.3 (2011).

130. Lee, Wong Cheng, et al. "Origin of enhanced stem cell growth and differentiation on graphene and graphene oxide." *ACS nano* 5.9 (2011): 7334-7341.

131. Dhiman, Prashant, et al. "Harvesting energy from water flow over graphene." *Nano letters* 11.8 (2011): 3123-3127.

132. Rafiee, Javad, et al. "Wetting transparency of graphene." *Nature Materials* 11.3 (2012): 217-222.

133. Mugele, Frieder. "Wetting: Unobtrusive graphene coatings." *Nature materials* 11.3 (2012): 182-183.

134. Seabra, Amedea B., et al. "Nanotoxicity of graphene and graphene oxide." *Chemical research in toxicology* 27.2 (2014): 159-168.

135. Sanchez, Vanesa C., et al. "Biological interactions of graphene-family nanomaterials: an interdisciplinary review." *Chemical research in toxicology* 25.1 (2011): 15-34.

136. Metcalfe, Anthony D., and Mark WJ Ferguson. "Tissue engineering of replacement skin: the crossroads of biomaterials, wound healing, embryonic development, stem cells and regeneration." *Journal of the Royal Society Interface* 4.14 (2007): 413-437.

137. Ikada, Yoshito. "Challenges in tissue engineering." *Journal of The Royal Society Interface* 3.10 (2006): 589-601.